Constraining Source Models, Underlying Mechanisms, and Hazards Associated with Slow Slip Events: Insight from Space-Borne Geodesy and Seismology

by

Mostafa Khoshmanesh

A Dissertation Presented in Partial Fulfilment
of the Requirement for the Degree
Doctor of Philosophy

Approved October 2018 by the
Graduate Supervisory Committee:

Manoochehr Shirzaei, Chair
Ramon Arrowsmith
Edward Garnero
James Tyburczy
Kelin Whipple

ARIZONA STATE UNIVERSITY

December 2018

ABSTRACT

The movement between tectonic plates is accommodated through brittle (elastic) displacement on the plate boundary faults and ductile permanent deformation on the fault borderland. The elastic displacement along the fault can occur in the form of either large seismic events or aseismic slip, known as fault creep. Fault creep mainly occurs at the deep ductile portion of the crust, where the temperature is high. Nonetheless, aseismic creep can also occur on the shallow brittle portion of the fault segments that are characterized by frictionally weak material, elevated pore fluid pressure, or geometrical complexity. Creeping segments are assumed to safely release the accumulated strain(Kodaira et al., 2004; Rice, 1992)(Kodaira et al., 2004; Rice, 1992)(Kodaira et al., 2004; Rice, 1992)(Kodaira et al., 2004; Rice, 1992)(Kodaira et al., 2004; Rice, 1992) on the fault and also impede propagation of the seismic rupture. The rate of aseismic slip on creeping faults, however, might not be steady in time and instead consist of successive periods of acceleration and deceleration, known as slow slip events (SSEs). SSEs, which aseismically release the strain energy over a period of days to months, rather than the seconds to minutes characteristic of a typical earthquake, have been interpreted as earthquake precursors and as possible triggering factor for major earthquakes. Therefore, understanding the partitioning of seismic and aseismic fault slip and evolution of creep is fundamental to constraining the fault earthquake potential and improving operational seismic hazard models. Thanks to advances in tectonic geodesy, it is now possible to detect the fault movement in high spatiotemporal resolution and develop kinematic models of the creep evolution on the fault to determine the budget of seismic and aseismic slip.

In this dissertation, I measure the decades-long time evolution of fault-related crustal deformation along the San Andrea Fault in California and the northeast Japan subduction zone using space-borne geodetic techniques, such as Global Positioning System (GPS) and

Interferometric Synthetic Aperture Radar (InSAR). The surface observation of deformation combined with seismic data set allow constraining the time series of creep distribution on the fault surface at seismogenic depth. The obtained time-dependent kinematic models reveal that creep in both study areas evolves through a series of SSEs, each lasting for several months. Using physics-based models informed by laboratory experiments, I show that the transient elevation of pore fluid pressure is the driving mechanism of SSEs. I further investigate the link between SSEs and evolution of seismicity on neighboring locked segments, which has implications for seismic hazard models and also provides insights into the pattern of microstructure on the fault surface. I conclude that while creeping segments act as seismic rupture barriers, SSEs on these zones might promote seismicity on adjacent seismogenic segments, thus change the short-term earthquake forecast.

To Sepideh, Hassan & Mansoureh

ACKNOWLEDGMENTS

I am greatly thankful to my PhD advisor, Dr. Manoochehr Shirzaei for his unconditional support and guidance throughout these years. His ability to create and maintain a collaborative relationship with his students and giving them the credit (sometimes even much more than what I personally deserved) is quite exemplary. I also wish to express my gratitude to my graduate advisory committee, Dr. Ramon Arrowsmith, Dr. Edward Garnero, Dr. Kelin Whipple, and Dr. James Tyburczy for their constructive comments and suggestions on different stages of my research.

I wish to thank my fellow Remote Sensing & Tectonic Geodesy Lab (RaTLab) members, Dr. Suzanna Werth, Dr. Jennifer Weston, Dr. Chandrakant Ojha, Dr. Megan Miller, Dr. Guang Zhai, Grace Carlson, Sonam Sherpa, and Emma Blackwell for support, wisdom, and raising the bar day in day out.

A special thanks to my fiancée, Sepideh, for her endless love and support. Your belief in me boosted my energy and confidence in every step of the way. My time here, and my life, are better for having met you. A great thanks to my dad for being who he is, one of the strongest souls I have ever known. Also thank you to my mom and sisters for their love and support.

This PhD research was partly supported by a NASA Earth and Space Science Fellowship. So, I would like to extend my gratefulness to National Aeronautics and Space Administration (NASA) for providing a great opportunity for all the graduate student, regardless of citizenship status and nationality.

TABLE OF CONTENT

CHAPTER Page

CHAPTER Page

LIST OF TABLES

Table Page

LIST OF FIGURES

Figure Page

Figure Page

CHAPTER 1.

INTRODUCTION

1.1. Central San Andreas Fault

As a boundary between the North America and Pacific plate, the San Andreas Fault (SAF) is a right-lateral, 1,100 km long transform fault, running all the way from north of the Gulf of California to the Mendocino triple junction. The fault segment between San Juan Bautista and Parkfield forms the Central 140 km section of the San Andreas Fault (CSAF) (Figure 1.1). Slip on this section of the SAF is predominantly aseismic, with a rate of up to 32 mm/year (Ryder & Bürgmann, 2008). The shallow creep tapers off toward zero, southeast of the Parkfield transition zone, and is accommodated by sub-parallel faults toward the northwest, reaching to fully locked segments that ruptured during the 1906 moment magnitude (M_w) 7.9 San Francisco earthquake (Song et al., 2008). According to seismicity records, no earthquake larger than M_w 4 has been observed in the middle 60 km segment of the CSAF over the last seven decades, but moderate earthquakes occurred in the bounding transition regions (Rolandone et al., 2008). Adjoining segments of the SAF are locked and slip mostly in large seismic events, making this almost continuous aseismic slip a unique characteristic of the CSAF.

The estimated geodetic long-term slip rates along the CSAF at near (<10 m) and intermediate distances (10 m to 1 km) from the fault trace are 25 ± 1 and 28 ± 2 mm/year, respectively (Titus et al., 2006). However, using the Global Positioning System (GPS) observation, Titus et al. (2011) estimated 26.5 ± 0.2 mm/year rate for the fault-parallel right-lateral motion between Sierra Nevada-Great Valley block and Pacific Plate, which is consistent with that estimated by Toké et al. (2011). This surficial creep rate gradient in perpendicular

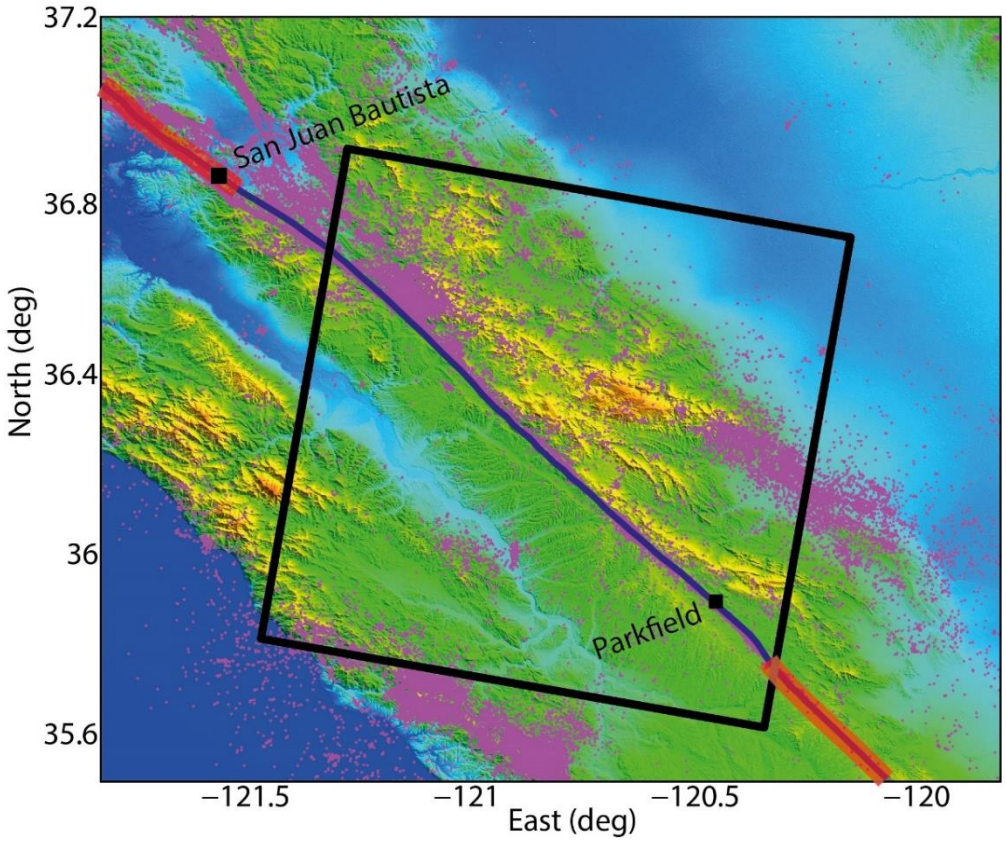

Figure 1.1. San Andreas fault in central California. The blue line represents trace of the fault, and the magenta dots are the location of microseismicity associated with the central SAF zone between 1984 and 2011 [Waldhauser and Schaff, 2008]. The black rectangle outlines the area covered by the SAR images used in CHAPTER 2, acquired from track 27 of Envisat and ERS satellites (Heading angle = 192°, Incidence angle = 23°). The northern and southern red shaded areas indicate the rupture zone of the 1906 Mw7.9 San Francisco and the 1857 Mw7.9 Fort Tejon earthquakes, respectively.

distance from the fault suggests that either strain accumulates on the seismogenic zone of the CSAF or on the sub-parallel fault strands, or part of the strain is released through off-fault inelastic (permanent) deformation processes, or a combination of them (Titus et al., 2011).

Along the CSAF and deeper than 15 km, the number of microseismicity significantly drops, which is an indicator of transition from brittle to ductile deformation at this depth (Rolandone et al., 2008). The creep rate models obtained from inversion of GPS data along the CSAF suggests shallow creep rate of up to 28 mm/year, which increases to 34.5 mm/year at depths greater than 12 km (Rolandone et al., 2008). Studies using a combination of InSAR

velocity maps alongside the data obtained from campaign and continuous GPS sites, while significantly improving the model resolution, yield 33 ± 3 mm/year creep rate for the deep zone with a generally lower rate in the shallow seismogenic zone (Maurer & Johnson, 2014; Ryder & Bürgmann, 2008). In terms of moment accumulation on the CSAF, Ryder and Bürgmann (2008) suggests that a moderate earthquake with M_w 5.7 - 5.9 can release the annual accumulated stress. This is equivalent to a M_w 7.2 - 7.4 earthquake over a period of 150 years. A recent study found a potential locked area where formerly believed to be stable, and upgrades the estimated moment deficit to be equivalent to a M_w 6.5 earthquake, if the entire CSAF rupture in a single earthquake (Maurer & Johnson, 2014). Furthermore, using a Bayesian approach, Jolivet et al. (2015b) estimated the spatial distribution of creep rate and its probability density function along the CSAF. They inferred heterogeneous distribution of the fault coupling in a probabilistic sense.

1.2. Time-Dependent Creep on Central San Andreas Fault

It is broadly assumed that the CSAF creeps at a relatively constant rate, varying merely in the spatial extent of the fault segment. This assumption is in agreement with the findings revealing that the average surface creep rates remained systematically unchanged over the course of past 40 years (Titus et al., 2006). Based on this idea, previous geodetic and seismic studies on the CSAF focused only on the spatial distribution of creep rate (e.g., Jolivet et al., 2015b; Maurer & Johnson, 2014; Rolandone et al., 2008; Ryder & Bürgmann, 2008). Insufficient spatiotemporal resolution of the surface deformation data, non-uniqueness of the inverse problems and incompleteness of the Green's functions are the key limiting factors to estimate temporal variations of creep along the CSAF. To improve the spatial resolutions, advanced geodetic techniques, such as InSAR time series can be applied to accurately measure

spatiotemporal surface deformation. Furthermore, the non-uniqueness of the geodetic inversion results can be mitigated by integrating seismic or geologic auxiliary information. However, the obtained results would still suffer from simplified Green's functions (e.g., homogenous elasticity, fault geometry, etc.), which may have a significant impact on the uncertainty of the slip models (Duputel et al., 2014).

Thus far, estimates of time-dependent creep on the CSAF has been limited to seismological data, which can be considered as a direct measurement of creep on the fault. Investigating the seismic moments and repeat times of small characteristically repeating earthquakes (CREs), Nadeau and McEvilly (2004) estimated spatiotemporal variation of aseismic slip on the CSAF. They found creep rate is not constant along the CSAF and has a pulse-like temporal behavior. These observations suggest that seismic hazard along the CSAF varies in time as well as space. Temporal variations in fault creep rate, known as slow slip events (SSEs), have also been observed elsewhere, such as on the Hayward Fault (HF) in the San Francisco Bay area, using the data from alignment arrays and creepmeters (Lienkaemper et al., 2012). Furthermore, transient creep events are also recognized using the baseline length monitoring along the transition zone between CSAF and the southeastern locked parts of the SAF (e.g., Gao et al., 2000; Murray & Segall, 2005). These accelerating creep events, exceeding the long-term geodetic rates by ~15 mm/year, are believed to play an important role in releasing the accumulated strain in these partially locked parts of the SAF (Murray & Segall, 2005). Moreover, Shirzaei and Bürgmann (2013) inverted 18 years of surface creep data and InSAR time series to solve for the spatiotemporal distribution of creep on the HF. They found that the creep rate varies in both time and space, suggesting a possible interaction between creeping and locked areas. This highlights the importance of time-dependent creep models for constraining spatially and temporally variable seismic hazards. Therefore, a high-resolution

time-dependent model of creep on the CSAF will significantly enhance our understanding of aseismic and seismic faulting processes and contribute to seismic hazard estimates on SAF. Moreover, spatiotemporal creep distribution on the CSAF allows investigating whether the accumulated elastic strain is released through quasi-periodic accelerated creep event. Using the time-dependent creep model, the scaling relationship that is widely used for inferring deep fault creep rates from the CREs (Nadeau & McEvilly, 2004) can also be refined.

In CHAPTER 2, a time-dependent model on CSAF is obtained using geodetic and seismic data set between 2003 - 2010 and the results are discussed to gain an insight on the temporal behavior of creep (Khoshmanesh et al., 2015). The time-dependent creep model is extended to 1992 - 2010, in CHAPTER 3, to further explore the multiscale characteristics and statistical properties of the fault creep history along the CSAF (Khoshmanesh & Shirzaei, 2018b).

1.3. Slow Slip Events on San Andreas Fault

Fault creep, which accounts for the release of up to half of the seismic moment budget, is a pivotal component of the earthquake cycle (Pacheco et al., 1993). The spatial extent of creep and its rate determine the degree to which a fault is locked and frequency of earthquakes (Chlieh et al., 2014; Perfettini et al., 2010). Moreover, assuming a nearly-constant and continuous creep in time, one can estimate the slip deficit and determine the fault's seismic potential (e.g., Jolivet et al., 2015b; Rolandone et al., 2008). Creeping behavior is mainly attributed to geometrical complexity (Gao & Wang, 2014) and frictional strength of the fault zone material, with the latter in turn depending on lithology (Carpenter et al., 2011; Carpenter et al., 2015; Lockner et al., 2011), temperature (Sibson, 1982), and pore fluid pressure (Kodaira et al., 2004; Rice, 1992). On the other hand, temporary episodes of creep acceleration, known

as SSEs, have been interpreted as earthquake precursors and as possible triggering factor for major earthquakes (Kato et al., 2012; Radiguet et al., 2016; Schurr et al., 2014; Shelly, 2009; Uchida et al., 2016). Ambient stress perturbations due to nearby earthquakes (Shelly et al., 2011; Shirzaei et al., 2013; Wei et al., 2015) and transient pore fluid pressure changes (Rice, 1992) are among the major causes of these creep events. However, recent observations indicate that SSEs can occur semi-periodically in different tectonic settings (Khoshmanesh et al., 2015; Nadeau & McEvilly, 2004; Uchida et al., 2016), which places additional constraints on the underlying mechanism.

The continuous creep on the CSAF is attributed to the frictional weakness, suggested by the lack of elevated heat flow (Williams et al., 2004) and nearly fault-normal orientation of maximum horizontal stress (Zoback et al., 1987). The frictional weakness, likely caused by intrinsic low friction of fault zone material (Carpenter et al., 2011; Carpenter et al., 2015; Lockner et al., 2011) and abnormally elevated pore pressure within the fault core (Fulton & Saffer, 2009; Rice, 1992), suggests that the CSAF is incapable of storing enough strain to generate large earthquakes. Yet, episodic unsteady slip with limited speed in the form of SSEs are observed over entire seismogenic depth of CSAF at semi-regular intervals (Khoshmanesh et al., 2015; Nadeau & McEvilly, 2004), which might modulate the time of seismic events on nearby locked zones. Although the maximum rate of these SSEs does not exceed several times the plate boundary shear strain rate, they share all other characteristics of the well-known SSEs on the subduction zones (Khoshmanesh et al., 2015; Nadeau & McEvilly, 2004). Stress transfer from nearby seismic events (Shelly et al., 2011; Shirzaei et al., 2013; Wei et al., 2015), transient inflow of fluid from depth into seismogenic zone (Rice, 1992), and shallow frictional heterogeneity (Wei et al., 2013) are suggested to trigger SSEs on the CSAF and nearby creeping segments. Availability of dense geodetic and seismic measurements and observations of CSAF

fault properties at San Andreas Fault Observatory at Depth (Carpenter et al., 2011; Carpenter et al., 2015) provide the opportunity to investigate the mechanism that drives SSEs and controls their velocity, duration and repeat time. Evidence for episodic SSEs on CSAF and its interaction with seismicity on surrounding locked segments is provided in CHAPTER 4, and a physically plausible mechanism that explains the occurrence of these events is explored.

1.4. Northeast Japan Subduction Zone

At subduction zones, the general assumption is that seismic rupture and aseismic transients such as afterslip and SSEs are distinct processes that affect different areas of the fault zone (Avouac, 2015). This segmentation is suggested to be driven by geometrical irregularities (Gao & Wang, 2014; Heuret et al., 2012; Tanioka et al., 1997) and frictional properties, which is a function of lithology, temperature (Sawai et al., 2017), and fluid pressure (Kodaira et al., 2004). However, recent observations following the 2016 M_w 7.8 Ecuador earthquake reveal that afterslip and SSE can collocate in the same fault segment (Rolandone et al., 2018). Furthermore, SSEs are also suggested to occur on the shallow segment of northeast Japan subduction zone (NJSZ) that accommodated the large-coseismic-slip (>30 m) of 2011 M_w 9.0 Tohoku earthquake (Ito et al., 2013; Kato et al., 2012; Uchida et al., 2016). One such SSE that initiated ~20 days before the event likely triggered the 2011 quake (Kato et al., 2012). Additionally, the down-dip extent of the NJSZ, which hosted several historic M_w 7+ earthquakes (Shibazaki et al., 2011; Yamanaka & Kikuchi, 2004), also accommodated SSEs (Uchida et al., 2016) as well as up to 3 m afterslip during 15 months following the 2011 M_w 9.0 earthquake (Fukuda et al., 2013; Shirzaei et al., 2014). Coexistence of SSEs and seismicity is also shown for areas near- and off-shore of Iwate Prefecture, which exhibit an increase in the number of M_w 5+ earthquakes during the periodic SSEs (Uchida et al., 2016). These

evidences that distinct processes coincide within same fault area suggest that the microstructures on the subduction zones have far more complex pattern than a binary picture, grossly dividing the fault zone into rate-weakening and rate-strengthening patches (Noda & Lapusta, 2013).

In the binary perspective of subduction zone, the aseismically creeping zones are considered to act as barriers, inhibiting seismic rupture from propagating through. However, depending on the average interseismic coupling, seismic rupture may break into these rupture-impeding patches (Kaneko et al., 2010). Moreover, SSEs can occur on these creeping segments and modulate the timing of earthquakes on the nearby locked segments by transient elevation of imparted shear stress (Khoshmanesh & Shirzaei, 2018a; Schurr et al., 2014). These observations highlight that a successful effort to predict seismic rupture extent and timing requires detailed understanding of the interaction between adjacent macrostructures with distinct long-term behavior. The down-dip segment of large-coseismic-slip of 2011 Tohoku earthquake, near shore of Miyagi Prefecture, is suggested to be creeping during the interseismic period (Weston & Shirzaei, 2016), perhaps in a non-steady manner through periodic SSEs (Uchida et al., 2016). Unlike the megathrust section off-shore of Iwate prefecture, the periodic SSEs on this deep creeping zone does not seem to have a causal relationship with earthquakes on that segment (Uchida et al., 2016). Nonetheless, the relationship between these creep transients and the major earthquakes rupturing the up-dip shallow locked patches remains ambiguous. These deep periodic SSEs are identified in CHAPTER 5 through kinematic modeling of interseismic slip on the NJSZ and their role in earthquake occurrence on the shallow seismogenic portion of the megathrust is investigated. This helps to gain an insight on the microstructure of NJSZ that exhibits such vibrant faulting behavior.

CHAPTER 2.

TIME-DEPENDENT MODEL OF ASEISMIC SLIP ON THE CENTRAL SAN ANDREAS FAULT FROM INSAR TIME SERIES AND REPEATING EARTHQUAKES

The work presented in this chapter has been published as: Khoshmanesh, M., Shirzaei, M., & Nadeau, R. M. (2015). Time-dependent model of aseismic slip on the central San Andreas Fault from InSAR time series and repeating earthquakes. *Journal of Geophysical Research-Solid Earth, 120*(9), 6658-6679. doi: 10.1002/2015JB012039

2.1. Methods

2.1.1. InSAR Time Series

To obtain spatiotemporal measurements of the surface deformation at high resolution, a wavelet-based interferometric synthetic aperture radar (InSAR) time series algorithm, so-called WabInSAR (Shirzaei, 2013) is applied to the radar images. Through this method, considering a threshold for perpendicular and temporal baselines, a large set of interferograms are combined to construct the time series of deformation for individual points. The satellite precise orbit information and a digital elevation model with 90 m resolution from Shuttle Radar Topography Mission are used to isolate the geometrical phase (Franceschetti & Lanari, 1999). A two-dimensional phase unwrapping algorithm proposed by Chen and Zebker (2001) is used to recover the absolute values from ambiguous phase observations. Due to phase decorrelation processes, however, only pixels with useful information should be identified and introduced to the phase unwrapping operator (Costantini & Rosen, 1999). Thus, an elite (i.e., less noisy) pixel identification procedure is implemented, which essentially investigates the time series of the complex interferometric noise. The method for noise estimation is based on

wavelet packet analysis (Goswami & Chan, 1999) of the complex interferometric phase (Lopez-Martinez & Fabregas, 2002). For details on the denoising step and elite pixel identification procedure, see Shirzaei (2013). Each interferogram is also corrected for the effect of orbital error using a first-order spatial polynomial (Shirzaei & Walter, 2011). However, to preserve the long-term interseismic signal in the line-of-sight (LOS) observations, a plane fitted to the Global Positioning System (GPS) velocity measurements is subtracted from and added back to the observations on either side of the fault prior and after orbital error correction step, respectively. The effect of spatially correlated atmospheric delay in all the interferograms is isolated and removed using a filter designed based on Coiflet wavelets of order 5, following a method proposed by Shirzaei and Bürgmann (2012).

Time series of surface displacement in the vicinity of the CSAF is obtained from the unwrapped phase values, using a linear unbiased estimation approach (Bjerhammar, 1973). Low-frequency spatial and high-frequency temporal variations in the time series of surface deformations are removed to mitigate the remaining effect of atmospheric delay. To this end, the InSAR time series is refined using a wavelet-based filter with temporal and spatial window size of 300 days and 4 km, respectively. Surface velocity in the LOS direction is estimated by fitting a line to the final time series of surface deformation using a robust regression algorithm. The result for time series analysis and validations will be presented in section 2.2.1.

2.1.2. Time-Dependent Creep Modeling

To solve for the spatiotemporal distribution of the creep on the CSAF, causing the surface deformation, an inverse modeling scheme is implemented, which uses a combination of Iterative bounded least squares (ILS) and linear Kalman filter (LKF) to minimize the mean errors in both spatial and temporal domain. In this study, it is assumed that the detected

surface deformation is due to pure right-lateral strike slip on triangular patches buried in an elastic, homogenous half-space medium (Meade, 2007). Given $l_t(x, y)$ as the set of surface displacement observed at locations $\{(x_i, y_i)\}_{i=1:n}$, where n is the number of observations sampled at times $t = 1, \ldots, T$ and the fault creep (d_t) at the center of each patch, the following mathematical relation holds:

$$l_t + r_t = Bd_t, \qquad t = 1, 2, \ldots, T \; ; \; P_t = S_0^2 \sum_{l_t l_t}^{-1} \tag{2.1}$$

$$lb_t \leq d_t \leq ub_t$$

$$\|P_t r_t\|_2 \rightarrow min$$

where B is the design matrix containing Green's functions relating the creep on triangular patches to the surface displacements observations with residuals, r_t. The design matrix B also contains the unit vectors mapping the three-dimensional vectors of the surface deformation on the LOS direction. P_t is the diagonal matrix of observations weight in each time step, which is estimated by scaling the variance-covariance matrix of the observations ($\Sigma_{l_t l_t}$) with the primary variance factor (S_0^2). In each time step, the initial variance-covariance matrix of observations (an identity matrix) as well as the primary variance factor are updated, based on the surface LOS deformation residuals in the previous iteration of the ILS procedure, to form the weight matrix. The inequality in equation (2.1) restricts the creep at each time step between lb_t and ub_t as the lower and upper bounds (Mikhail, 1976). The subscript t in all the variables implies that the equation (2.1) is solved separately for each time step. The residual orbital error and offset due to potential error in the reference point are also accounted for, by solving for a ramp and offset alongside other unknowns in each time step.

To obtain an optimum time series of creep on the CSAF, equation (2.1) is solved using an ILS method, which mimics the statistical properties of L1-norm minimization; hence,

assuring that the estimated fault creep is less affected by outliers (Holland & Welsch, 1977). To obtain a smoother slip distribution and deriving a more realistic creep model, a constraint is added to the system of equations that minimizes the second-order spatial derivative of the fault creep (Segall & Harris, 1987):

$$\lambda D d_t = 0 \quad t = 1, 2, \dots, T \tag{2.2}$$

where D is the Laplacian operator. The smoothing factor, λ, is determined using an L curve showing the trade-off between roughness of the creep model and its fit to the surface deformation data. The trade-off curve is estimated at some discrete points, choosing different numbers for λ and solving equations (2.1) and (2.2). The point at which the curvature is maximum represents the optimum smoothing factor. Further details of this method is described in Shirzaei and Bürgmann (2013).

To reduce the temporal noise of the time-dependent creep model, LKF (Grewal & Andrews, 2001) is applied to the estimated time series of aseismic slip. The system dynamics model for the LKF is as follows:

$$\begin{bmatrix} {}_{kf}d_t^i \\ V_t^i \end{bmatrix} = \begin{bmatrix} 1 & \Delta t \\ 0 & 1 \end{bmatrix} \begin{bmatrix} {}_{kf}d_{t-1}^i \\ V_{t-1}^i \end{bmatrix} + \begin{bmatrix} {}_{d}w_{t-1}^i \\ {}_{V}w_{t-1}^i \end{bmatrix}, \tag{2.3}$$

$${}_{d}w_{t-1}^i \sim N\left(0, Q_d^i\right), \qquad {}_{V}w_{t-1}^i \sim N\left(0, Q_V^i\right)$$

where ${}_{kf}d_t^i$ and ${}_{d}w_t^i$, $t = 1,2, \dots, T$, are the vector of unknowns (i.e., time series of creep on the i-th patch) and associated zero-mean Gaussian distributed noise, respectively. This equation explains that each patch creeps with a constant velocity, subject to random velocity perturbations. The measurement model is established as:

$${}_{s}d_t^i = {}_{kf}d_t^i + v_t^i, \quad v_t^i \sim N(0, Q_d^i) \tag{2.4}$$

where, creep for patch i at time step t, ${}_sd_t^i$, obtained in the static inversion step by solving equation (2.1), is used as the vector of observation in the LKF step. The rest of the parameters are estimated as follows:

$$Q_d^i = \frac{1}{T-1}\sum_{t=1}^{T}\left({}_s\sigma_t^i - {}_s\bar{\sigma}^i\right)^2 \tag{2.5}$$

$$Q_V^i = \frac{1}{T-1}\sum_{t=1}^{T}\left(V_t^i - \bar{V}^i\right)^2$$

$${}_s\bar{\sigma}^i = \frac{1}{T}\sum_{t=1}^{T} {}_s\sigma_t^i$$

$$\bar{V}^i = \frac{1}{T}\sum_{t=1}^{T} V_t^i$$

$$V_t^i = \frac{{}_sd_t^i - {}_sd_{t-1}^i}{\Delta t}$$

where Δt is the time interval between consecutive time steps, and ${}_s\sigma_t^i$ is the standard deviation of obtained creep on the patch i at time step t. The system of equations (2.3) and (2.4) has a recursive solution, provided by Grewal and Andrews (2001). Note that the LKF scheme is applied to the time series of creep at each patch separately; therefore, the creep covariance between patches does not propagate into this step. In the following, this framework is applied to the InSAR surface displacement and repeating earthquake time series to model the time-dependent pattern of creep along the CSAF.

2.2. Data and Model Input

2.2.1. InSAR Time Series and Validation

Synthetic aperture radar (SAR) data, which are often acquired routinely on a monthly basis, provides high spatial resolution maps of the ground surface motion. These are a valuable complement to Global Navigation Satellite System measurements for tracking the surface movements. The dataset used in this study includes SAR images acquired in descending orbit (heading = 192°, incidence angle = 23°), track 27 of ERS2 (16 scenes) and Envisat (30 scenes) C-band satellites spanning period 26 March 2003 to 7 July 2010 (Figure 2.1). The surface deformation for more than 700,000 elite pixels is calculated in 46 time steps within this period.

The LOS velocities obtained from multi-temporal analysis of the InSAR dataset (section 2.1.1) alongside the GPS velocities are shown in Figure 2.1a. The solid rectangles denote the location of the GPS stations, which are color-coded based on the GPS velocities projected onto the LOS direction. The black arrows show the horizontal velocity of the GPS stations. Visual comparison of the InSAR LOS velocity and projected GPS velocities shows a good agreement between these two independent data sets. The difference between the GPS and InSAR LOS velocity has an average of -0.2 mm/year and a standard deviation of 1.8 mm/year (inset in Figure 2.1a). The time series of GPS surface deformation, however, is not included in the inversion for two main reasons: First, observations from the continuous GPS stations started in 2006, and second, spatial distribution of these stations is sparse (> 40 km) and may not be affected by near fault creep signal. Thus, including these data sets in the inversion causes an additional level of complexity and requires dealing with spatially and temporally heterogeneous data weights.

The trace of the SAF clearly defines the boundary between the red and blue areas in Figure 2.1a, which correspond to movement toward and away from the satellite, respectively.

Given the profiles marked by yellow dashed line in Figure 2.1a, the InSAR surface deformation velocities measured within ~10 km distance of either side of these profiles are plotted in

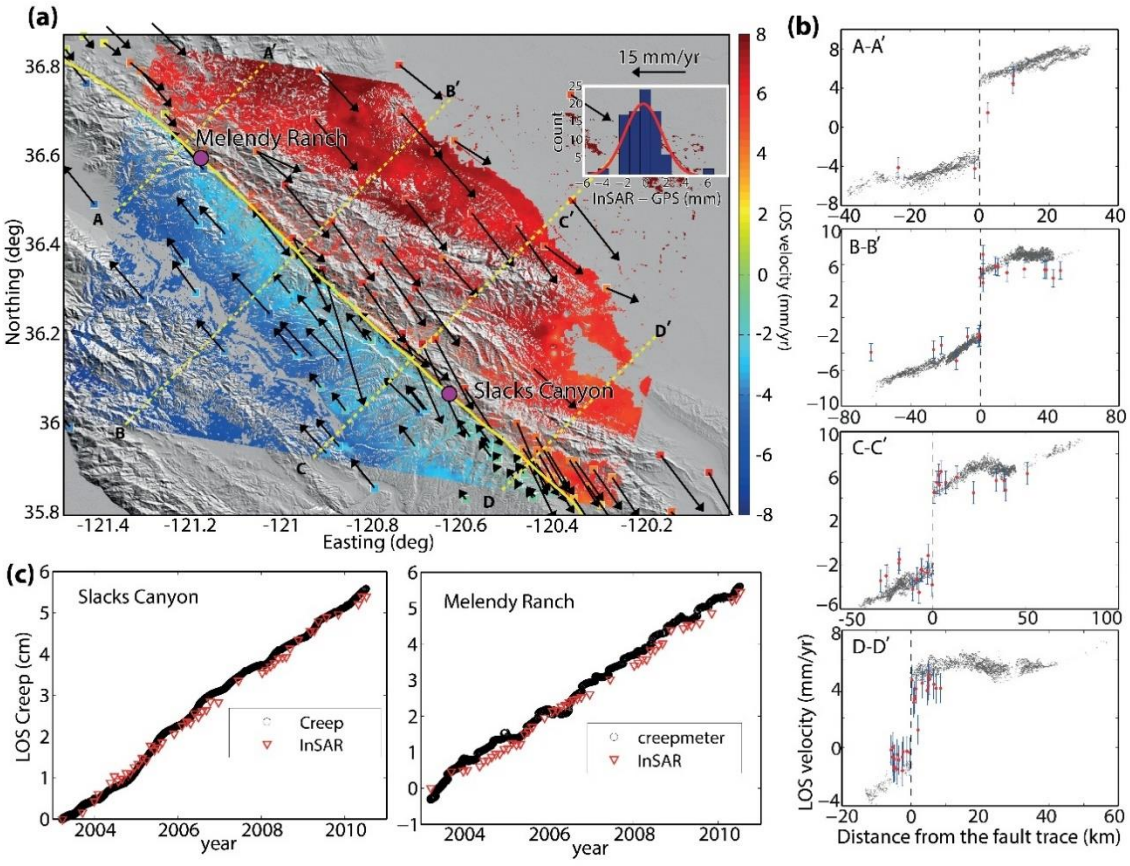

Figure 2.1. InSAR observations on central San Andreas Fault and validation. (a) InSAR LOS linear velocity obtained from WabInSAR analysis of the ERS and Envisat data (track 27) over the CSAF between 2003 and 2011. The GPS velocity vectors (black arrows) and their projection onto the radar LOS is shown to provide a comparison between InSAR and GPS data. The rectangles are color-coded by the amount of GPS horizontal velocity projected onto the LOS direction. The solid yellow line illustrates the trace of the SAF. Location of the Slacks Canyon and Melendy Ranch creepmeter stations are shown by magenta circles on the fault trace. The inset is a histogram showing the difference between GPS and InSAR data and the normal distribution fit to the histogram. (b) The InSAR surface velocities (gray dots) within ~10 km distance of either side of the profiles (A-A', B-B', C-C', and D-D'). Red dots represent the corresponding amount of surface deformation measured by the GPS stations with blue-colored error bars showing 1 mm/year uncertainty (c) Comparison between InSAR surface creep time series and the creep obtained using creepmeters located at Slacks Canyon and Melendy Ranch stations. The creep time series are projected onto the radar LOS for comparison with the InSAR data.

Figure 2.1b. The equivalent surface LOS deformation measured by the GPS stations (red dots) is also shown. For each GPS station, a 1 mm/year error bar, representing one-sigma uncertainty (blue bars) is provided. Except for a handful of stations, there is an overall good agreement between InSAR and GPS observations. The occasional discrepancy is likely caused by the non-tectonic vertical signals that only affect the InSAR observations. These profiles show large step crossing the fault, which indicates that creep reaches the surface. Moreover, away from the fault trace, the variable slope of the deformation profiles suggests that despite abundant creep, the CSAF also accumulates strain, with magnitude varying along the fault trace.

To further validate the generated InSAR time series, they are compared with direct measurements of the creep along the fault trace, obtained using creepmeters stations. The locations of the two creepmeter stations are shown with the magenta circles along the CSAF in Figure 2.1a. The comparison shows that there is a good agreement between obtained InSAR creep time series and in situ measurements of the creep (Figure 2.1c). Note that the observed backward creep motions at Melendy Ranch station are likely due to station settlement, measurement artefacts, or other non-tectonic processes. In summary, the validation tests with GPS and creepmeter data indicates that the presented multitemporal InSAR processing method is robust, and the obtained surface deformation is accurate.

To make the inversion more amenable, a downsampling method similar to Quadtree algorithm (Jónsson et al., 2002), but suitable for irregularly sampled data, is applied to the InSAR observations. This approach iteratively downsamples a large InSAR LOS data set to a smaller data set, while preserving the quality of the original data set. In this approach, similar to the method proposed by Gonzalez et al. (2010), within each iteration triangles are formed using the Delaunay algorithm and the observations at three vertices are used to estimate the

standard deviation of the LOS velocities. Data points forming triangles with a standard deviation less than a certain value are eliminated. This method is implemented iteratively until either the standard deviation of the LOS velocity for all the remaining triangles exceeds the threshold, or the number of remaining points reduces to less than a predefined number. Since the focus here is to obtain the shallow creep on the CSAF, which has a greater contribution to the deformation of the points located near the fault trace, the data points are divided into two subsets, near-field and far-field. The near-field subset, comprising the data points within ~20 km distance from the fault trace, is downsampled to less than 5000 points. The remaining data points, i.e., the far-field subset, are downsampled to less than 1000 points.

2.2.2. Fault Geometry

In this study, pure right-lateral strike slip on a three-dimensional surface representing the CSAF, which is composed of triangular patches embedded in an elastic, homogenous half-space medium, is assumed as the source of detected deformation on the surface. Microseismicity in the study area is used to determine the optimum representative three-dimensional fault geometry (R. Simpson, personal communication, 2012). Figure 2.2 shows a three-dimensional view of the fault model, color-coded based on the dip angle of the triangular patches. Also, the locations of microseismicity in the vicinity of the CSAF are shown for the period of 1984-2011 (Waldhauser & Schaff, 2008). The blue curve shows the average perpendicular distance of the microseismicity from the fault surface. The concentration of microseismicity (low perpendicular distance) near the trace of the fault in the central section of the CSAF (Figure 2.2) suggests that this fault segment is almost freely creeping. Moving toward the transition parts of the fault, further northwest or southeast, the perpendicular distance of microseismicity increases significantly, especially toward the San Juan Bautista in

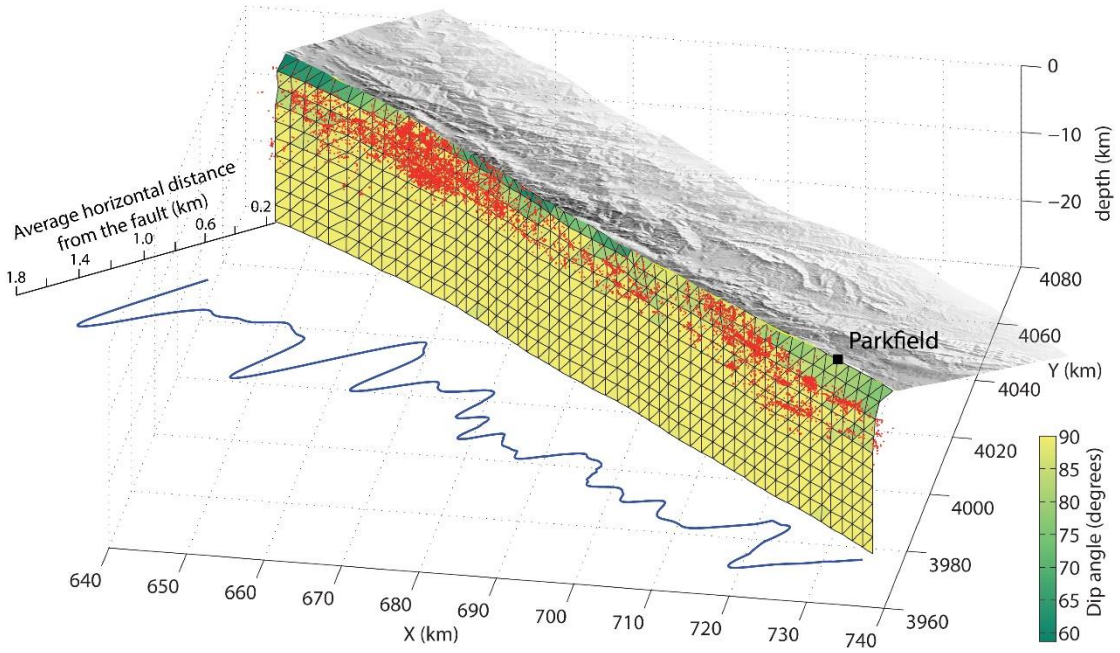

Figure 2.2. Three-dimensional geometry of central San Andreas Fault. The figure is color-coded based on the dip angle of each triangular patch. The red dots show the epicenters of microseismicity along the CSAF between 1984 and 2011 [Waldhauser and Schaff, 2008]. The blue curve shows the average perpendicular distance of the microseismicity from the fault surface.

the northwest. This suggests that coupling of the fault increases moving toward two termini of the study area. Moreover, no microseismicity is detected for depths more than 15km, implying a transition to ductile zone of the fault.

2.2.3. Characteristically Repeating Earthquake

Characteristically Repeating Earthquakes (CREs) are sequences of microseismic events with highly similar seismic waveforms (cross-correlation coefficients >98%) and moment magnitudes (± 0.1 M_w), suggesting quasi-periodic events occurring on the same patch. Generally, these asperities occupy less than 1% of the active fault surface (Nadeau et al., 1995; Nadeau & Johnson, 1998) and are surrounded by areas that slip aseismically. The adjacent creep loads these asperities and causes periodic failure. Recurrence intervals of these events is

inversely proportional to the creep rate on the surrounding fault patches (Nadeau & Johnson, 1998; Schaff et al., 1998). The seismic moment release provides quantitative information about the area of the fault surface and the amount of slip involved in these seismic events. The following relationship associates the amount of creep (d) on the surrounding area, during the period between two consecutive events of the same CRE sequence, to the seismic moment (M_0) (Nadeau & Johnson, 1998):

$$d = 10^{\alpha} M_0^{\beta} \tag{2.6}$$

where, $\alpha = -2.36$ and $\beta = 0.17$ are constants that are estimated through empirical calibration, using long-term spatially averaged CREs and geodetic slip rate data (Nadeau & Johnson, 1998).

More than 630 CRE sequences were detected between 2003 and 2011 along the creeping segment of the SAF, with an average of ~eight events per sequence. The slip obtained using 4900 individual repeating earthquakes is used in this study. Figure 2.3 represents the spatial distribution and the associated long-term slip rate of these CRE sequences. To obtain the amount of CRE creep at the time of each SAR acquisitions, a temporal interpolation scheme is applied. The creep time series obtained from CREs has a quasi-linear pattern in the absence of coseismic or postseismic contributions. Figure 2.3b and c provide two examples of such sequences, located inside the black rectangle shown in Figure 2.3a. However, over the southeastern segment of the CSAF, which is affected by afterslip due to the 2004 Parkfield earthquake, CRE creep shows a logarithmic pattern. Figure 2.3d and e show the time series of creep obtained from two of the CRE sequences located in this area (inside the red rectangles shown in Figure 2.3a). To account for the behavioral differences of the CRE sequences through time, an interpolation function comprised of linear and logarithmic functions is considered. The logarithmic term has the form:

$$d(t) = a \log(bt/a + 1) \tag{2.7}$$

where, $a = V_0 t_r$ with V_0 as the long-term slip rate and t_r as the relaxation time, and b is the afterslip velocity. This equation describes frictional afterslip, under two assumptions: First, that stress grows with increase in the logarithm of sliding velocity in a linear fashion, and second, the contribution from ongoing plate convergence and viscoelastic relaxation in upper mantle and lower crust are negligible (Marone, 1998). Estimating the coefficients a and b using the CRE-determined creep, allows calculation of creep at each arbitrary time step. To identify

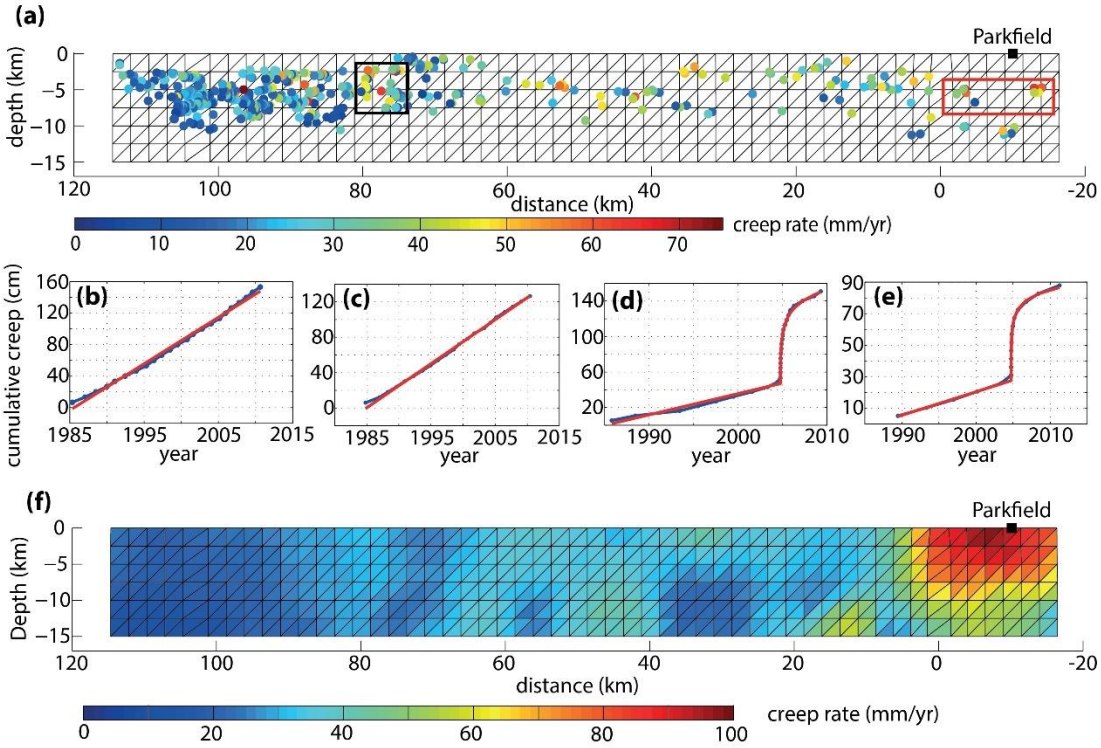

Figure 2.3. Characteristically repeating earthquake data set. (a) The CSAF and location of CRE sequences color-coded based on the estimated long-term creep velocity for each sequence. (b, c) Time series of the cumulative creep obtained from two of the CRE sequences in the absence of coseismic and postseismic effects (blue curve). The red curve is the creep obtained using temporal interpolation. These two sequences are located inside the black rectangle. (d, e) Time series of cumulative slip obtained from two of the CRE sequences located close to Parkfield (blue curve). The red curve shows the fitted curve for temporal interpolation. The location of these two sequences is inside the red rectangle. (f) Map of the long-term creep rate obtained following spatially and temporally interpolating the creep associated with CRE sequences.

the CRE sequences affected by the afterslip, and thus showing the logarithmic pattern, the CRE-derived short-term creep rate between each consecutive time step is estimated. The sequences with maximum creep rate, exceeding a certain value are picked as the ones affected by the afterslip and are temporally interpolated using the equation (2.7). The threshold is estimated through series of trial and error with the objective to minimize the misfit between the interpolated and original creep time series. A linear function is used to interpolate all the CRE sequences, for the time steps prior to the 2004 Parkfield earthquake. The total mean value of the misfit following the temporal interpolation is -0.3 mm with a standard deviation of 23 mm. The interpolated CRE creep (red curves) in Figure 2.3b-e show a very good fit to the original creep time series (blue curve).

In the next step, the temporally interpolated CRE-determined creep is spatially interpolated to derive the amount of CRE-determined creep on each triangular patch. The amount of creep on each patch is estimated as the average of the creep associated with CREs located within a 5 km radius distance. Given the distribution of the CREs, we have tested various interpolation distances and found that 5 km radius provide a balance between smoothness and the coverage. This means that while a CRE-derived creep is assigned to each patch along the fault, the creep distribution is not oversmoothed. Figure 2.3f shows the spatial distribution of CRE long-term creep rate on the CSAF, estimated as the slope of best-fitting line the time series of creep at each patch. Part of the fault close to Parkfield shows the maximum creep rate of up to 100 mm/year because of accelerated afterslip creep due to the 2004 Parkfield earthquake. In the central section of the CSAF, except for a small slow creeping zone located at 5 km depth between km 25 and 40, most of the fault from km 0 to 70 creeps with a rate up to 45 mm/year. Toward the northwest, the creep rate drops to less than 10 mm/year, highlighting the transition to the surrounding locked segments of the SAF. Notably,

the higher density of the CRE sequences along this part of the fault (Figure 2.3a) leads to a more reliable spatially interpolated CRE creep.

2.3. Model Results

Applying the time-dependent inversion scheme, detailed in section 2.1.2, to the time series of InSAR surface deformation (section 2.2.1) and the interpolated CRE creeps (section 2.2.3), here the aim is to solve for the spatiotemporal distribution of the creep along the CSAF. The static inversion of InSAR deformation data using the ILS method is followed by applying LKF to reduce the temporal noise of the creep model and derive the final map of the creep along the CSAF. To remove the effect of deep dislocation from the surface observations, an infinite freely creeping zone starting from 25 km depth, continuing down to 3000 km is considered. This deep dislocation zone is considered to creep with long-term rate of 34.5 mm/year following (Rolandone et al., 2008).

To integrate the CRE observations into the creep inversion, the bounds on inverted fault creep are defined using interpolated CRE-determined creep (equation (2.1)). To examine the effect of this bound on the inversion results, two different scenarios are tested, including: 1) zero as the lower bound, and upper bound is 20% more than that of the CRE creep, and 2) lower and upper bounds are 50% and 20% less and more than that of the CRE creep, respectively. Given that the CREs occur in the shallow zone of the fault (surface to 15 km depth), a transition zone to the ductile deformation is defined at depth of 15 km to 25 km, which is allowed to creep at a rate up to the long-term creep rate. More details, further clarifying this procedure are provided in the Appendix A and Figure A.1.

To estimate the smoothing factor, the cumulative InSAR surface deformation for the entire time series is used and the same value is applied throughout the time-dependent

inversion. Figure 2.4a and b show the trade-off curve obtained for each scenario. The optimum smoothing factor is estimated to be 2.4 and 8.3, for the first and second scenario, respectively.

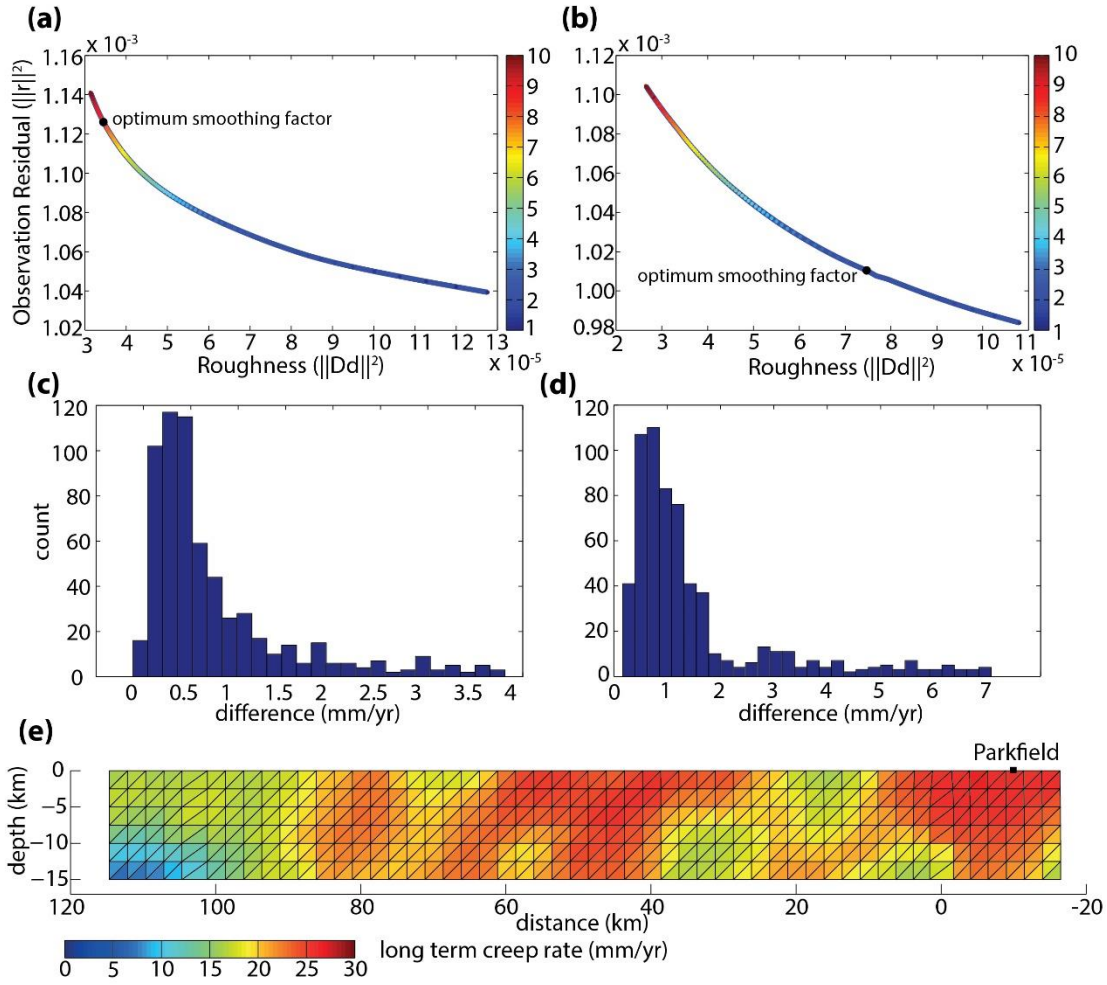

Figure 2.4. Trade-off curve used to estimate the optimum smoothing factor implementing (a) scenario #1, and (b) scenario #2. (c) The histogram of the difference between the long-term creep rate obtained by implementing the scenario #1 and the CRE observations. (d) The same histogram obtained following implementing the scenario #2. (e) Long-term creep rate obtained implementing scenario #1.

The preferred scenario is chosen based on the root-mean-square error (RMSE) of the model fit to InSAR deformation data and CRE-determined creep, in each scenario. Accordingly, the estimated RMSE for InSAR LOS velocity of the first and second scenarios are 1 and 1.3 mm/year, respectively. Although the fit to the surface deformation data is equally

well in both scenarios, the creep model in the second scenario deviates less from the creep measured using CREs. Figure 2.4c and d show the histograms of the difference between creep models and the CRE observations for each scenario. The histograms have average and skewness of 1.52 mm/year and 2.02 for first scenario and 0.75 mm/yr and 1.95 for the second, respectively. Visual inspection of the results also confirms that the obtained creep rate in the first scenario (Figure 2.4e) is generally less than that of CREs, especially in the areas close to the Parkfield, while the second scenario (Figure 2.4b) provides a better match. Therefore, the scenario #2 is chosen to invert the entire dataset and perform the time-dependent creep modeling.

Figure 2.5a shows the three-dimensional perspective of the CSAF creep rate from the optimum time-dependent model. This figure also represents the time series of creep for various patches along the fault. The distribution of the obtained creep rate is generally similar to that obtained in earlier studies (e.g., Jolivet et al., 2015b; Rolandone et al., 2008; Ryder & Bürgmann, 2008) while the spatiotemporal map of creep model includes unique features, such as afterslip of the 2004 Parkfield earthquake affecting the southeastern part of the fault. The logarithmic pattern of the creep time series over patches near Parkfield is due to the ongoing afterslip triggered by this event. This accelerated creep was not pronounced in the inversion results of the first scenario (Figure 2.4e). This implies that our InSAR data did not entirely capture the near-surface deformation due to the afterslip in the vicinity of this area. Using tighter bounds based on the CRE model, in the scenario #2, enabled mapping of the accelerated creep along the fault in the Parkfield area. This example highlights the complementary nature of these independent data sets for estimating spatiotemporal model of creep.

A two-dimensional map of the long-term creep rate along the CSAF, is presented in Figure 2.5b. Given the large amount of afterslip, the creep on the fault segment close to

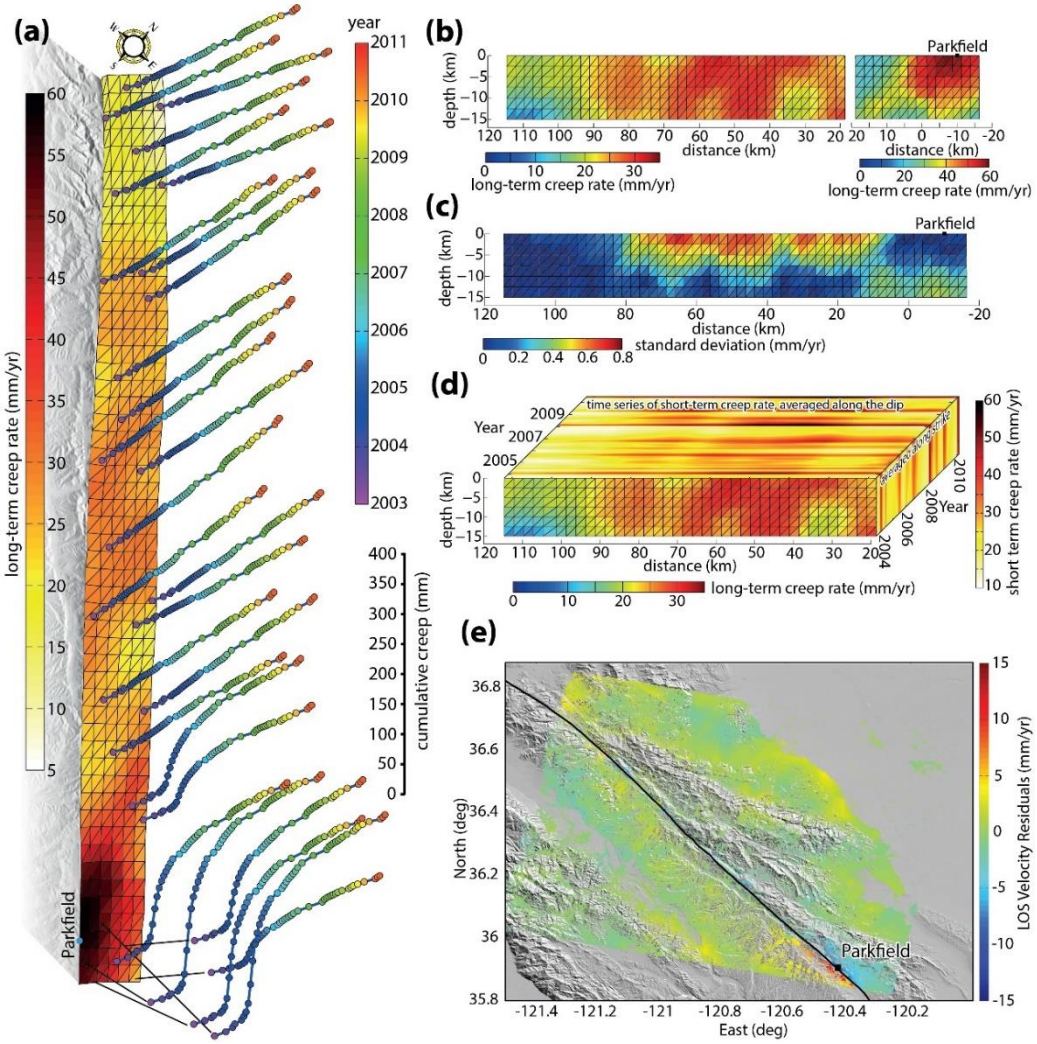

Figure 2.5. Results of time-dependent creep model along central San Andreas Fault. (a) Three-dimensional perspective of the CSAF color-coded based on the long-term creep rate obtained from the time-dependent inversion and examples of the creep time series associated with various patches along the fault. (b) Long-term creep rate along the CSAF in a two-dimensional view. (c) Model uncertainty in the form of standard deviation of creep due to random error observation, estimated through a bootstrapping method. (d) Average creep rate at the patches of the CSAF far from Parkfield and, thus, not affected by the afterslip. The top and right panel show the time series of short-term creep rate estimated between consecutive time steps, and averaged along the dip and strike of the fault, respectively. (e) LOS velocity residuals (observed - modeled) for the optimum time-dependent model obtained following scenario #2. The black line is the trace of the CSAF.

Parkfield is color-coded differently to allow identifying smaller creep rate variations elsewhere. The map of the creep rate reveals that the 30 km central section (km 40 to 70) creeps with the highest rate, up to 32 mm/year in some patches, in agreement with earlier works (e.g., Ryder & Bürgmann, 2008). Though, within this creeping central section, there is a small zone (km 55 to 62 and depth >10 km) with a creep rate as low as 25 mm/year. North of this region (>75 km) the creep rate decreases from almost 30 mm/year to less than 10 mm/year. This finding is consistent with that suggested by Rolandone et al. (2008) and Jolivet et al. (2015b), though the obtained time-dependent model here estimates a slightly lower creep rate for the northwestern segment relative to the central fast creeping zone. The obtained results for northwestern segment of the fault is not evident in the model suggested by Ryder and Bürgmann (2008) and is dissimilar to the recent model of the CSAF estimated by Maurer and Johnson (2014), which suggests a creep rate similar to the central section for this part of the fault. The southeast part of the CSAF (km -15 to -5) shows up to 60 mm/year creep rate, largely due to the 2004 Parkfield earthquake afterslip. Moreover, in contrary to the model by Jolivet et al. (2015b), there is a general increasing pattern of creep rate moving from depth to the surface, in our time-dependent creep model.

Figure 2.5d shows another two-dimensional map of the long-term creep rate along the CSAF, but excludes the parts affected by the 2004 Parkfield earthquake afterslip. Additionally, the time series of short-term creep rate, estimated between consecutive time steps, averaged along the strike and dip of the fault, is represented as a panel to the right side and on top of the long-term creep rate map, respectively. These results suggest temporal variation in the short-term creep rate ranging between 10 to 60 mm/year for most of the fault. These temporal variations of the creep rate will be further discussed in section 2.4.4.

Figure 2.5e illustrates the LOS velocity residuals (observed - modeled) at the location of the original InSAR elite pixels. This figure shows that the LOS velocity residuals of optimum time-dependent model vary between -3 to 3 mm/year for almost the entire study area. Maximum residuals occur near the area affected by the 2004 Parkfield earthquake shallow afterslip. One likely reason for this localized high residual is the constraints provided by the CRE-derived creep rates, which causes overestimation of the creep rate on the shallow patches near Parkfield (from zero to ~ −15 km distance and 0 to 2.5 km depth). Phase unwrapping errors and edge effects can be other possible sources of large misfit, which again, emphasizes the complementary nature of the InSAR surface deformation and CRE creep observations to obtain accurate models of the fault creep.

2.3.1. Model Uncertainty

The uncertainty of creep model stems from observations error and incompleteness of Green's functions. Sophisticated approaches such as Bayesian statistics are used to jointly investigate these effects (Duputel et al., 2014). However, here simpler, yet widely used approaches, such as bootstrapping (Efron & Tibshirani, 1993) and variance-covariance analysis (Mikhail, 1976) are used to investigate the effects of these two sources of error. To quantify the effect of observation error on the creep model, bootstrapping approach (Murray & Segall, 2002) is used. Bootstrap procedure provides a tool to estimate the standard error of unknowns, which involves choosing random samples with replacement from the observations and analyzing each sample to estimate the unknowns (Efron & Tibshirani, 1993). Though the effect of observation error is a function of time, for simplicity, here only the effect of this error on the creep rate model is investigated. Through the bootstrapping procedure, the inversion procedure is repeated many times (here 500), by using random samples of the

observations, to obtain an ensemble of the creep rate. During iterations, a random error with zero mean and 1 mm/year standard deviation is added to the surface deformation velocities. Then using the inversion approach detailed in section 2.1.2, these observations are inverted to obtain the associated creep rate model. Following 500 iterations, a probability density function (PDF) for creep rate on each patch can be estimated. Given the linearity of the problem, this PDF mimics the normal distribution function. The distribution of the standard deviation of this PDF along the CSAF is shown in Figure 2.5c. The result suggests that the maximum sensitivity to the observation random error occurs at the patches located on the shallow part of the CSAF, where the standard deviation reaches up to 0.8 mm/yr. Moreover, although the InSAR surface deformation time series are corrected for the spatially correlated errors (e.g., the effect of atmospheric delay) through the implemented multitemporal InSAR processing algorithm (see section 2.1.1), nonetheless, the effect of residual colored noise that is not accounted for is further investigated. The results for this analysis are presented in Appendix B and Figures B.1 to B.10. The results show that despite presence of the residual correlated noise, the standard deviation of creep time series is less than 1 mm. Since the short-term creep rate varies up to 50% of the long-term rate through time (as it will be shown in section 2.4.4), the uncertainty due to colored noise is also negligible. Note that these estimates are, however, a lower bound for the model error, as the surface observations are often contaminated by other sources of the error that are less known yet have more complex spatiotemporal behaviors.

The second source of model uncertainty is associated with the incompleteness of the Green's functions that relate the surface displacements to fault dislocations. The incompleteness is a result of simplified fault model, medium elastic properties, and observation

distributions. The effect of Green's functions can be investigated through variance-covariance analysis of the unknowns given by following equation (Mikhail, 1976):

$$Q_d^{InSAR} = (B^T B + \lambda^2 D^T D)^{-1} \quad (2.8)$$

in which, B and D are the design matrix (containing the Green's function) and Laplacian operator, respectively, and λ is the smoothing factor introduced in section 2.1.2. Subscript T and -1 represent the transpose and inverse operator, respectively. The standard deviation of the obtained creep on each patch is estimated as the root of diagonal components of the variance-covariance matrix defined by equation (2.8). Figure 2.6a shows the distribution of

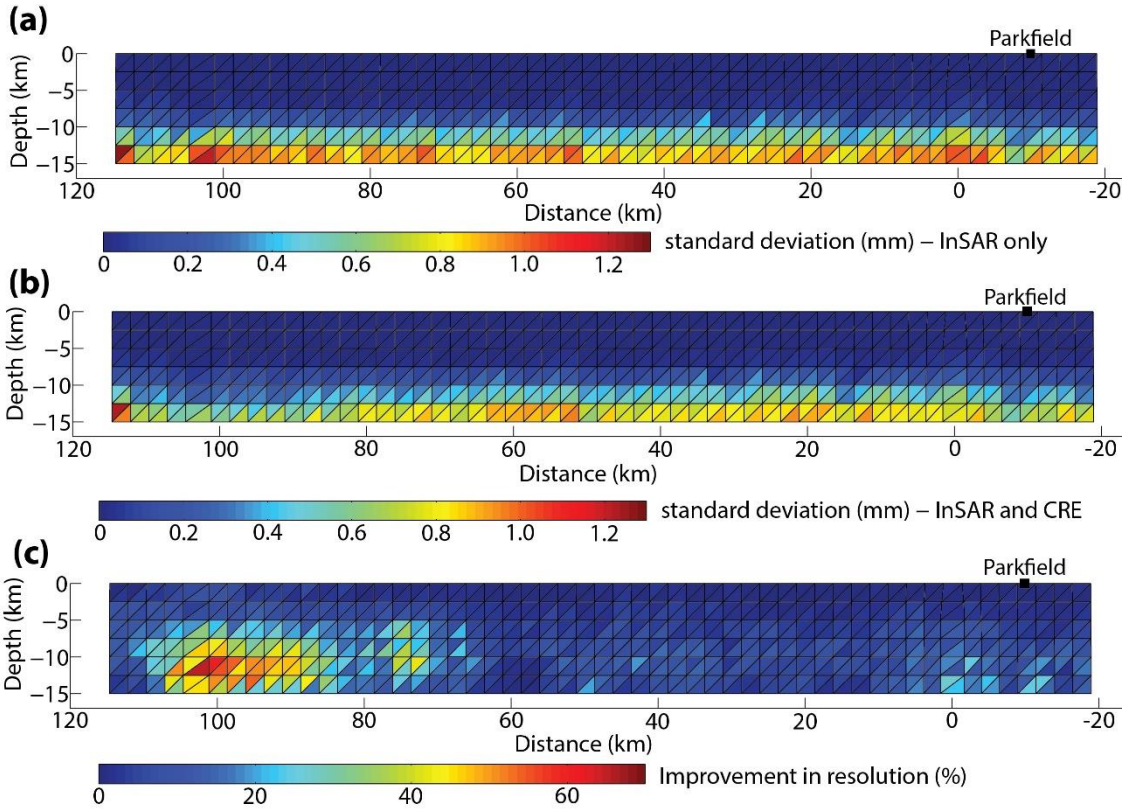

Figure 2.6. Model resolution in the form of standard deviation of the creep due to incompleteness of Green's function, (a) using InSAR surface observations only. (b) Using CRE observations in addition to InSAR data. (c) The model resolution improvement following using CREs.

creep rate standard deviation associated with inverting only InSAR data. This map also resembles the model resolution, as it reflects the ability of model and data in resolving

distribution and amplitude of the fault creep. To further investigate the impact of CREs on the model resolution, another test is performed, where InSAR and CRE data are combined to solve for the creep rate. The associated resolution map in the form of creep rate standard deviation and the improvement over the case of using only InSAR data is shown in Figure 2.6b and c, respectively. As seen, the inclusion of CRE data, improves the model resolution up to 70% at the deeper zone of the fault, to the northwest, where there is a high density of CRE events (Figure 2.3a). These analysis does not address the effects of Earth model heterogeneous elastic properties and simplified fault geometry. Nonetheless, their associated error is only significant when dealing with source model of large earthquakes and thus can be safely ignored here (Duputel et al., 2014).

2.4. Discussion

In this study, a spatiotemporal map of creep along the CSAF is obtained using InSAR deformation time series and CRE creep observations. The map of long-term creep rate along the CSAF, though generally resembling the previous geodetic-based models, also includes several unique features, such as afterslip due to the 2004 Parkfield earthquake affecting the southeastern part of the CSAF. Here, various aspects of the obtained model, its implications and broader impacts will be discussed.

The time-dependent creep model can be used to investigate whether or not the long-term elastic strain is relieved through quasi-periodic accelerated creeps (Nadeau & McEvilly, 2004). The estimates of the earthquake potential and its temporal variations on the CSAF are of great importance for seismic hazard evaluations. Impact of the Calaveras-Paicines fault segment on pattern and magnitude of the creep along the CSAF is also an important topic, which is addressed in this section. The behavior of the short-term creep rate and its relation

to the long-term rates in both time and space is also investigated. The aim is to quantify creep pulsing and its duration as suggested by studies of the CRE creep observations (Nadeau & McEvilly, 2004). The time-dependent creep model is also compared with the creep observation obtained from CRE sequences to refine the scaling relationship linking the CRE moments to the creep on the adjacent fault segments.

2.4.1. Seismic Potential of the CSAF

The moment accumulation rate due to slip deficit along the CSAF is between 4.37×10^{17} and 4.55×10^{17} Nm/year, which is equivalent to a M_w 5.6-5.7 earthquake annually.

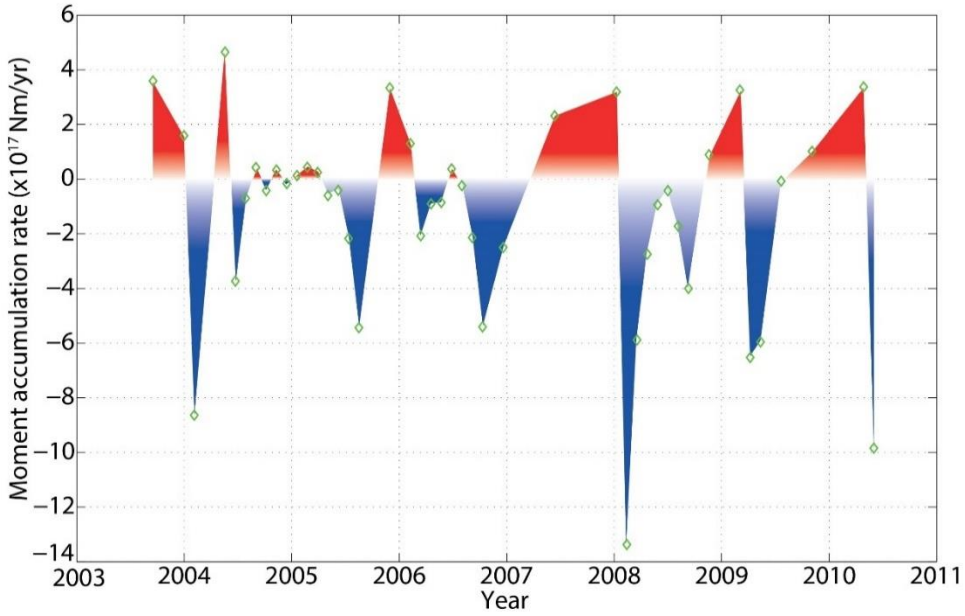

Figure 2.7. Time variation of strain accumulation in the form of the difference between short-term and long-term moment deficit accumulation rate. Red and blue color show the positive and negative difference, respectively.

This rate, which falls into the range reported by Ryder and Bürgmann (2008) is estimated for the patches located far from Parkfield (starting from km ~20) and thus are not affected by the 2004 Parkfield earthquake. Considering the contribution of afterslip due to this earthquake in

the estimated geodetic moment, the moment deficit drops to between 3.44×10^{17} and 3.64×10^{17} Nm/year, equivalent to a magnitude 5.6 earthquake.

Given the variability of the short-term creep rate over the observation period and its deviations from the long-term rates (Figure 2.5d), the short-term geodetic moment accumulation rates along the CSAF is also estimated. Figure 2.7 shows the deviation of the short-term moment accumulation rates from that of long-term for the fault segments not affected by the Parkfield afterslip. The observed differences are characterized by a quasi-periodic pattern with maximum of up to $\sim13\times10^{17}$ Nm/year. Negative differences (i.e., short-term moment accumulation rate smaller than that of long-term) implies the occurrence of accelerating creep exceeding the long-term creep rate. The alternating sign of the moment accumulation difference highlights episodes of strain relief, which in the long-term may change the seismic budget of the fault. Note that this study does not address the question, whether the accumulated strain is released in an event nucleating on the creeping segment, or as a part of a larger event that propagates to the creeping segment from the north or south.

2.4.2. Parkfield afterslip

The slip rate and its type vary along the SAF, in particular near the Parkfield section, where the southern locked section joins the northern creeping segment. The latest major earthquake to the south of CSAF, also rupturing the Parkfield section, was the 1857 M_w7.9 Fort Tejon event (Sieh, 1978). As a transition zone, the surface deformation along the Parkfield segment of SAF is a result of shallow fault creep, hindered by deeper locked asperities (Harris & Segall, 1987; Murray et al., 2001). This segment of the SAF is also well-known for the sequence of M_w 6 events, with the last one occurring in 2004. It is suggested that the coseismic stress change due to the 2004 event triggered the aseismic slip on the

surrounding areas; thus, immediately after the event, the afterslip has dominated the postseismic deformation (Freed, 2007).

The time-dependent model obtained here reveal an accelerated creep due to the afterslip in the southwestern part of the CSAF, near Parkfield, starting right after the event. Based on results, this afterslip mostly affected patches located in the shallow zone of the fault, from the surface to the depth of ~10 km. The spatial distribution of this slip is in agreement with that of earlier studies (e.g., Barbot et al., 2009; Bruhat et al., 2011; Freed, 2007; Johanson et al., 2006). However, the studies that do not include lower crust viscoelastic relaxation, suggest that a considerable part of the afterslip propagated at greater depth (Barbot et al., 2009; Freed, 2007; Johanson et al., 2006), whilst inclusion of the viscoelastic relaxation allows the creep to be shallower (Bruhat et al., 2011). although the obtained model does not account for deep viscoelastic relaxation, the constraints provided by CREs on the creep allow resolution of the afterslip distribution that is consistent with the models that include lower crustal relaxations.

Using the time-dependent model of the afterslip, the coefficients a and b of the equation (2.7) in the section 2.2.3 are also estimated. Assuming 34.5 mm/year long-term creep rate, a fault relaxation time of 1.52 years is estimated for this segment of the fault. This estimate is consistent with the reported relaxation time of ~1.1 year for this and previous events such as the 1966 M_w 6.0 Parkfield earthquake (Bruhat et al., 2011; Marone et al., 1991).

2.4.3. Effect of the Calaveras-Paicines Fault

Another factor that may affect the distribution of the aseismic slip on the CSAF is the presence of Calaveras-Paicines fault, a subparallel fault at the northwestern portion of the

CSAF. Previous studies suggest that creep is divided across this fault segment and the northwestern part of the CSAF (Ryder & Bürgmann, 2008). To investigate the effect of this

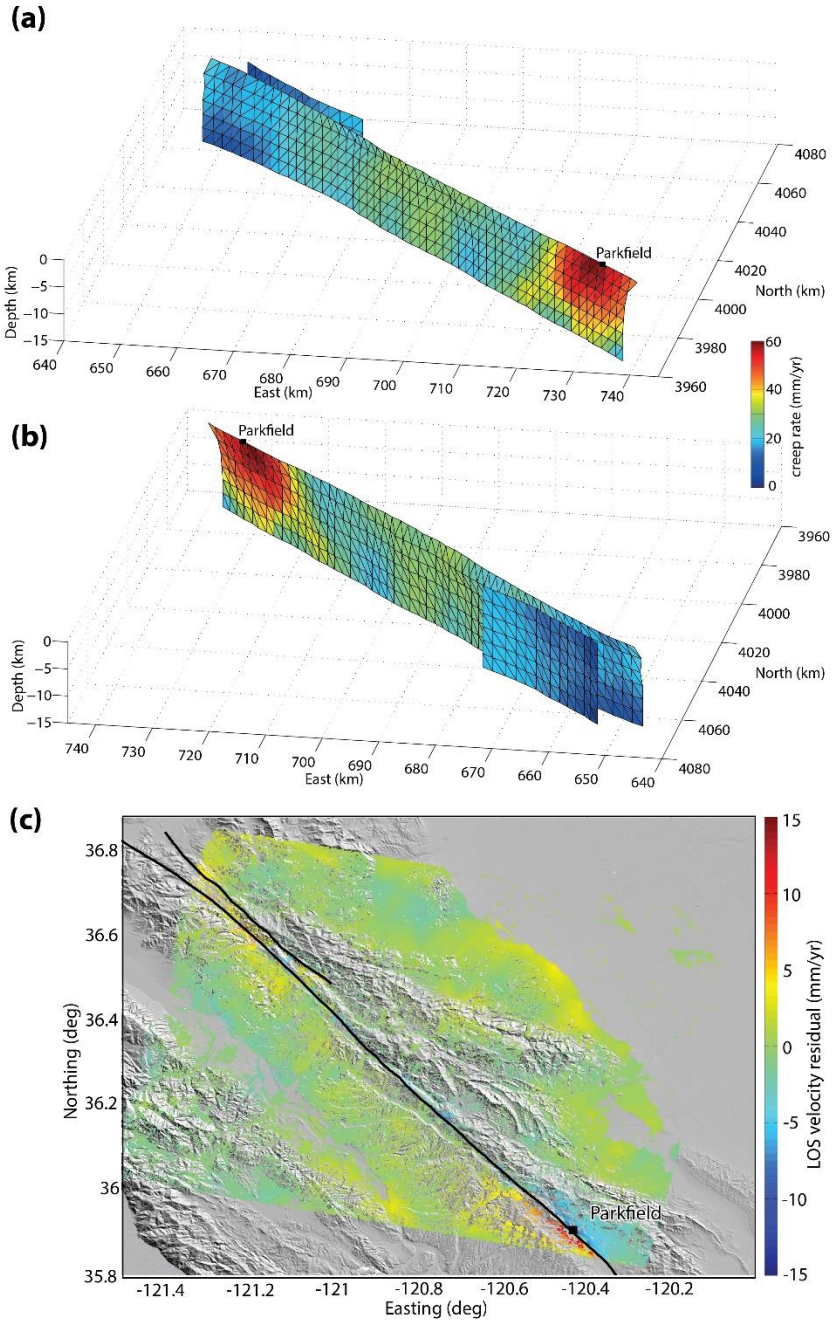

Figure 2.8. Long-term creep rate along the CSAF and Calaveras-Paicines from two different perspectives. (a) View from south. (b) View from north. (c) LOS velocity residuals (observed - modeled) considering the Calaveras-Paicines together with the CSAF. The black lines show the trace of these two faults.

fault segment on creep model along the CSAF, another time-dependent inversion is performed, by including the Calaveras-Paicines segment. During the inversion, the creep on the Calaveras-Paicines fault is constrained such that its long-term creep rate does not exceed 34.5 mm/year. Figure 2.8 presents the results from this test, showing the distribution of the long-term creep rate from two different views.

The model suggests that contribution of the Calaveras-Paicines fault does not have a significant impact on the pattern and magnitude of the creep on the CSAF. However, including the Calaveras segment in the inversion diminishes the model fit to the data (Figure 2.8c), especially in the northwestern part of the study area, where the parallel fault is included. The larger misfit implies that the Calaveras-Paicines fault is nearly locked during the time span of this study, and the estimated slight creep on this fault segment is likely an artifact of the inverse modeling.

2.4.4. Short-Term Creep Rate Behavior

Previous geodetic studies of the creep on the CSAF solved for a constant creep velocity along the fault. However, the time-dependent creep model obtained here (Figure 2.5a and d) shows that creep history varies in both time and space. This suggests that the creep rate undergoes short-term variations. To identify the spatial extent of the creep rate variations along the CSAF, the distribution of creep rate coefficient of variation (COV) is investigated. Creep rate COV is defined as the ratio of standard deviation of the short-term creep rate to the long-term rates for each patch. The patches near Parkfield are exclude from this analysis due to the accelerated creep resulting from afterslip. The results show that the COV distribution changes from 34% to 43% along the creeping segment (Figure 2.9a). The highest

rate variation occurs in the central section (35 to 65 km) that shows the highest amount of long-term creep rate as well.

Earlier work using the deep fault information obtained from sparse sets of CREs revealed patterns of quasi-periodic temporal variation of creep in the form of creep pulses along the CSAF (Nadeau & McEvilly, 2004). Here the obtained high-resolution time-

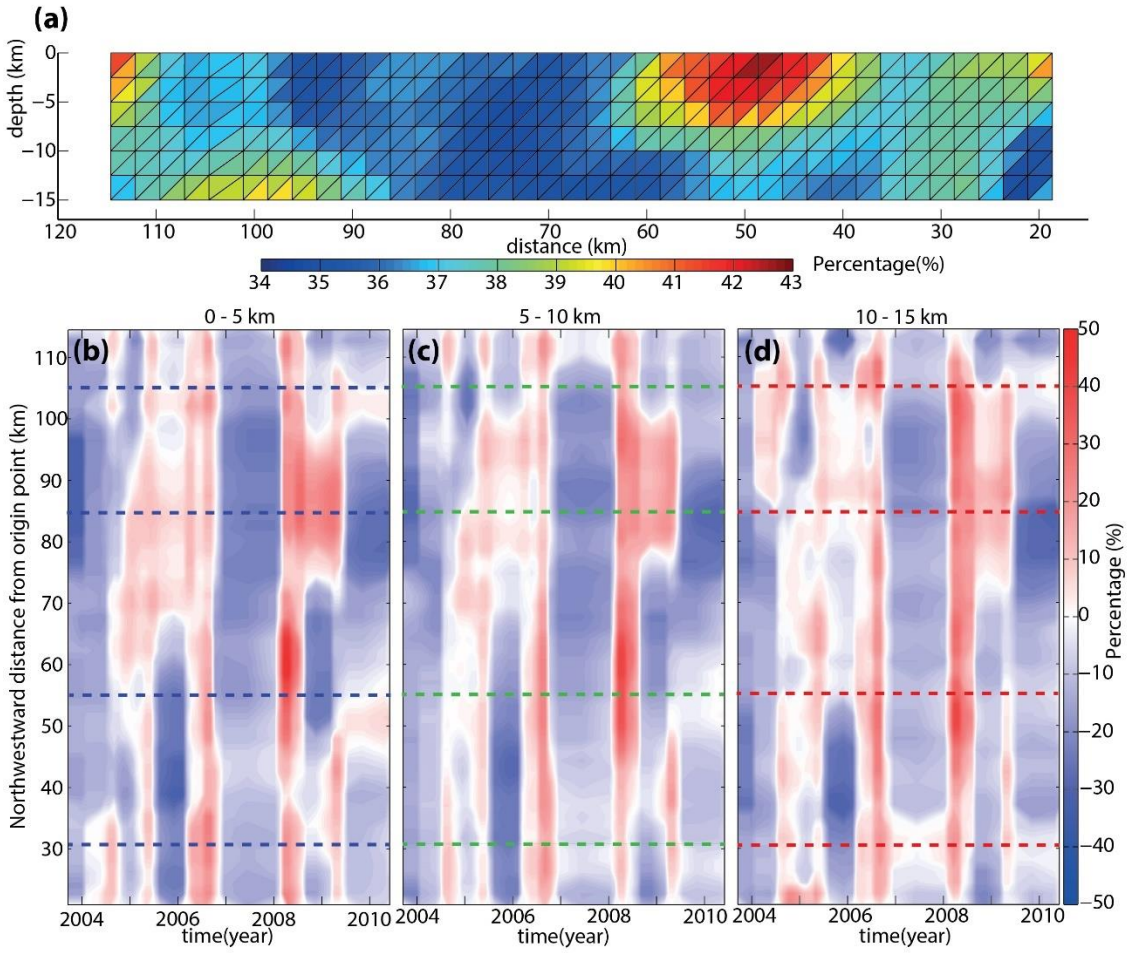

Figure 2.9. Variation of short-term creep rate (a) COV at the patches of the CSAF that are not affected by the afterslip. The difference between the short-term creep rate time series and the long-term, averaged along the dip: (b) 0 km to 5 km depth, (c) 5 km to 10 km., and (d) 10 km to 15 km depth. Dashed lines show the location of profiles presented in Figure 2.10.

dependent creep model is sued to investigate the creep pulsing. To this end, the estimated short-term and long-term creep rates are compared for each patch in the creep model. To

calculate the short-term velocity, a moving window of size ~10 months is used. Figure 2.9 shows the time series of difference between long-term and short-term creep rate, normalized by the long-term rate in percentage. A spatial averaging filter of length ~2 km is also applied to the estimated rate differences. To better investigate the creep rate variations and identify possible depth-dependence, the fault is divided into three different zones by depth: shallow zone from surface to 5 km depth (Figure 2.9b), medium zone from 5 km to 10 km (Figure 2.9c), and deep zone from 10 km to 15 km (Figure 2.9d).

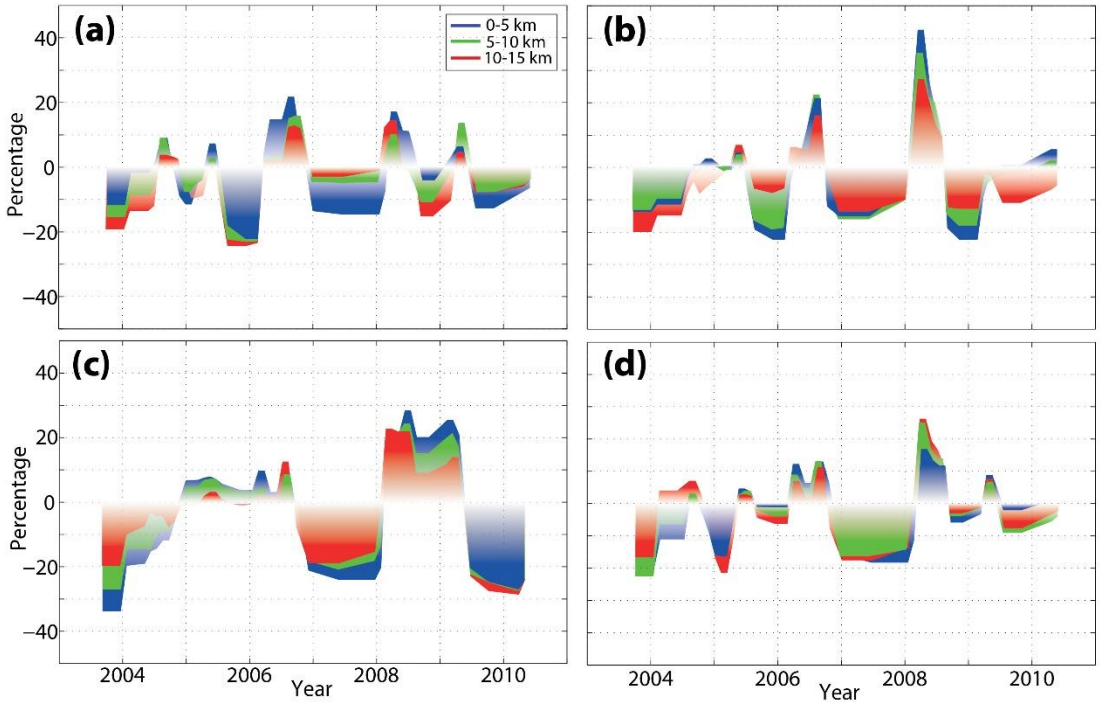

Figure 2.10. Two-dimensional profile of the difference between the time series of short-term creep rate and the long-term rate, averaged along the dip at different locations along the fault (shown with dashed lines in Figure 2.9). Colors corresponds to the profiles for different depth zone; shallow zone (0 to 5 km): blue, medium depth zone (10 to 15 km): green, deepest zone (10 to 15 km): red. (a) 31 km distance. (b) 55 km distance. (c) 85 km distance. (d) 105 km distance from the reference point.

The results confirm presence of pulse-like quasi periodic creep events with repeat time varying along different parts of the CSAF. Variations of the creep rate in each depth zone are also compared along four profiles that their locations are shown in Figure 2.9. These profiles clearly demonstrate variation of the pattern, duration, and amplitude of the creep pulses in

different segments of the fault. As shown in Figure 2.10, the pattern of creep pulses and their repeat time is almost identical for all the depth zones. While the amplitude of pulses generally drops moving toward the ductile zone of the fault. As seen in Figure 2.10a and b, the duration of each creep pulse is between 1 to 2 years for the central creeping parts of the fault (km 20 to 70), in all the depth zones. According to the Figure 2.9a, the central segment that creeps with the fastest long-term rate, shows the largest amount of COV. However, the profile of average creep rate at 85 km distance (Figure 2.10c) shows two distinct pulses of creep with duration of ~3 years. Moreover, Figure 2.10d shows that the pattern of creep pulsing further northwest, at km 105, is similar to that of the central section (km 20 to 70), indicating that a similar mechanism is likely deriving the creep pulses in these two sections. These results are in agreement with the observed ~1.7 and ~3 years cycle duration for creep pulsing obtained from CRE observations for this segment of the SAF (Nadeau & McEvilly, 2004). Another noticeable point is the negative pulse (blue color in Figure 2.9b-d), starting in late 2006 and ending in early 2008, which is evident in all depth zones and along entire the CSAF. It also can be seen that there is a direct relation between the repeat time of pulses and their amplitude. For instance, the maximum amplitude of the pulses occurs in mid-2008 (Figure 11b-d) following the longest duration of negative pulse, starting in late 2006.

To further investigate the effect of relaxing the CRE constraint on the observed creep pulsing, the short-term behavior of the creep model obtained from the first scenario in section 2.3, i.e., no lower bound of inverted creep time series is similarly inspected. The results of this analysis (Figure A.2) provides a pulsing pattern like that of the second scenario. Since, within the first scenario no CRE-derived constraint is applied to the lower bound for the inverted creep, it can be concluded that the creep pulsing is mostly constrained by the InSAR surface deformation observations. Moreover, as mentioned in section 2.2.3, the CRE data is

temporally interpolated using a function which comprises a linear and logarithmic function, and thus, does not contain any periodic component.

Episodic pulses of creep along the CSAF resembles the slow slip events (SSEs), observed to occur periodically in a number of subduction zones such as southwest Japan (Hirose et al., 1999; Miyazaki et al., 2003; Ozawa et al., 2002), Cascadia (Dragert et al., 2001; Miller et al., 2002), and Guerrero in Mexico (Kostoglodov et al., 2003). The observed pulsing along the CSAF can be categorized as SSEs, as they are aseismic with long time duration, and occur on a broad source area (Obara et al., 2004; Rogers & Dragert, 2003). Moreover, they both occur adjacent to the locked parts of the fault that would rupture in large earthquakes. However, in subduction zones, SSEs are often accompanied by temporally and spatially correlated non-volcanic tremors. Furthermore, their source area is usually observed to be deeper than locked seismogenic areas and even below the transition zone to ductile deformation (Rogers & Dragert, 2003). Therefore, a comprehensive analysis of the seismic data is needed to verify whether these SSEs are accompanied with tremor beneath the SAF and that they correlate with the observed creep pulses.

2.4.5. Refining the CRE Scaling Relationship

As mentioned in section 2.2.3, continuous creep on a portion of a fault surrounding an asperity may repeatedly lead to sudden rupture of this asperity and generate seismic waves. Measuring the seismic moment (M_0) due to these small-scale ruptures, the amount of creep in the surrounding area during the recurrence interval preceding each event (d_i) is calculated using equation (2.6). Constants in this relationship are estimated empirically to be $\alpha_0 = -2.36$ and $\beta_0 = 0.17$ (Nadeau & Johnson, 1998). The high-resolution spatiotemporal creep model obtained in this study can be used to refine these scaling constants, which relates CREs

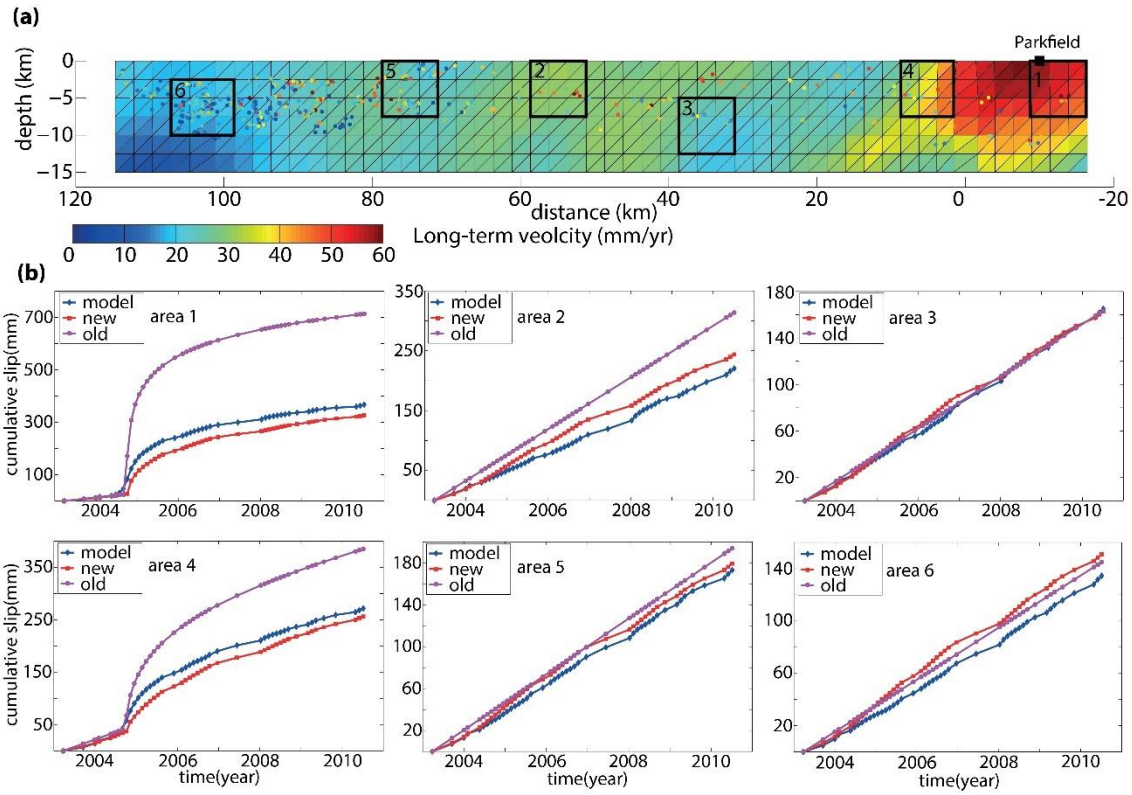

Figure 2.11. Refined scaling relationship of CRE observations. (a) Map of the long-term creep rate along the CSAF, overlaid by the CRE observations color coded based on the creep rate of the sequence. Black rectangles, numbered from 1 to 6, represent the sample area that we selected to compare the creep rate obtained from the time-dependent inversion with that obtained from the CRE sequences. (b) Time series of creep obtained using the time-dependent inversion (blue curve), compared with the CRE creep rate obtained from the original scaling relation (magenta curve) and the updated scaling relation (red curve).

moment magnitude and aseismic slip on the nearby patches. First, the time series of creep obtained through the time-dependent inversion is compared with the CRE-determined creep time series. Six zones are selected, identified by rectangles in Figure 2.11a. Next, the averaged time series of the modeled creep (blue curve) is compared with the averaged time series of CRE creep (magenta curve) within each zone. Results show that, generally, the amount of CRE is higher than the corresponding amount obtained using the optimum time-dependent model. The difference is dramatic, especially in the parts of the fault close to the Parkfield (zones 1 and 4) and the central creeping part (zone 2).

This comparison suggests, though the scaling relationship (equation (2.6)) is successful in estimating the long-term creep rates, its coefficients could be re-estimated using our time-dependent creep model. Using time series of seismic moment (M_0) for each CRE sequence and the time series of modeled creep (d_i), equation (2.6) can be rewritten as $\log(d_i) = \alpha + \beta \log(M_0)$, thus the goal is to re-estimate coefficients α and β. For each CRE sequence at each time step, d_i is obtained by averaging the creep time series over all patches located within a 5 km radius of the hypocenter. The best estimate of the coefficients is obtained using a bounded least squares optimization method. The estimated coefficients using the entire CRE sequences and their standard deviation considering various bounds for the unknowns is presented in Table 2.1.

Table 2.1. Re-estimated Coefficients of the CRE Creep Scaling Relation, Using Different Upper and Lower Bound on the Parameters During Least Squares Inversion[a]

Lower Bound	Upper Bound	Constants
α_{lb}= 0.5 α_0	α_{ub}= 1.5 α_0	α= –1.56 ± 0.31
β_{lb}= 0.5 β_0	β_{ub}= 1.5 β_0	β= 0.10 ± 0.02
α_{lb}= 0.3 α_0	α_{ub}= 1.7 α_0	α = –1.54 ± 0.34
β_{lb}= 0.3 β_0	β_{ub}= 1.7 β_0	β = 0.10 ± 0.02
α_{lb}= 0	α_{ub}= 2.0 α_0	α = –1.53 ± 0.37
β_{lb}= 0	β_{ub}= 2.0 β_0	β = 0.10 ± 0.02

[a] α_0= −2.36 and β_0= 0.17 (Nadeau & Johnson, 1998)

Repeatability of the results given different choices of upper and lower bounds indicates the robustness of the approach and accuracy of the estimated coefficients. The reported standard deviation is calculated as a representative for the dispersion of the results for different sequences distributed along the fault. The amount of creep for CRE sequences is then recalculated using the new coefficients (red curve in Figure 2.11b) and is compared with the time series of creep derived from the time-dependent model (blue curve in Figure 2.11b), as well as original CRE creep times series (magenta curve in Figure 2.11b). Evidently, except for

areas 3 and 6, there is a better agreement between the CRE creep obtained using the new coefficients and the creep obtained through the time-dependent inversion. The RMSE of the difference between the creep obtained through time-dependent modeling and the CRE creep estimated using the original and re-estimated coefficients is represented in Table 2.2. These estimates show that using new coefficients significantly decreases RMSE.

Table 2.2. Root-Mean-Square Error of the Difference Between the Time-dependent Creep Model and the CRE Creep Using the Original and Reestimated CRE Creep Scaling Coefficients

Area #	Creep Model Versus Original CRE Creep (mm/year)	Creep Model Versus Re-estimated CRE Creep (mm/year)
1	283	43.1
2	55.4	19.3
3	2.9	4.6
4	80.8	20.4
5	13.1	6.9
6	8.7	13.5

CHAPTER 3.

MULTISCALE DYNAMICS OF ASEISMIC SLIP ON CENTRAL SAN ANDREAS FAULT

The work presented in this chapter has been published as: Khoshmanesh, M., & Shirzaei, M. (2018). Multiscale Dynamics of Aseismic Slip on Central San Andreas Fault. *Geophysical Research Letters, 45*(5), 2274-2282. doi: doi:10.1002/2018GL077017

3.1. Data and Methods

In order to measure the time series of surface deformation at high spatial resolution, a wavelet-based multitemporal interferometric synthetic aperture radar (InSAR) algorithm, so-called WabInSAR (Shirzaei, 2013; Shirzaei & Bürgmann, 2013) is applied to large sets of C-band radar images. Details about the InSAR methodology is provided in section 2.1.1. The used data set includes 63 European Remote Sensing (ERS)1/2 and 30 Envisat images that are acquired in descending orbit (heading = ~192° and incidence angle = ~23°), track 27, between 3 May 1992 and 7 July 2010 with respective average temporal sampling rate of ~4.5 and ~2 months. The long-term line-of-sight (LOS) displacement rates (Figure 3.1) is validated against three-dimensional Global Positioning System (GPS) observations, projected onto the LOS direction. A standard deviation (SD) of 1.4 mm/year is found for the difference between these data sets. The comparison between the two data sets along profiles perpendicular to the strand of CSAF (Figure 3.1) also show a good agreement (Figure 3.2). To further validate both the long-term and short-term behaviors, the cumulative LOS creep time series is compared with the creep measured by the Slacks Canyon creepmeter station projected onto the LOS direction (Figure 3.3). The comparison shows an overall good agreement with SD of 4.5 mm for the

differences over the ~18 years observation period. The SD for the period following year 2003 is 1.2 mm, while the corresponding value for the prior period is 5.8 mm. The improved SD for the latter period is likely due to addition of high-quality imageries provided by Envisat satellite.

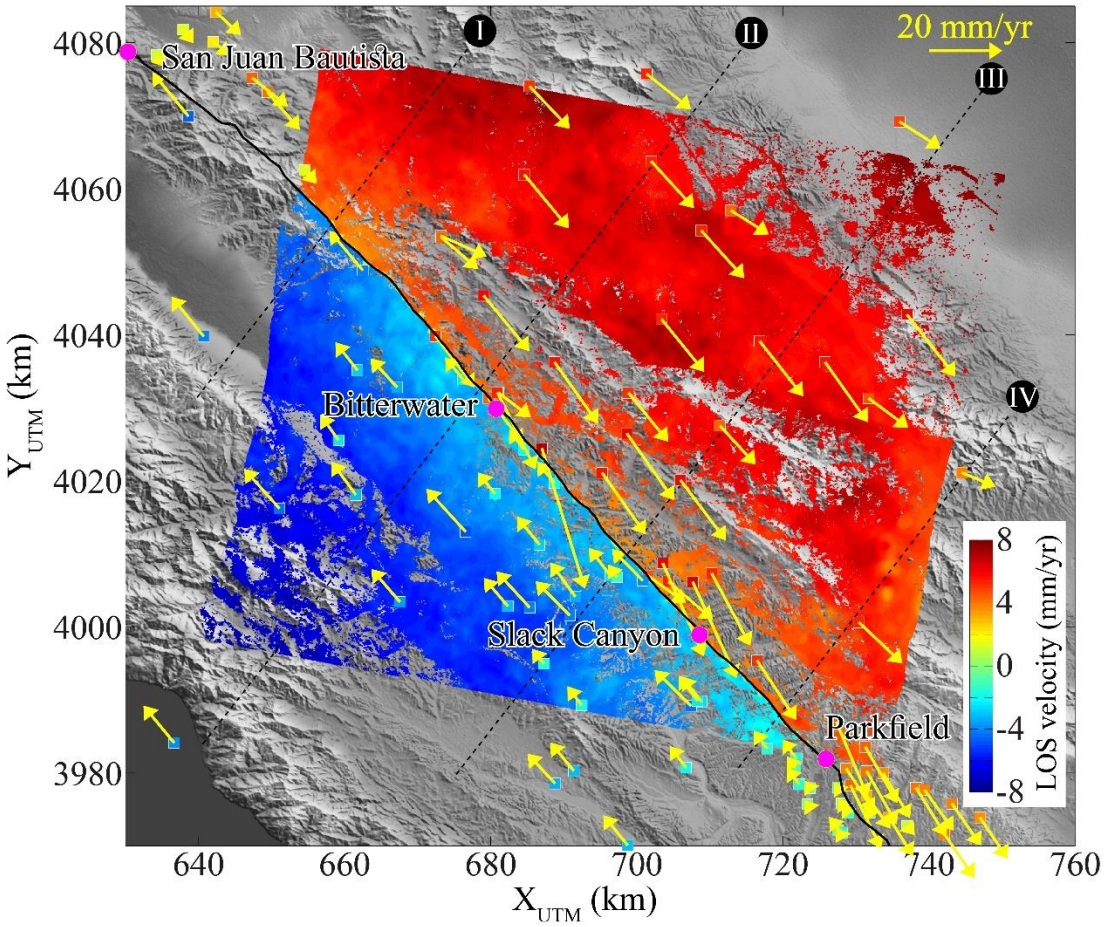

Figure 3.1. InSAR LOS surface deformation between 1992 and 2010. The red and blue colors represent the surface motion in the LOS direction toward and away from the satellite, respectively. The solid black line represents the surface trace of the SAF. The GPS stations are shown using the solid rectangles color-coded based on their three-dimensional displacement rates projected onto the LOS direction. The direction and magnitude of GPS horizontal rates are also shown using the yellow arrows. The black dashed lines show the location of fault-perpendicular profiles, where the InSAR LOS rates are compared with the corresponding GPS values (Figure 3.2).

To solve for spatiotemporal evolution of fault slip, a time-dependent kinematic modeling approach is implemented (Khoshmanesh et al., 2015), as described in section 2.1.2.

This approach integrates a static slip inversion scheme with a recursive Kalman filter structure (Shirzaei & Walter, 2010), which allows incorporating various data sets and constraints such as repeating earthquakes. The effect of deep dislocations is removed by considering a long-term slip rate of 34.5 mm/year (Rolandone et al., 2008) on a vertical planar fault extending

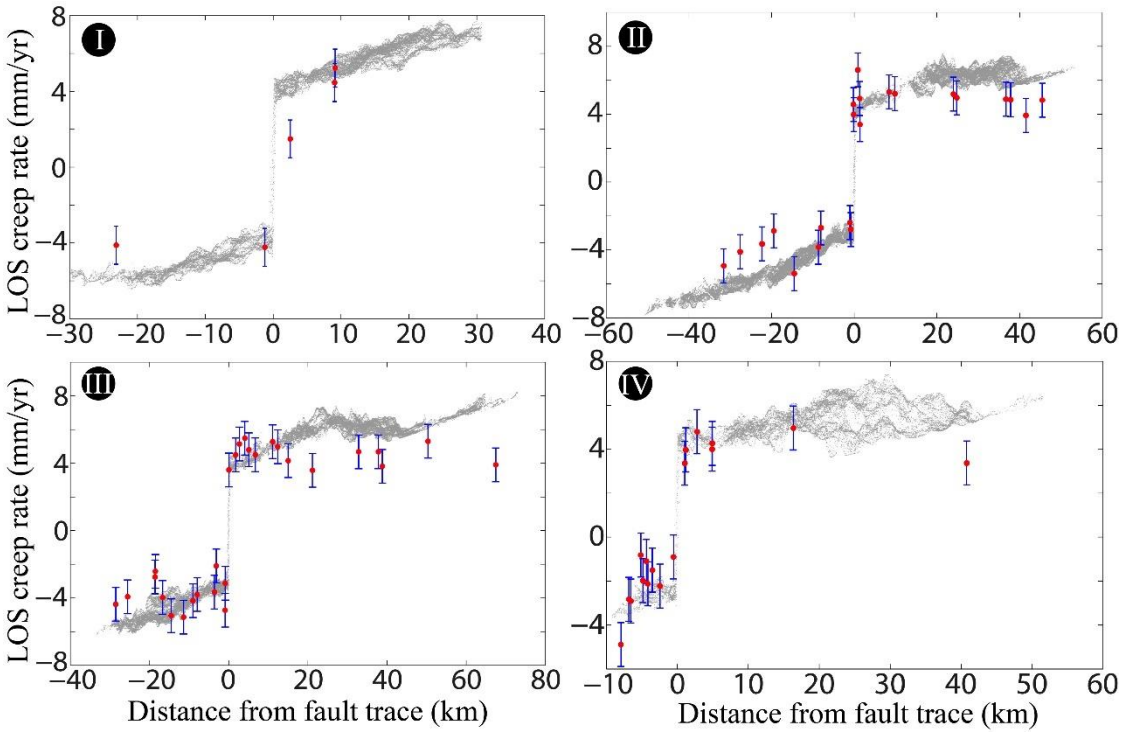

Figure 3.2. Validation of long-term InSAR observation with GPS data set. InSAR LOS long-term surface velocities (gray dots) within ~10 km distance of either side of the fault-perpendicular profiles numbered from I to IV, whose locations are shown using the dashed black line in Figure 3.1. The red dots represent the corresponding amount of three-dimensional surface deformation rate measured by the GPS stations, when projected onto the LOS direction. The blue-colored error bars show 1 mm/year uncertainty for GPS observations.

from 25 km downward. The segment between 15 and 25 km depth is considered as transition zone between shallow seismogenic creep and deep ductile slip. The top 25 km of the fault is then discretized into triangles of ~2.5 km side. For practical purposes, the surface observations is down-sampled using a method similar to the Quadtree algorithm (Jónsson et al., 2002), but adapted for irregularly sampled data (Khoshmanesh et al., 2015). The data down-sampled

through this method represents the statistically significant portion of the observation; thus, does not contribute to the uncertainty of inversion results (Jónsson et al., 2002). To mitigate the model roughness, the second derivative of the creep on the fault (Segall & Harris, 1987)

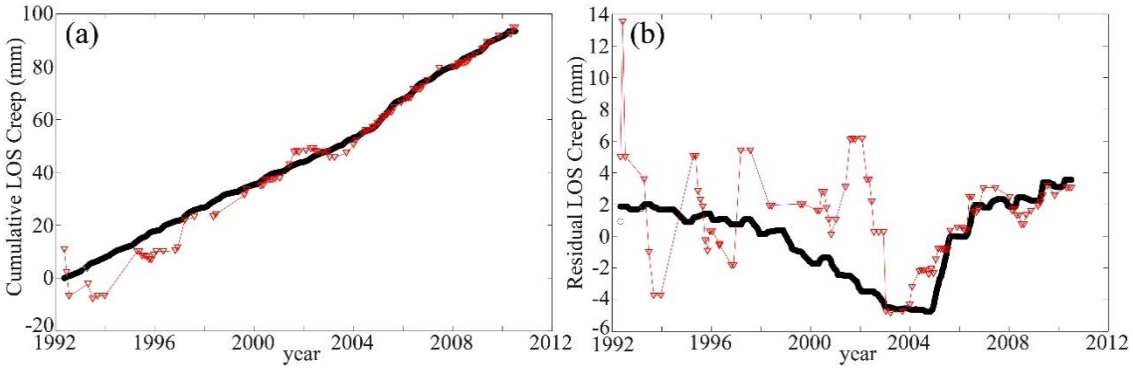

Figure 3.3. Validation of InSAR time series with creepmeter data set. Comparison between cumulative (a) and detrended (b) time series of InSAR surface creep and the corresponding creep measured by creepmeter located at Slacks Canyon stations, when projected onto the radar LOS.

is minimized. The trade-off parameter, controlling the model roughness, is determined using an L-curve approach (Figure 3.4) (Jónsson et al., 2002).

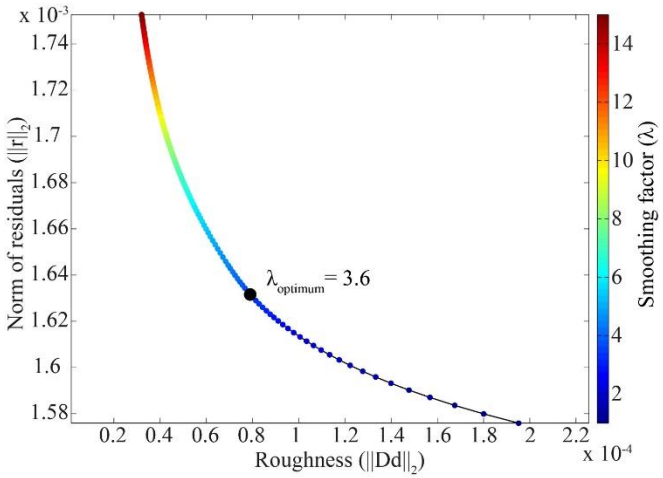

Figure 3.4. The trade-off curve between roughness of the creep model and its fit to the surface deformation data, which is used to estimate the optimum smoothing factor. To estimate the smoothing factor, the cumulative InSAR surface deformation as a difference between deformation at the last and first time steps is used, and the same value is applied throughout the time-dependent inversion.

The other data set used here includes the time series of fault creep obtained from characteristically repeating earthquakes (CREs), previously published by Turner et al. (2015). As explained in section 2.2.3, CREs are sequence of microseismic events with highly similar waveforms and magnitudes, which are resulted from semi-periodic failure of the same asperity loaded by creep on its adjacent fault segment (Nadeau et al., 1995; Nadeau & Johnson, 1998). For each CRE sequence during 1992 - 2010 (Figure 3.5a), a function composed of a linear

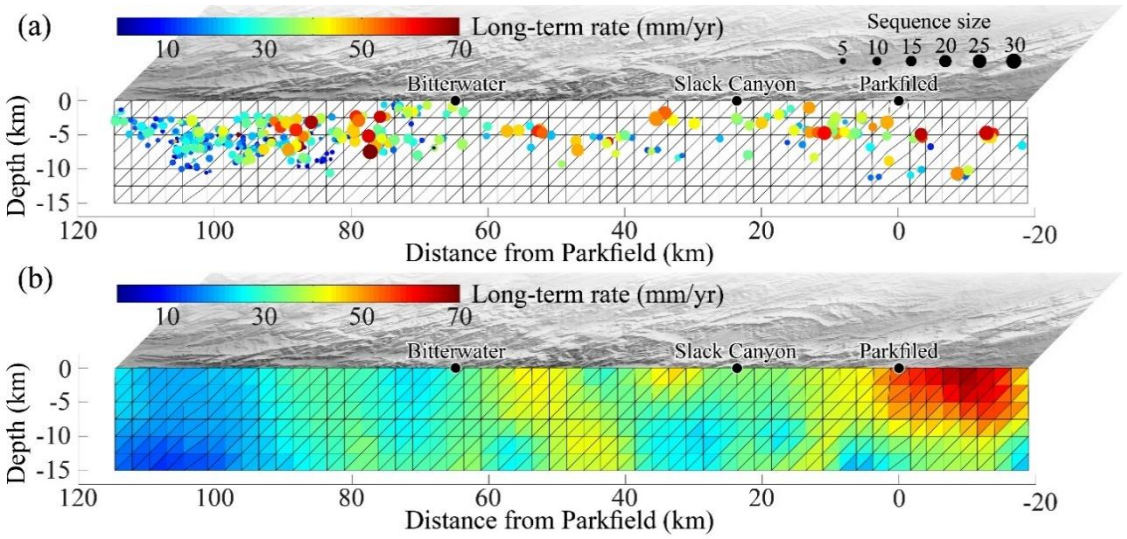

Figure 3.5. Characteristically repeating earthquake observation. (a) Spatial distribution of CRE sequences, color-coded based on their long-term rate. Size of circle at each CRE hypocenter corresponds to the size of the sequence during 1992 - 2010. (b) Map of the long-term creep rate obtained by spatial oversampling of creep associated with CRE sequences.

trend, and a logarithmic component that accounts for the afterslip of 2004 Parkfield earthquake, is fitted to obtain the time series of CRE creep at the time of SAR acquisitions. Following the temporal interpolation, a spatial oversampling scheme is implemented to estimate the time series of CRE creep for each triangular patch. The amount of creep on each patch is estimated as the weighted average of creep associated with CREs located within 5 km from its center (Figure 3.5b). The number of events in each CRE sequence (Figure 3.5a) is used to determine the weight of the associated sequence for this averaging. The oversampled

time series of CRE creep is then used to inform the static creep inversion step by constraining the incremental creep between successive time steps to be less than 190% the equivalent CRE creep. This choice of upper bound, while restricting the maximum average creep rate to remain below the slip rate of deep dislocation zone, does not determine its temporal evolution.

3.2. Results and Discussion

3.2.1. Eighteen-Year Time-Dependent Creep Model

Distribution of long-term creep rate, estimated as the slope of the best fitting line to the time series for the period 1992 - 2010, shows a higher rate in the central zone (CZ) from km 15 to 90, which gradually declines moving toward the two termini of the fault model

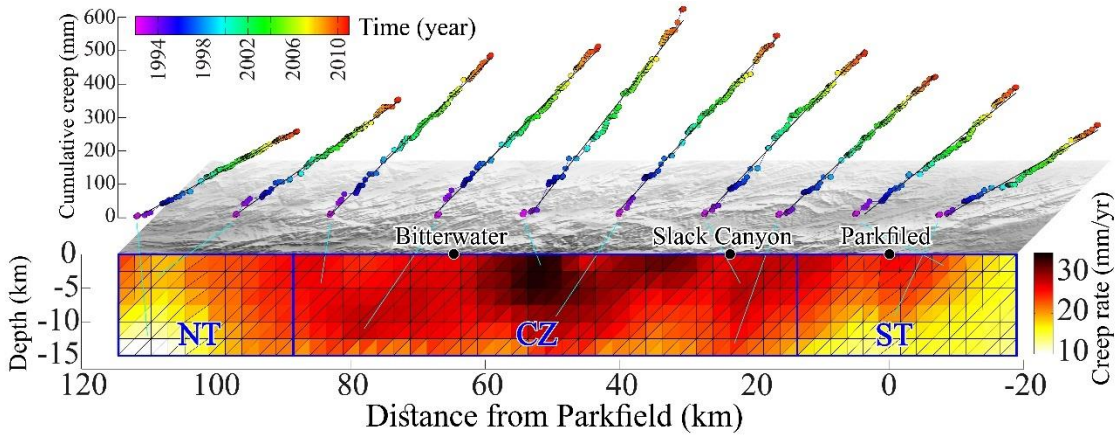

Figure 3.6. The distribution of inverted long-term creep rate on central San Andreas Fault. The cumulative time series of creep for several patches is also shown, color-coded based on the SAR acquisition times. The best fit to each time series, determining the long-term rate, is also shown using the solid black line.

(Figure 3.6), consistent with earlier studies (e.g., Jolivet et al., 2015b; Khoshmanesh et al., 2015; Rolandone et al., 2008). Using a bootstrapping approach (Murray & Segall, 2002), the estimated uncertainty of long-term creep rate resulted from adding random and colored noise (Hanssen, 2001) with 5 mm SD to the time series of InSAR observations (Appendix B) is up to 1.5 and 4 mm/year, respectively (Figure 3.7 and Figure 3.8). Also, the model misfit, that is,

observed long-term surface LOS rate less predicted one (Figure 3.9), yields an SD of 0.8 mm/year.

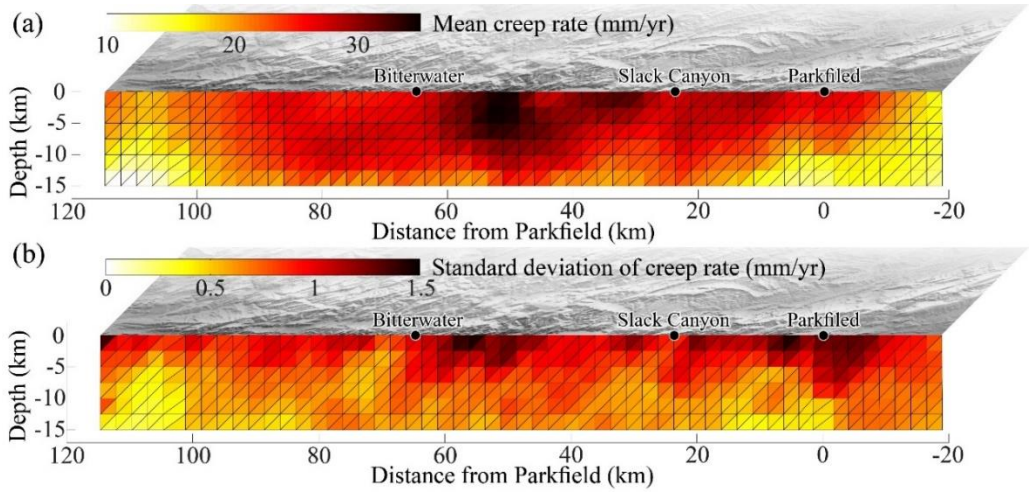

Figure 3.7. Uncertainty of modeled creep due to a random noise with standard deviation of 5 mm in time series of surface deformation. (a) Mean long-term rate, and (b) Standard deviation of long-term rate.

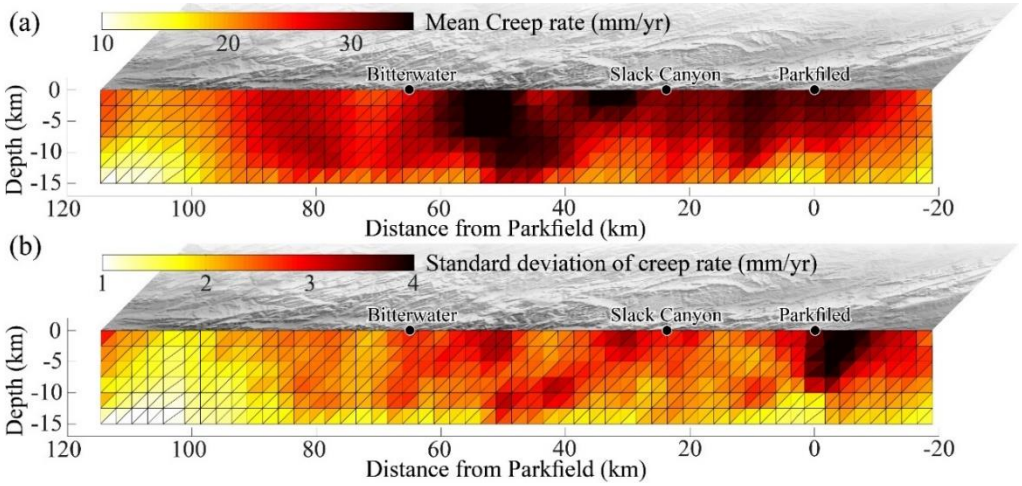

Figure 3.8. Uncertainty of modeled creep due to a spatially correlated colored noise with standard deviation of 5 mm in time series of surface deformation. (a) Mean long-term rate, and (b) Standard deviation of long-term rate.

Two zones of significant creep rate decline are identified on the deeper portion of the northern transition (NT) zone between km 90 and 115, and southern transition (ST) zone at km −20 - 15 (Figure 3.6). The average coupling coefficient at both NT and ST zone, assuming

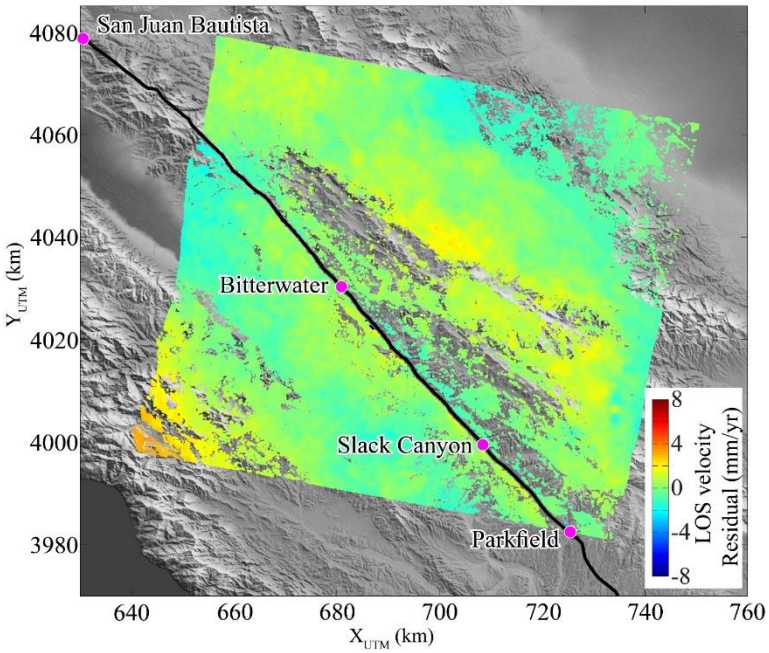

Figure 3.9. Residuals (observed-modeled) associated with the optimum creep model obtained from inverting the LOS long-term deformation velocities.

a long-term rate of 34.5 mm/year, ranges from 0.35 in shallow parts to 0.55 near the bottom of seismogenic zone (Figure 3.10). The higher coupling of these two zones compared to CZ,

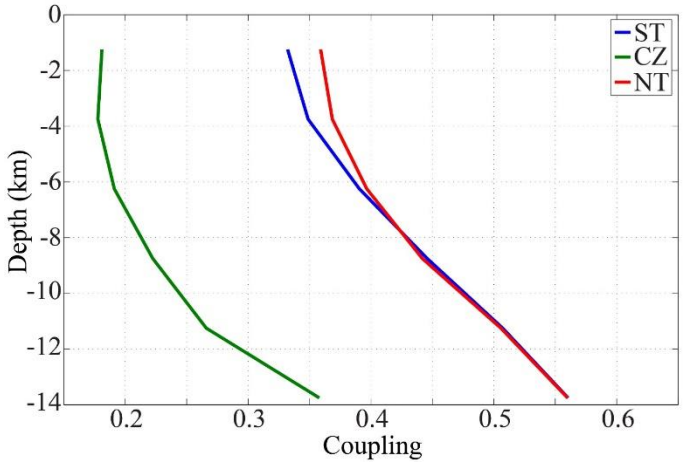

Figure 3.10. Along-strike averaged coupling coefficient as a function of depth for central zone (CZ: km 15 - 90) in green, northern transition zone (NT: km 90 - 115) in red, and southern transition zone (ST: km −20 - 15) in blue.

where coupling coefficient is between 0.18 and 0.35, may be a result of stress shadowing effect of the surrounding locked segments (Johnson, 2013). Assuming a shear modulus of 30 GPa,

the accumulated long-term strain along the CSAF is equivalent to a M_w 5.8 earthquake per year. This estimate falls into the M_w 5.7 - 5.9 range reported by Ryder and Bürgmann (2008) for 1992 - 2001, but is slightly higher than the M_w 5.6 - 5.7 range calculated by Khoshmanesh et al. (2015) for 2003 - 2011, likely due to the influence of Parkfield earthquake afterslip in the latter model.

The short-term (<2 years period) creep rate variations on the CSAF are constrained in CHAPTER 2 (section 2.4.4), indicating its complex behavior (e.g., Khoshmanesh et al., 2015; Nadeau & McEvilly, 2004). To obtain a first-order approximation of the CSAF intermediate-term (decadal-scale) creeping behavior, the time series of cumulative creep (d) on each patch is further modeled using an equation comprising an initial rate (v_0), different from long-term rate shown in Figure 3.6, and a constant acceleration (a) (Mavrommatis et al., 2015):

$$d(t) = v_0(t - t_0) + \frac{1}{2}a(t - t_0)^2 \tag{3.1}$$

The constant acceleration is estimated using a least squares approach (Figure 3.11a). The associated uncertainty of model acceleration is also estimated using bootstrapping by introducing a random noise with SD equal to 5% of the total creep to the time series of creep at each patch (Figure 3.12). Considering that this choice of SD is an upper bound for the estimated creep uncertainty due to residual noise in InSAR observations (Figure 3.8), the pattern of acceleration remains persistent within the range of model uncertainty. The results for ST zone (km −20 - 15), which is estimated only for the period prior to the Parkfield earthquake to avoid the impact of afterslip, suggest that this segment has been accelerating in years prior to the earthquake. Such intriguing observations are also made for northeast Japan subduction zone prior to the 2011 Tohoku earthquake (Mavrommatis et al., 2015). This

accelerating segment is limited by a zone of deceleration at ~ −0.7 mm/year^2, located at km 0 - 10. The shallow part (< 7.5 km depth) of the middle segment (km 40 to ~90) is characterized by accelerated creep of up to 2 mm/year^2. We further identify several zones of creep deceleration at km 20 - 60 and km 80 - 110. The pattern and amplitude of the deceleration in these zones vary with depth. The major shallow creep deceleration zone is located at km 90 - 110 with value of −1 mm/year^2. The major deep deceleration zone (km 35 - 60) with creep deceleration of ~ −0.5 mm/year^2, has an overlap with the locked patch suggested by some workers being capable of rupturing in a M_w 6.5 earthquake (Maurer & Johnson, 2014).

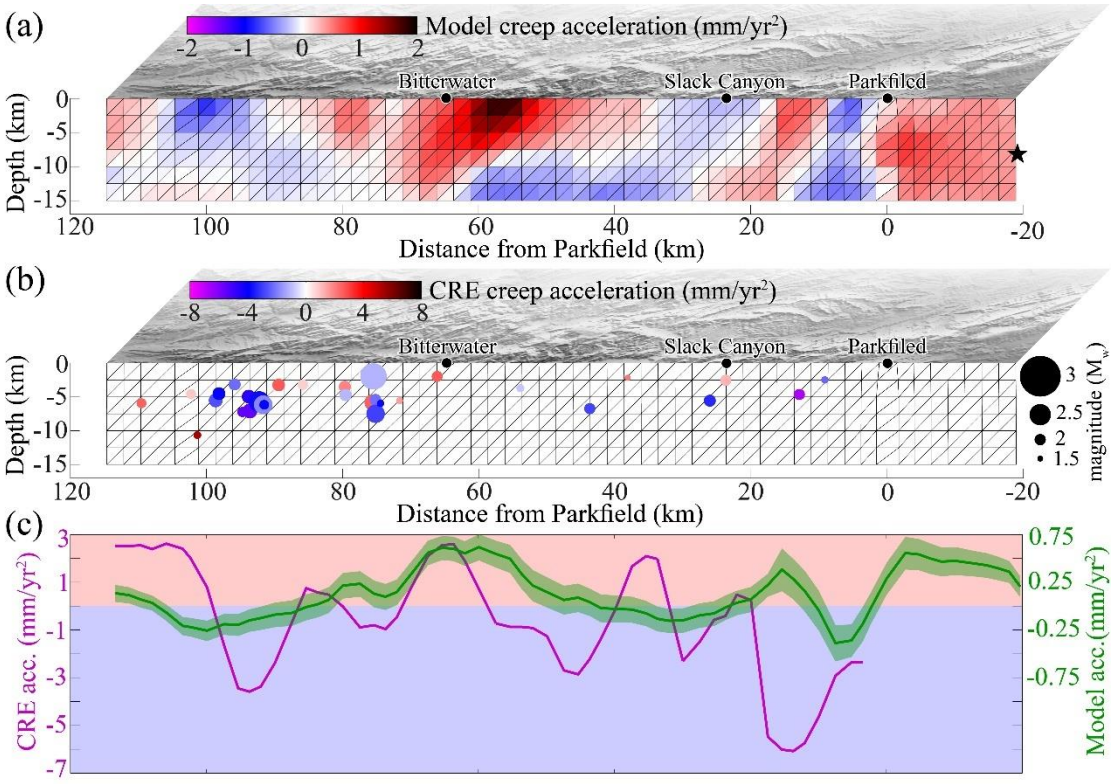

Figure 3.11. Spatial distribution of constant acceleration estimated by fitting equation (2.2) to (a) the time series of creep at each fault patch. The black star shows the hypocenter of 2004 M_w 6 Parkfield earthquake. (b) Spatial distribution of CRE sequences passing the Mann-Kendall test with 95% confidence, color-coded based on the estimated constant acceleration for each sequence. (c) Along-strike comparison between depth-averaged constant accelerations estimated from kinematic model (green curve) and CRE creeps (purple). The green shaded area represents the associated uncertainty of model acceleration (Figure 3.12).

The equation (2.2) is further applied to the cumulative CRE creep to estimate the associated constant acceleration. To obtain a reliable result, only the sequences that pass Mann-Kendall (MK) statistical test at 95% confidence level (Appendix C), indicating that they are characterized by a monotonic creep trend (Gilbert, 1987; Satriano et al., 2014) are considered. For the sequences affected by the Parkfield earthquake afterslip, only the events prior to the earthquake are considered. The 33 sequences passing the criteria (Figure 3.11b) are oversampled on the fault triangular mesh using the weighted averaging approach explained above (Figure C.1 in Appendix C). Since most of CREs are within 2.5 - 7.5 km depth, no obvious depth-dependent pattern is evident in the CRE accelerations. Some extreme acceleration values (up to 4 times of that estimated for kinematic creep model) are likely artifact

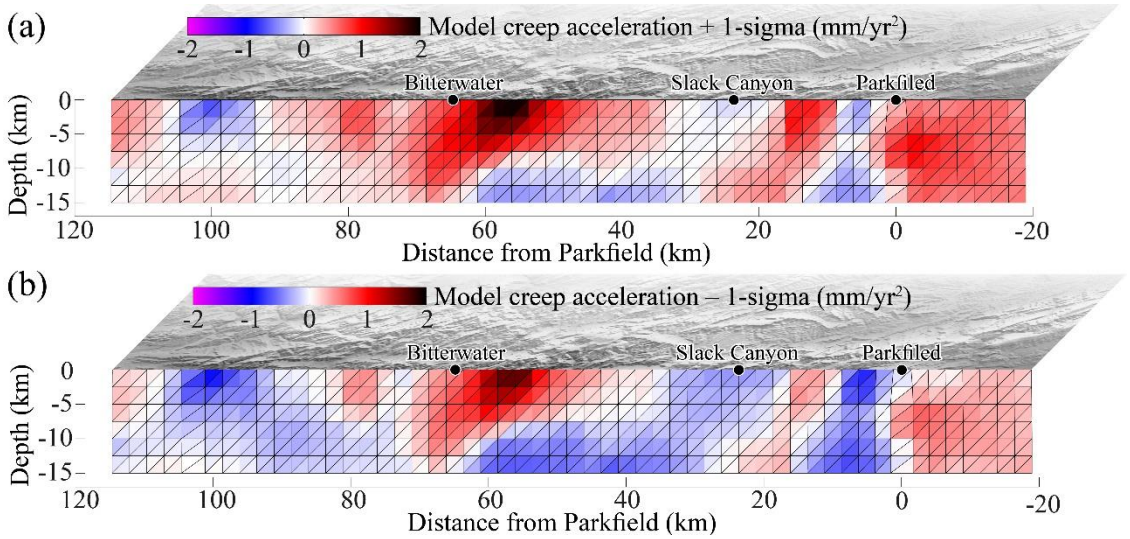

Figure 3.12. Uncertainty of modeled creep acceleration, quantified using 200 samples of fault creep times series generated by introducing a random noise with standard deviation equal to 5% of total creep during 1992 - 2010. The figures show mean acceleration plus (a) and minus (b) one-sigma standard deviation.

caused by the small number of events in that particular sequence and/or the large uncertainty associated with CRE creep (Nadeau & McEvilly, 2004). Nonetheless, the stress interaction between CRE sequences as well as the stress perturbations due to microseismicity on the CSAF may further complicate the observed pattern of CRE acceleration (Mavrommatis et al.,

2015). Comparing the estimated creep accelerations from kinematic model (Figure 3.11a) and CREs (Figure 3.11b) indicates similar features distributed along strike of the fault. The model and CRE acceleration estimates are further compared by averaging the results along the dip (Figure 3.11c). Some discrepancies between the two estimates can be found, in particular at km ~15 and ~35, likely due to the lack of depth resolution and sparse sampling of CRE sequences in those locations (Figure 3.11b). However, the correlation coefficient is 65 ± 17% for the segment between km 40 and 100 where most of the CRE sequences are located, and the estimated CRE creep acceleration has a lower uncertainty. These observations mark a new class of creep rate variations on the CSAF that occur on decadal scale. As a result, stress is relieved on the zones of creep acceleration, while they load adjacent patches, including those characterized with creep deceleration that further accumulate strain over time due to lowered creep rate.

Considering a steady state rate- and state-dependent friction law (Ruina, 1983) and constant shear stress, change in the rate of slip is inversely proportional to the variations of effective normal stress (Dupont & Bapna, 1994). On the CSAF, effective stress is low and possibly heterogeneous due to presence of high pressure fluid (Faulkner et al., 2006; Rice, 1992). Thus, the zones of accelerated and decelerated creep may mark areas subject to decadal increase or decrease in pore fluid pressure, which are separated by low permeability barriers (Lockner & Byerlee, 1995). Change in effective stress, that is, pore fluid pressure, also alters the critical stiffness (Rubin & Ampuero, 2005). Thus, for slow enough changes in the rate of creep such as those observed here, under which the state variable remains steady, the zones of creep acceleration are also subject to decrease in critical stiffness, promoting stable slip. Whereas, critical stiffness increases over the zone of deceleration. However, this does not necessarily mean that creeping segment is capable of generating its own large earthquakes

(Carpenter et al., 2011; Lockner et al., 2011). Nonetheless, the accumulated strain over the zones of creep deceleration may release once a fast enough rupture initiated on the surrounding locked zone propagates through the creeping section, as a result of thermal pressurization (Noda & Lapusta, 2013).

3.2.2. Dynamics of Creep

A statistical approach is further employed to explore the observations of short-term (< 2 years period) creep rate changes on the CSAF (Figure 3.6) and infer the underlying mechanisms. The temporal evolution of short-term creep rate is estimated from surface InSAR LOS data, estimated between successive acquisitions, using a moving window of size 0.5 km × 2.5 km (from 0.3 km to 2.8 km fault-perpendicular) and step size of 0.3 km along the strike. To account for the spatially sparse and irregular sampling of InSAR measurements, which results in different number of pixels in the moving window, the uncertainty of the measured short-term creep rates is further estimate in terms of formal standard deviation. Assuming 5 mm SD for LOS deformation measured at each InSAR pixel (Shirzaei, 2013) and given the number of pixels in each moving window, a one-sigma uncertainty range of 0.1 - 1.3 mm/year is estimated.

The spatiotemporal distribution of near-field creep rate (Figure 3.13a), reveals complex short-term behavior of aseismic slip along the CSAF. This observation suggests that evolution of aseismic slip includes periods of slow creep, that is, below the long-term average (blue color in Figure 3.13a), followed by episodes of fast creep, where the creep rate exceeds the long-term average (warmer colors). These two opposing regimes are respectively referred to as "pinning" and "depinning," borrowed from the disciplines studying dynamic critical phenomena, such as fluid invasion in disordered medium and crack propagation (e.g., Clotet

et al., 2016; Maloy et al., 2006; Planet et al., 2009; Tallakstad et al., 2011). The empirical probability distribution function (PDF) of the near-field short-term creep rates is then estimated. The creep rates obtained from only ERS (1992 - 2001) and combined ERS and Envisat (2003 - 2010) satellites are separately normalized with their associated long-term rate to account for the possible differences between the products of different sensors. The result show that creep rate PDF does not follow a Gaussian distribution (Figure 3.13b). Notably, the

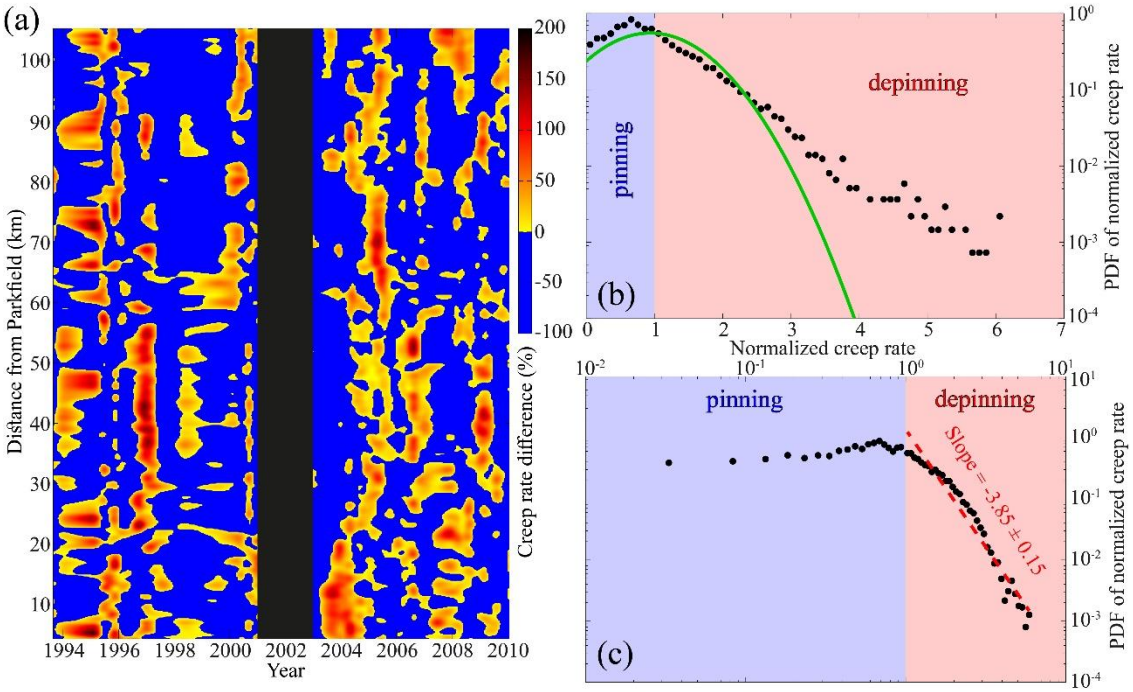

Figure 3.13. Near-field creep rate variation and its statistical properties. (a) Spatiotemporal distribution of creep rate less mean velocity in percentage. The slow creeping episodes during pinning regime are shown with blue color to highlight the creep avalanches shown with warmer colors. The shaded black area shows the time interval 2001 - 2003 excluded from analysis due to the degraded quality of ERS observation resulted from complete failure of satellite's gyroscope. A Gaussian smoothing filter with window size of ~8 months and ~1.3 km in time and space domains, respectively, is applied to the figure. (b) Probability distribution function (PDF) of short-term creep rate, normalized by the mean rate. Shown in green curve is the normal distribution with mean of one and SD equal to that of normalized creep rate (0.72). The blue and red shaded area represent the pinning and depinning regime, respectively. (c) The PDF of normalized short-term creep rate in log-log space. The dashed red line shows the power law with exponent 3.85 fitted to the normalized velocity in the depinning regime.

maximum PDF does not coincide with the long-term rate, which suggests that creep is mostly expected to occur in the pinning regime, while some creep values exceeding the long-term rate occur during the subsequent depinning period. The PDF also has a longer tail toward the extreme positive values, up to ~6 times the average long-term rate, with an estimated skewness of 1.6. The distribution of depinning rates can be well approximated by a power law function $P(v_n) \propto (v_n)^{-\alpha}$, where $v_n = v/\bar{v} > 1$, $\bar{v}$ is the long-term rate, and α = 3.85 ± 0.15 (Figure 3.13c). Propagating the one-sigma uncertainty estimated for the short-term creep rates, the exponent α ranges between 3.60 and 4.12 (Figure D.1 in Appendix D).

That the maximum PDF appears below the long-term rate (Figure 3.13b) and the depinning rates exhibit a power law behavior (Figure 3.13c) mark a specific class of creep behavior, referred to as "creep avalanches" (e.g., Clotet et al., 2016; Maloy et al., 2006; Tallakstad et al., 2011). These attributes are also reported to characterize the statistical properties of the instantaneous velocities associated with crack propagation and fluid imbibition in porous medium (e.g., Clotet et al., 2016; Tallakstad et al., 2011). In our observations, the dynamics of aseismic slip in depinning regime is governed by creep avalanches, which appear as spatially isolated clusters of velocities exceeding the long-term average rate (Figure 3.13a).

The characteristics of the creep avalanches is further explored by estimating their size (S), defined as average excess rate, and length (L) as the along-strike extent of the clusters. To make a comparison between the observed creep avalanches and the more established statistical properties for the seismic events, such as Gutenberg-Richter law (Gutenberg & Richter, 1944), the potency rate is estimated as $P = SL^2$, assuming that the extent of avalanche along the dip is equal to its along-strike length. The PDF of potency rate (Figure 3.14a) can be explained by a power law relation with an exponent of α = 1 (black dashed line in Figure 3.14a), as a first-

order approximation, similar to that reported for the observed creep avalanches along the creeping section of the Haiyuan Fault (Jolivet et al., 2015a). However, a double power law with exponent $\alpha_1 = 0.66$ for $P < P_0$ and $\alpha_1 = 1.38$ for $P > P_0$, where $P_0 = 1.3 \times 10^4$ m^3/year (red dashed line in Figure 3.14a), can better explain the PDF of potency rate. Considering the effect of short-term creep rate uncertainties on the potency rate estimates (Figure D.2), the estimated exponents remain similar given the range of errors. The increase in the estimated exponent for $P > P_0$ suggests a cutoff in the probability of the creep avalanches with higher potency rates. To identify the cause of this decline, the PDF of avalanche size and length are separately

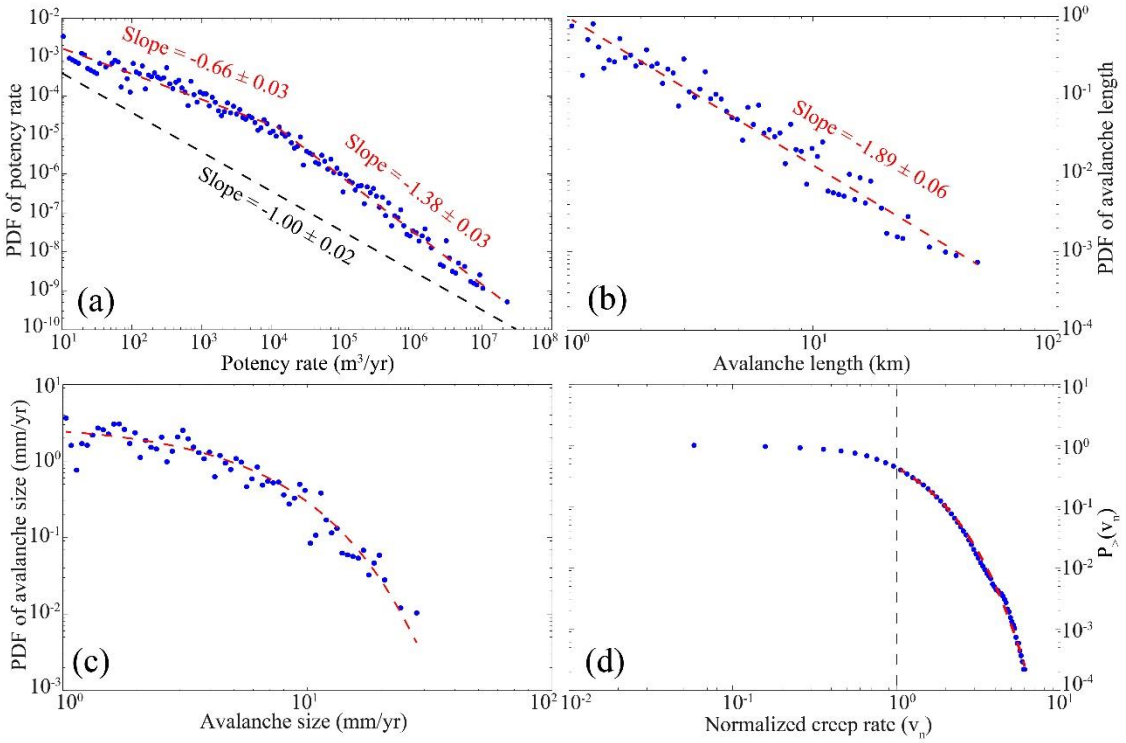

Figure 3.14. Probability distribution function (PDF) of potency and its constituting parameters. (a) PDF of the potency rate. The dashed black and red line respectively show the single and double power law functions fitted to the PDF. (b) PDF of avalanche length with fitted power law shown using the dashed red line. (c) PDF of avalanche size with fitted exponential function shown using the dashed red line. (d) Cumulative distribution function (CDF) of short-term creep rate with exponential function (dashed red line) fitted to the rates higher than long-term average (vertical dashed black line).

investigated. The results show that distribution of avalanche length (Figure 3.14b) has a power law form with an exponent of $\alpha = 1.89$, suggesting that avalanches occur at all length scales. The PDF of avalanche size (Figure 3.14c), however, is well approximated by an exponential function in the form of $P(S) \propto exp(-S/\beta)$, with $\beta = 0.42$. Therefore, the decline in the slope of potency rate probabilities at higher rates is resulted from the exponential decay in the PDF of avalanche size. One possible cause of this decay is the sparse and irregular temporal sampling of InSAR dataset, which restricts us to estimate of creep rate averaged over several months. The decline with respect to the power law for the higher rates, though less pronounced, is also evident in the PDF of normalized velocities (Figure 3.13c). To further highlight this probability decay, the cumulative probability distribution (CDF) of short-term creep rates is estimated. The result show that CDF of creep rate can be explained by an exponential decay in the form $P_{>}(v_n) \propto exp(-v_n/\beta)$, where $P_{>}(v_n)$ quantifies the probability of velocity fluctuations larger than v_n, and $\beta = 0.68$ for $v_n > 1$ (Figure 3.14d). This exponential decay in the probability of higher velocities is linked to the presence of fluids on the crack tips, leading to subcritical growth, following the laboratory experiments performed on crack propagation (Marchenko et al., 2006). This is also consistent with the suggested role of elevated pore fluid pressure as the responsible mechanism for transient creep events (Liu & Rice, 2007; Rice, 1992).

CHAPTER 4.

EPISODIC CREEP EVENTS ON THE SAN ANDREAS FAULT CAUSED BY PORE PRESSURE VARIATIONS

The work presented in this chapter has been published as: Khoshmanesh, M., & Shirzaei, M. (2018). Episodic creep events on the San Andreas Fault caused by pore pressure variations. *Nature Geoscience, 11*(8), 610-614. doi: 10.1038/s41561-018-0160-2

4.1. Slow Slip Events on the Central San Andreas Fault

The time series of line-of-sight (LOS) surface deformation obtained from interferometric processing of synthetic aperture radar (SAR) data set, collected between 26 March 2003 and 7 July 2010 with average temporal sampling interval of ~2 months, are used to measure surface fault creep (Figure 4.1). The data set is obtained by applying an advanced multitemporal InSAR processing algorithm (Shirzaei, 2013), explained in section 2.1.1, on 16 and 30 images acquired by European Remote Sensing (ERS) and Envisat C-band satellites, respectively (Khoshmanesh et al., 2015; Turner et al., 2015). These LOS observations are thoroughly validated using independent geodetic observations in section 2.2.1 (see also, Turner et al. (2015)). Here, the near-field LOS creep time series is calculated using a moving window of 0.5 km × 2.7 km (from 0.3 km to 3 km fault-normal distance) and along-strike step size of 0.3 km (inset in Figure 4.1) (Khoshmanesh & Shirzaei, 2018b). The observations of near-field LOS creep reflect the slip behavior of the shallow few kilometer portion of the fault, which might have a similar pattern to that of deeper seismogenic depths (Jolivet et al., 2015a; Khoshmanesh et al., 2015). The spatiotemporal distribution of the difference between short-term and long-term LOS creep rate along the CSAF depicts the local variations of creep rate

in both space and time (Figure 4.2). To increase the signal to noise ratio, the rate differences is averaged in the spatial domain (magenta curve in Figure 4.3a), which reveals the semi-periodic slow slip events (SSE). To focus on the interseismic slip and disregarding the co- and post-seismic deformations due to the 2004 Parkfield earthquake in our analysis, the affected observations are excluded (inside the black dashed rectangle in Figure 4.2).

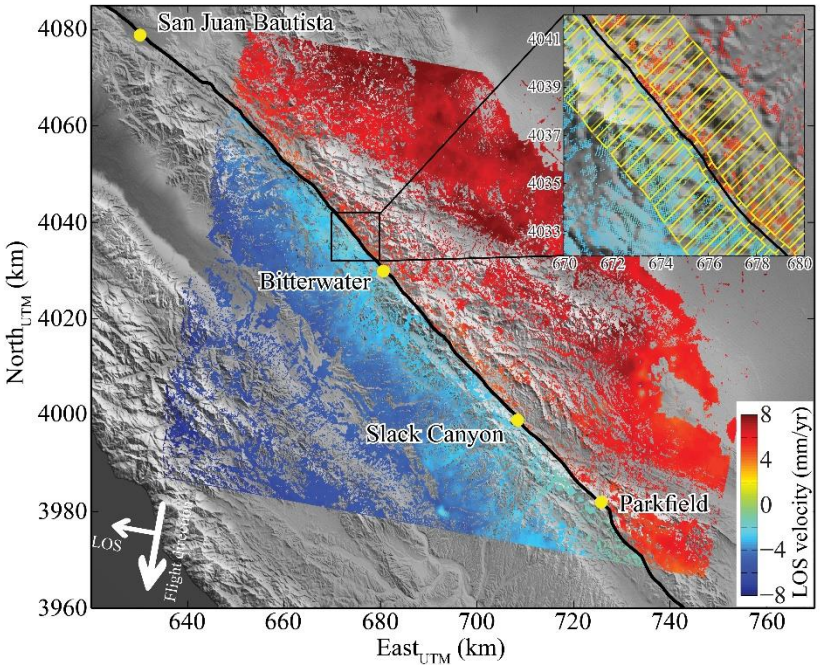

Figure 4.1. Creeping segment of the San Andreas Fault with long-term InSAR LOS velocity (Khoshmanesh et al., 2015; Turner et al., 2015). The trace of the SAF is shown with the black line. Warm and cold colors correspond, respectively, to the movement toward and away from the descending satellite. The inset depicts the moving window (yellow boxes) used for estimation of near-field creep rate, with every other step shown with a lower opacity for visualization purposes. Shaded relief topography is digital terrain model from the Shuttle Radar Topography Mission.

4.1.1. Fault Creep Self-Affinity Analysis

The roughness of LOS creep distribution along the fault is estimated through self-affinity analysis implemented on the fault-parallel profiles of rate difference at each time step. A self-affine two-dimensional profile in xy plane has constant statistical properties under an

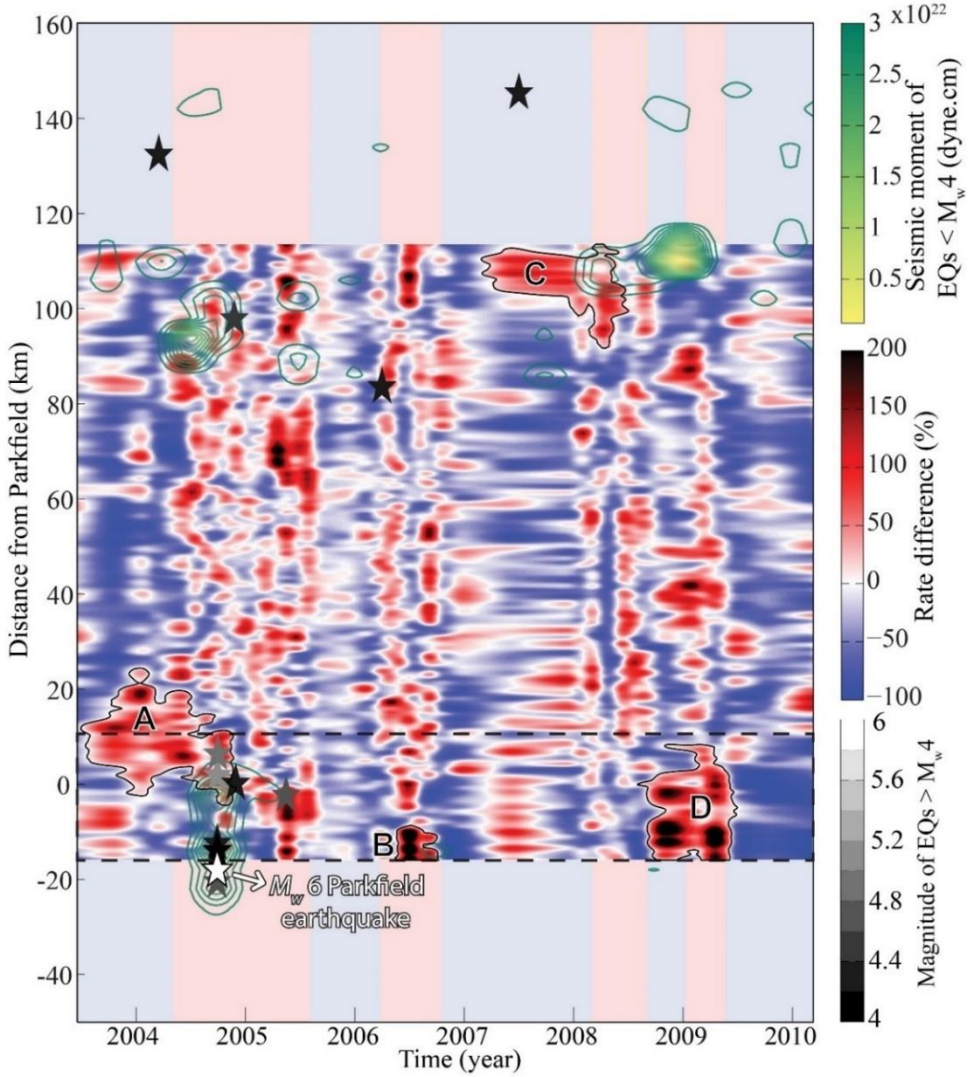

Figure 4.2. Spatiotemporal distribution of rate difference and seismicity. The relative difference between short-term (between consecutive time steps) and long-term LOS creep rate (slope of the cumulative time series) in percentage, along with moment released for earthquakes < M_w 4 (green contours). The grayscale stars show the location and time of the earthquakes > M_w 4. The light red and blue bands on the neighboring segments highlight the time intervals of SSEs and the decelerated creeping, respectively. The dashed rectangle shows the approximate location of the Parkfield transition zone which is excluded from our analyses. The areas indicated by capital letters show the extent of the significant local bursts that are discussed in the main text.

affine transformation of the form $\delta x \rightarrow \lambda \delta x,\ \delta y \rightarrow \lambda^H \delta y$, where λ is the scale factor and H is the Hurst exponent (Schmittbuhl et al., 1995a). To investigate the self-affinity of a given profile, the method of Fourier analysis is widely used (Schmittbuhl et al., 1995b). Through this method, Fourier power spectrum (P) as a function of wave number (k) follows a linear trend

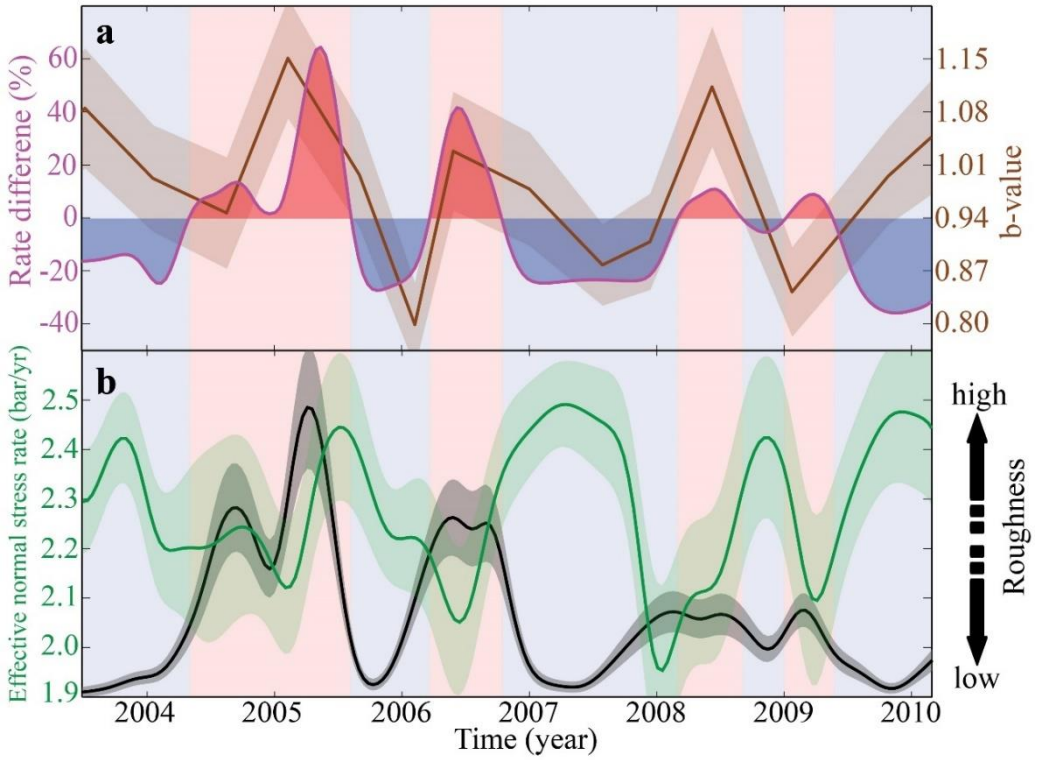

Figure 4.3. temporal evolution of creep rate, effective normal stressing rate, roughness and b-value. (a) Time series of spatially averaged LOS creep rate difference in percentage (magenta), and *b*-value (brown) alongside its one-sigma uncertainty (shaded brown). Background red and blue bands highlight the time interval of SSEs and decelerated creeping, respectively. (b) Temporal evolution of spatially averaged effective normal stress rate (green) and its standard deviation (shaded green), and roughness amplitude of LOS creep rate difference along the fault (black) and its one-sigma uncertainty (shaded gray). All the curves in this figure, beside the *b*-value are smoothed using a Gaussian smoothing filter with a window size of 6 months.

in log-log space, which is related to the Hurst exponent through $P(k) = Ck^{-1-2H}$, where C is the pre-factor. Thus, fitting a line to the log-log plot of $P(k)$ versus wave number k using a robust regression method, enables estimating the Hurst exponent and pre-factor, as well as their standard deviations. The Hurst exponent, ranging between 0 and 1, describes how the profile roughness changes with scale, with a smoother and more persistent trend in larger scales, for higher values. The pre-factor, C, on the other hand, gives information about the amplitude of roughness and is used for comparing the relative roughness of multiple profiles (Candela et al., 2012).

The estimated roughness amplitude also exhibits time-dependent behavior (black curve in Figure 4.3b), which has an 87 ± 3% correlation with creep rate difference. This means that surface LOS creep is rougher during the SSEs, likely due to more heterogeneous creep distribution on the fault. In other words, each observed SSE results from an ensemble of localized creep avalanches, namely clusters of accelerated creep exceeding the long-term rate (Khoshmanesh & Shirzaei, 2018b). These bursts aseismically rupture isolated fault segments, separated by stable creeping patches, instead of a single burst rupturing the entire extent of the fault.

4.1.2. Possible Mechanism of Slow Slip Events

In order to nucleate SSEs several mechanisms are suggested, including velocity-weakening frictional properties of certain materials at very low velocities (Kaproth & Marone, 2013; Shibazaki & Iio, 2003), and frictional strength reduction with steady slip, i.e., slip weakening (Ikari et al., 2013). Stress perturbations due to nearby earthquakes or pore pressure variations are also suggested to generate transient SSEs on the unstable-stable transition zone with velocity-neutral properties (Liu & Rice, 2007). Switching to velocity-strengthening properties at higher (sub-seismic) creep rates (Kaproth & Marone, 2013; Shibazaki & Iio, 2003), and frictional dilation leading to a reduction of pore pressure (Segall et al., 2010), on the other hand, are proposed as mechanisms for arresting the premature slip in SSEs, preventing these events from turning into an earthquake. The combination of these nucleation and arrest mechanisms are used to simulate SSEs on the downdip end of the seismogenic zone in subduction faults (Liu & Rice, 2007), where creep velocity reaches up to 10^2 - 10^3 times the tectonic shearing rate (Iio et al., 2002; Kato et al., 2012). However, much slower semi-periodic accelerated creep events that are shown to occur on the entire seismogenic depth of the CSAF

(section 2.4.4) (Khoshmanesh et al., 2015; Nadeau & McEvilly, 2004) which exhibits velocity-strengthening properties (Carpenter et al., 2011; Carpenter et al., 2015), likely belong to a new class of SSEs. These require a new explanation, perhaps based on localized perturbation of shear strength on the fault (Perfettini & Ampuero, 2008).

The common aspect of aforementioned mechanisms for initiation of SSEs is the requirement of a constant or transient near-lithostatic pore pressure. In subduction zones, elevated pore pressure is speculated to be caused by dehydration of hydrous minerals in a down-going plate (Kodaira et al., 2004). But, the mechanism for pore pressure fluctuations on crustal transform faults is less clear. The inflow of mantle-driven fluid (Fulton & Saffer, 2009; Rice, 1992) into the highly permeable active fault zone of CSAF, as an existing hypothesis, implies a time lag between SSEs at different depths, which is not supported by slip models (Khoshmanesh et al., 2015), presented in section 2.3. Thermal pressurization due to shear heating (Schmitt et al., 2011) is an alternative explanation for the elevation of pore pressure, which results in seismic rupture nucleation. However, this mechanism is significant only when the creep rate reaches orders of magnitude higher than the maximum rate of SSEs on the CSAF (Schmitt et al., 2011). Compaction of intergranular pore spaces within the hydraulically isolated fault core (Byerlee, 1993; Sleep, 1995; Sleep & Blanpied, 1992), on the other hand, can serve as a viable mechanism for cyclic elevation of pore pressure on CSAF. Elevated pore pressure in this mechanism is self-generating (Byerlee, 1993), and does not require an external fluid source.

4.2. Rate and State Friction Modeling

To investigate the role of pore pressure variation in generating SSEs, the time series of effective normal stress rate on the fault is quantified using a rate and state friction model

under a steady-state condition. The effective normal stress, $\sigma_e = \sigma_n - p$, where σ_n is tectonic normal stress and p is the pore pressure, is related to steady-state shear stress (τ_{ss}) through:

$$\tau_{ss} = \sigma_e(f_0 + (a-b)log\frac{V_{ss}}{V_0}) \tag{4.1}$$

In this equation, f_0 is nominal coefficient of friction, $(a-b)$ is the frictional rate parameter, V_{ss} is the steady-state rate and V_0 is the reference creep rate (Ruina, 1983). The shear stress change on fault patch i between time steps t_1 and $t_2 = t_1 + dt$ is estimated through (Perfettini & Avouac, 2007):

$$\tau(i,dt) = \dot{\tau}_0 dt + d\tau(i,dt) \tag{4.2}$$

in which the first term on the right side is the stress due to tectonic plate loading with $\dot{\tau}_0$ = 0.25 bar/year (Parsons, 2002). The second term accounts for the imparted stress due to slip on the adjacent fault patches, provided by:

$$d\tau(i,dt) = \sum_{j=1}^{n} G(i,j)d(j,dt) \tag{4.3}$$

where slip (d) on the fault, discretized into n dislocation patches, is obtained from the time-dependent model of creep along the CSAF presented in section 2.3 (Khoshmanesh et al., 2015). The elastic kernel, $G(i,j)$ represents the shear stress change at the patch i due to a unit rake-directed slip on patch j. This kernel is defined by the analytical solution of a rectangular dislocation buried in an elastic half-space (Okada, 1992), with Poisson ratio and shear modulus of 0.25 and 30 GPa, respectively. Figure 4.4 demonstrate the temporal average and standard deviation of the shear stress rate on the CSAF. Without loss of generality, $V_0 = V_{lt}(i)$ is chosen, where $V_{lt}(i)$ is the long-term creep rate estimated for each fault patch along CSAF, obtained in section 2.3. Time series of V_{ss}, which is considered as the rate of creep between

consecutive time steps, is also obtained from the time-dependent model of section 2.3 (Khoshmanesh et al., 2015). Moreover, based on the laboratory experiments on SAFOD samples (Carpenter et al., 2015), frictional parameter $(a-b)$ and coefficient of friction (f_0) are chosen to be 0.01 and 0.1 for entire fault, respectively. Given that $\tau(i,dt)$ and, therefore

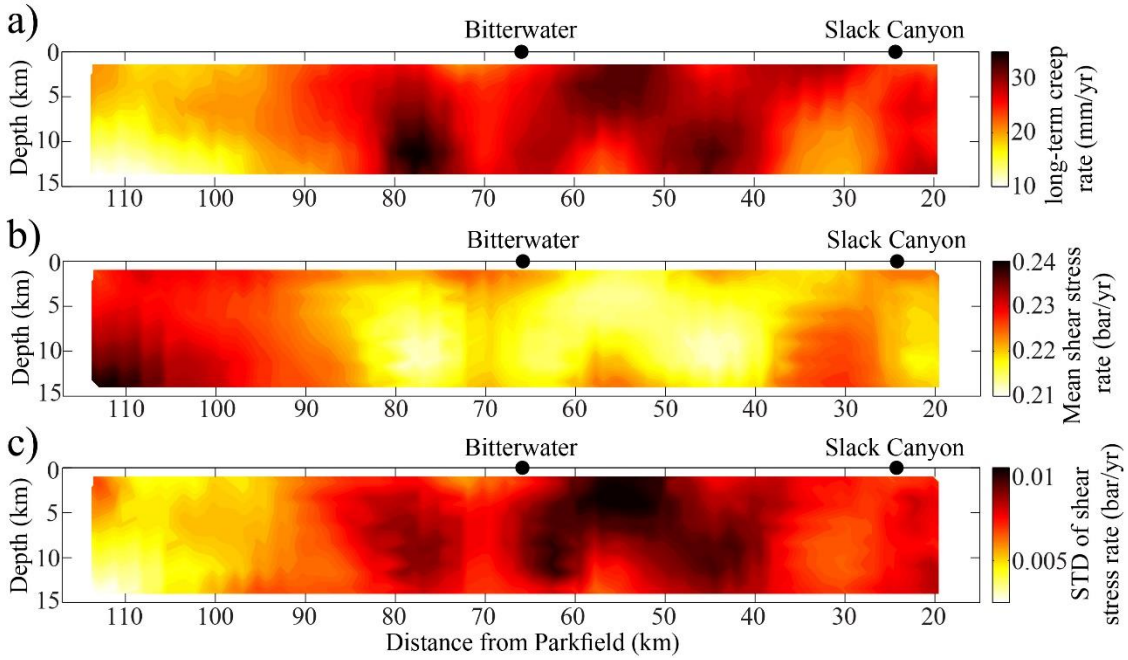

Figure 4.4. Estimated shear stress and uncertainty. (a) Spatial distribution of long-term modeled creep rate from section 2.3 (Khoshmanesh et al., 2015) in mm/year. (b) temporal average, and (c) and standard deviation of shear stress rate along the CSAF in bar/year.

estimated σ_e are a function of interval between consecutive time steps, our estimates could be affected by irregular temporal sampling of creep model. Therefore, temporally-normalized effective normal stress with respect to period between consecutive time steps is presented and discussed. Spatial distribution of average rate of σ_e and its standard deviations are depicted in Figure 4.5. The estimated effective normal stress rate depicts the spatiotemporal variation of pore pressure along the CSAF, given that there is no evidence for variable tectonic normal stressing rate during our study period. Averaging along the fault and comparing the temporal evolution of effective normal stress rate (green curve in Figure 4.3b) with that of surficial creep

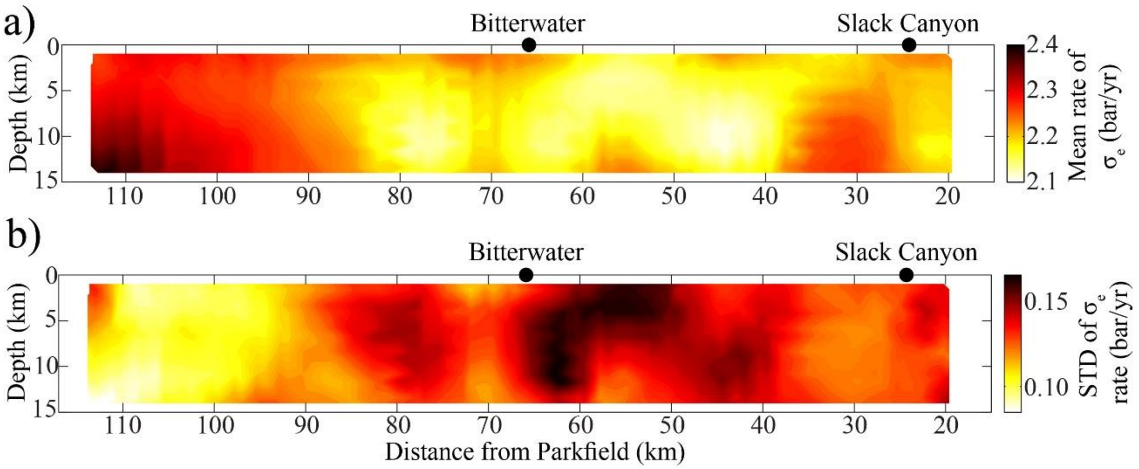

Figure 4.5. Estimated effective normal stress. Spatial distribution of (a) temporal mean and (b) standard deviation of effective normal stressing rate along the CSAF in bar/year.

rate difference, it is evident that an increase (decrease) in average LOS creep rate corresponds with reduction (increases) in the effective normal stressing rate that is attributed to pore pressure elevation (reduction).

4.3. Gutenberg-Richter *b*-value

Microseismicity, a distinguishing attribute of creeping faults (Malservisi et al., 2005), can also provide insight into the temporal evolution of fault strength and shed light on the possible mechanism for transient events. Here, the Gutenberg-Richter *b*-value is estimated to further investigate the temporal change of effective normal stress on the fault. The *b*-value time series shows the temporal evolution of the ratio of smaller to larger earthquake, which is negatively related to the effective normal stress on the fault (Schorlemmer et al., 2005; Tormann et al., 2013). Gutenberg-Richter law relates the frequency of occurrence to the magnitude of earthquakes through

$$\log_{10} N = a - bM \tag{4.4}$$

where N is the cumulative number of events larger than magnitude M, and a and b are constants (Richter, 1958). To obtain the parameter b (so-called *b*-value), the maximum likelihood estimation (MLE) method is implemented (Bender, 1983; Utsu, 1965). Using this method:

$$b_{MLE} = \log_{10}\left(\frac{e}{M_m - (M_c - \delta M/2)}\right) \tag{4.5}$$

where M_m is the mean magnitude, M_c is the magnitude of completeness, e is the Euler's number, and the magnitudes are rounded to $\delta M = 0.01$. The associated standard deviation can also be calculated using (Shi & Bolt, 1982):

$$\sigma_b = 2.30 \times (b_{MLE})^2 \sqrt{\sum_{i=1}^{n} (M_i - M_m)^2 / n(n-1)} \tag{4.6}$$

where n is the size of observation window, containing n earthquakes with magnitudes M_i.

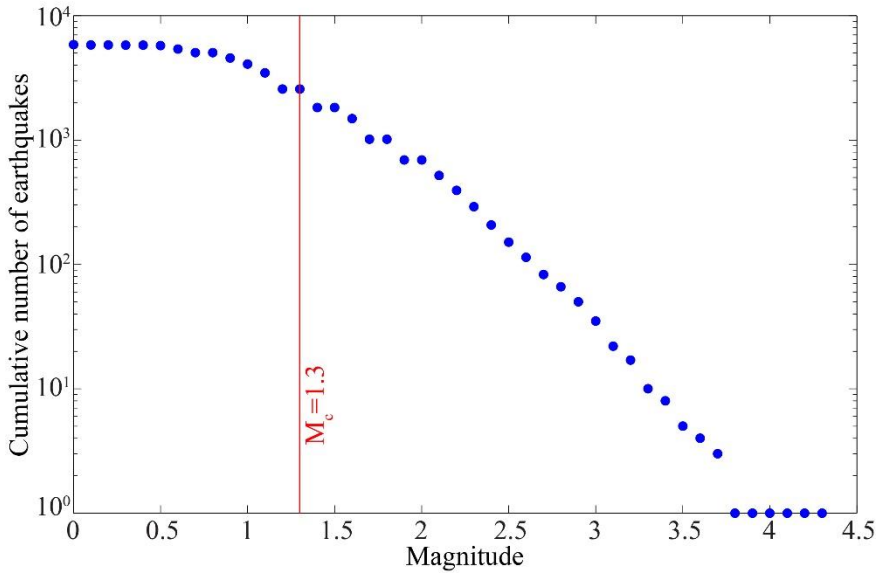

Figure 4.6. Frequency-Magnitude distribution of all the earthquakes used for b-value time series analysis.

To avoid underestimation of *b*-value, one needs to carefully consider the completeness magnitude (M_c) for a given seismic catalogue (Woessner & Wiemer, 2005). Following previous

estimations of completeness magnitude for the seismic catalogue near CSAF and Parkfield segment (Schorlemmer et al., 2004; Tormann et al., 2013; Tormann et al., 2014), M_c = 1.3 is used here. To account for the distribution of events near the fault surface, a distance-dependent weight is assigned to all the earthquakes in the vicinity of the fault. An exponential weighting function, $w(D) = \zeta e^{-\zeta D}$, is used (Tormann et al., 2014), in which D is the closest distance between earthquake hypocenter and the fault surface, and ζ = 0.7 (Tormann et al., 2014). Various values of ζ ranging from 0.3 to 1 have been tested and all yield comparable results. Given its relatively homogeneous and fast rate of creep, the central zone (km 20 to 90) is considered for *b*-value calculation. The magnitude distribution of all the earthquakes considered for this analysis is shown in Figure 4.6.

Sorting the earthquakes based on the occurrence time, n number of events is used as the size of the moving window, without any overlap between consecutive windows, to estimate the time-dependent *b*-value (Tormann et al., 2013). The optimum size of this moving window is estimated through a Monte Carlo search algorithm (Tormann et al., 2014). To this end, 1000 synthetic earthquake catalogues with true *b*-value of b_0 = 1 is simulated using:

$$M = (M_c - \delta M/2) - \log(r)/\beta \tag{4.7}$$

in which $\beta = b_0 \times \log(10)$, and r is a set of random numbers between 0 and 1, produced using Matlab's *rand* function (Tormann et al., 2014). The number of events in each synthetic catalogue and their weight as a function of distance from the fault are the same as that of the CSAF observed seismic catalogue. To identify the acceptable range of window size, a range of n from 50 to 300 with steps of two is tested. As a result, a time series of *b*-value as a function of n, per synthetic catalogue is obtained. Next, the time series of mean *b*-value and associated standard deviation is calculated for each window size n, considering the estimated values for

different time steps across all 1000 simulations. For each window size, the highest standard deviation and the maximum difference between mean *b*-value time series and the true value of $b_0 = 1$, are considered as the representative precision and accuracy of the time series (Figure 4.7). The criterion for acceptable window sizes is the associated accuracy and precision being less than 5% and 10% of the true *b*-value, respectively. It is found that the accuracy of the estimated mean *b*-value time series is acceptable for the window sizes of larger than ~60 events (Figure 4.7). However, considering the precision criterion, the Monte Carlo search algorithm

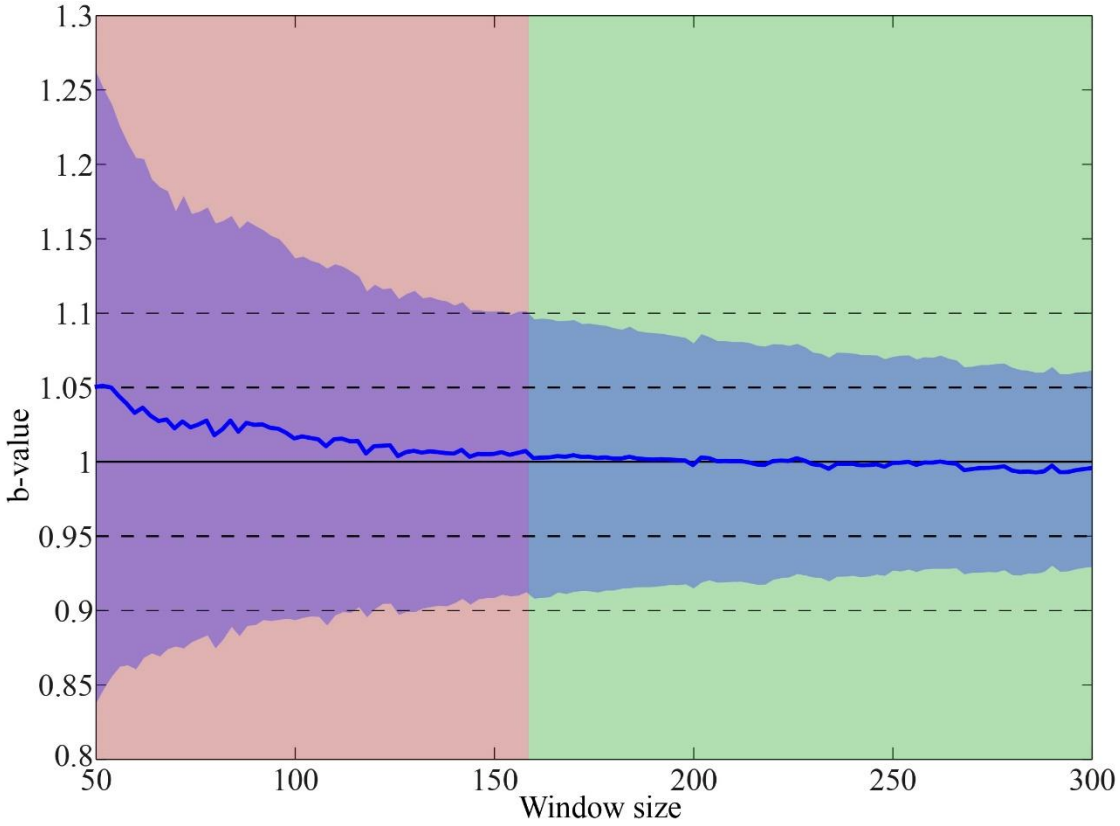

Figure 4.7. Optimization of the window size using the Monte Carlo search algorithm. The blue curve shows the estimated mean *b*-value for each window size across 1000 random simulations. The shaded blue area shows the standard deviation of estimated *b*-value. For each sample size, the *b*-value and the corresponding standard deviation associated with the time step with maximum uncertainty across all simulations is shown. The true *b*-value of b_0=1 is shown by the horizontal solid black line. The two thick and thin dashed lines indicate the acceptable range of accuracy and precision, respectively. The green and red shaded area highlights the range of acceptable and unacceptable sample size, respectively.

results in an optimum window size of larger than 160 events (Figure 4.7). The preferred *b*-value time series, shown in Figure 4.3a is estimated using window size of 170 events, which yields a sampling rate of roughly half a year (Figure 4.8).

The temporal evolution of estimated Gutenberg-Richter *b*-value (brown curve in Figure 4.3a), exhibits a 60±8% correlation with the variation of LOS creep rate difference, showing clear increase in *b*-value during the dominant SSEs on the CSAF. However, the reason for poor correlation starting in 2009 and before mid-2004 is unclear. Moreover, time series of the total seismic moment of microearthquakes exhibits a negative correlation with *b*-value and

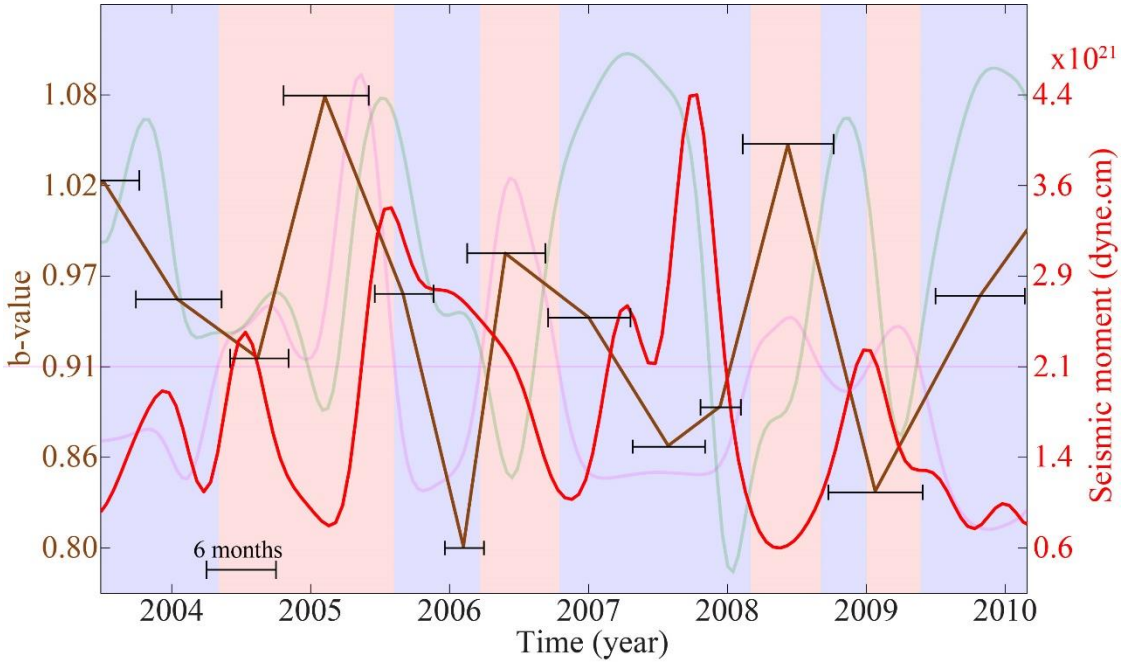

Figure 4.8. Time series of the released seismic moment (in red) calculated using moving temporal window of 3 months for the earthquake within 2 km distance from the central segment of the CSAF (from 20 to 90 km), versus the estimated *b*-value (in brown) considering M_c = 1.3. The horizontal error bar on each estimated *b*-value shows the time interval encompassed by that estimation. A reference error bar with a length of 6 months is provided in the bottom left of the Figure. The magenta and green curves in the background respectively show the average rate difference and effective normal stress rate as shown in the Figure 4.3. Beside the *b*-value, the other time series are smoothed using a Gaussian smoothing filter of size 6 months.

surface creep rate (Figure 4.8). This suggests that larger microearthquakes (lower *b*-value) occur when the fault is creeping with a relatively slower rate (Tormann et al., 2013), due to

pore pressure drop leading to re-strengthening of the fault. A similar conclusion can also be reached by comparing earthquake counts and the creep rate difference (Figure 4.9), which suggest that microseismic activity maximizes when the frictional strength is increased. This is followed by a decline in microseismicity when the pore pressure is elevated while CSAF is

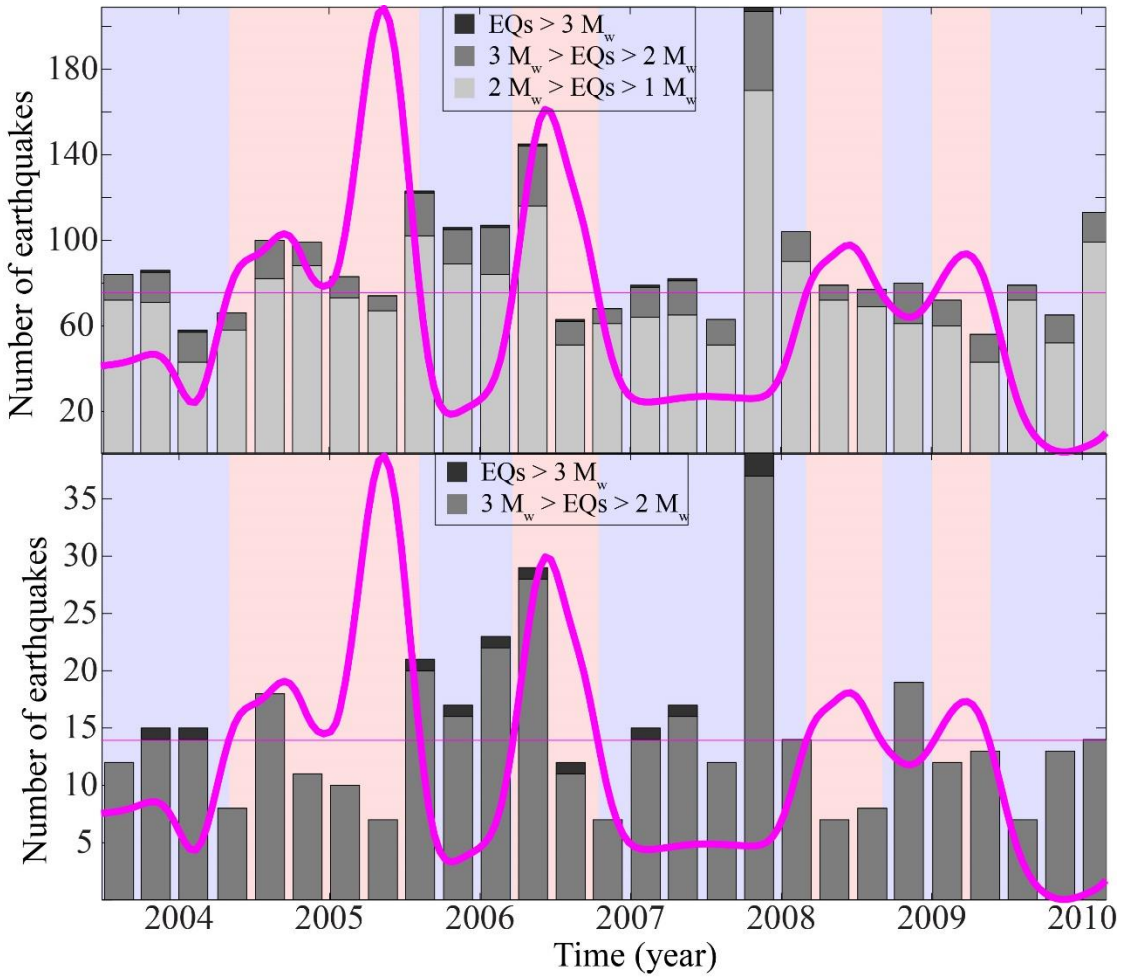

Figure 4.9. Time series of the earthquakes count for the microseismicity within 2 km distance from the central segment of the CSAF (from 20 to 90 km). A temporal window of 3 months is used for this calculation. The magenta curve shows the average rate difference as shown in the Figure 4.3. Top panel considers all the earthquakes larger than M_w 1.0 with light gray showing the count for M_w 1.0 < EQs < M_w 2.0, gray for M_w 2.0 < EQs < M_w 3.0 and dark gray for M_w 3.0 < EQs. The bottom panel only considers earthquake larger than M_w 2.0, with colors as defined above. No temporal smoothing is applied to the time series of earthquake count.

experiencing an episode of SSE. Spatiotemporal distribution of seismic moment along the CSAF and adjacent locked segments is also overlain on the distribution of LOS creep rate

difference (Figure E.1 in Appendix E). Comparisons confirm that segments with elevated seismic moment release are predominantly creeping slower than the long-term rate (indicated by the colder colors).

4.4. Preferred Mechanism Driving Creep Events on San Andreas Fault

Observations and analyses presented here suggest that elevated pore pressure possibly driven by compaction (Byerlee, 1993; Sleep, 1995; Sleep & Blanpied, 1992) and subsequent frictional dilation (Segall et al., 2010) are responsible for initiating and arresting the episodic SSEs along the CSAF. Within a dilated fault zone with an average pore pressure below lithostatic, intergranular pore spaces undergo compaction due to ductile creep (Sleep, 1995). Under an undrained condition, namely being hydraulically isolated from the surrounding country rock through a permanent impermeable seal layer (Blanpied et al., 1992), compaction results in increased pore pressure to lithostatic level (Sleep, 1995; Sleep & Blanpied, 1992), which correlates with incipient creep acceleration (Leclere et al., 2016). Considering a compressibility of 10^{-10} to 10^{-9} Pa^{-1}, a porosity reduction of 1 - 6% at depth of 8 km results in elevation of pore pressure from hydrostatic to lithostatic level. Due to the heterogeneous fault zone material and geometrical irregularity of the fault surface, however, rate of porosity reduction due to compaction is not the same for the entire fault, leading to heterogeneous distribution of overpressurized fluid on the fault (Hillers & Miller, 2007; Mittempergher et al., 2011). Moreover, extremely low permeability of fault gouge on CSAF (10^{-23} to 10^{-21} m^2) (Morrow et al., 2014) reduces the rate of specific discharge from zones of elevated pore pressure. This divides the fault into natural compartments with different fluid pressures, resulting in a heterogeneous distribution of pore pressure across the seismogenic zone (Byerlee, 1993; Lockner & Byerlee, 1995). The isolated creep bursts, therefore, pinpoint the

location of these overpressurized compartments along the CSAF. An ensemble of these localized creep burst, observed as heterogeneous creep rates on the surface, which is quantified using increased roughness estimates makes up the episodic SSEs.

Frictional dilation (Segall et al., 2010) due to accelerated creep, on the other hand, restores the porosity and re-strengthens the overpressurized compartments, which is correlated with the incipient creep deceleration (Leclere et al., 2016). Frictional dilation also increases the permeability of fault gouge, which leads to redistribution of fluid within the fault zone, and therefore homogenous distribution of pore pressure along the fault (Sleep, 1995; Sleep & Blanpied, 1992). This coincides with decelerated creep rate with a spatially uniform pattern throughout the fault, observed as a smoother surface creep rate distribution (Figure 4.10), which also marks the initiation of the next compaction cycle. The increased effective normal stress during creep deceleration, causing negative Coulomb stress changes, may additionally trigger slip transients, which are characterized by significantly smaller amplitude, and temporal delays proportional to the size of stress perturbations (Perfettini & Ampuero, 2008). Nonetheless, modulation of these dilation-induced slip transients onto the compaction-induced SSEs might be responsible for some of the irregularity that we observe in amplitude and timing of the SSEs on the CSAF.

In this mechanism, therefore, creep rate variation is not instantaneous, and instead, creep evolves in consecutive intervals of acceleration and deceleration, which correlate with similar variations in pore pressure. This is consistent with the results of laboratory experiments, documenting the role of elevated pore pressure and decreased permeability in generating the transient events (Leclere et al., 2016). The observed concurrence of the decreased *b*-value and increased number of microseismic events and their released moment during the decelerated creep, when the frictional strength is elevated, is also aligned with our

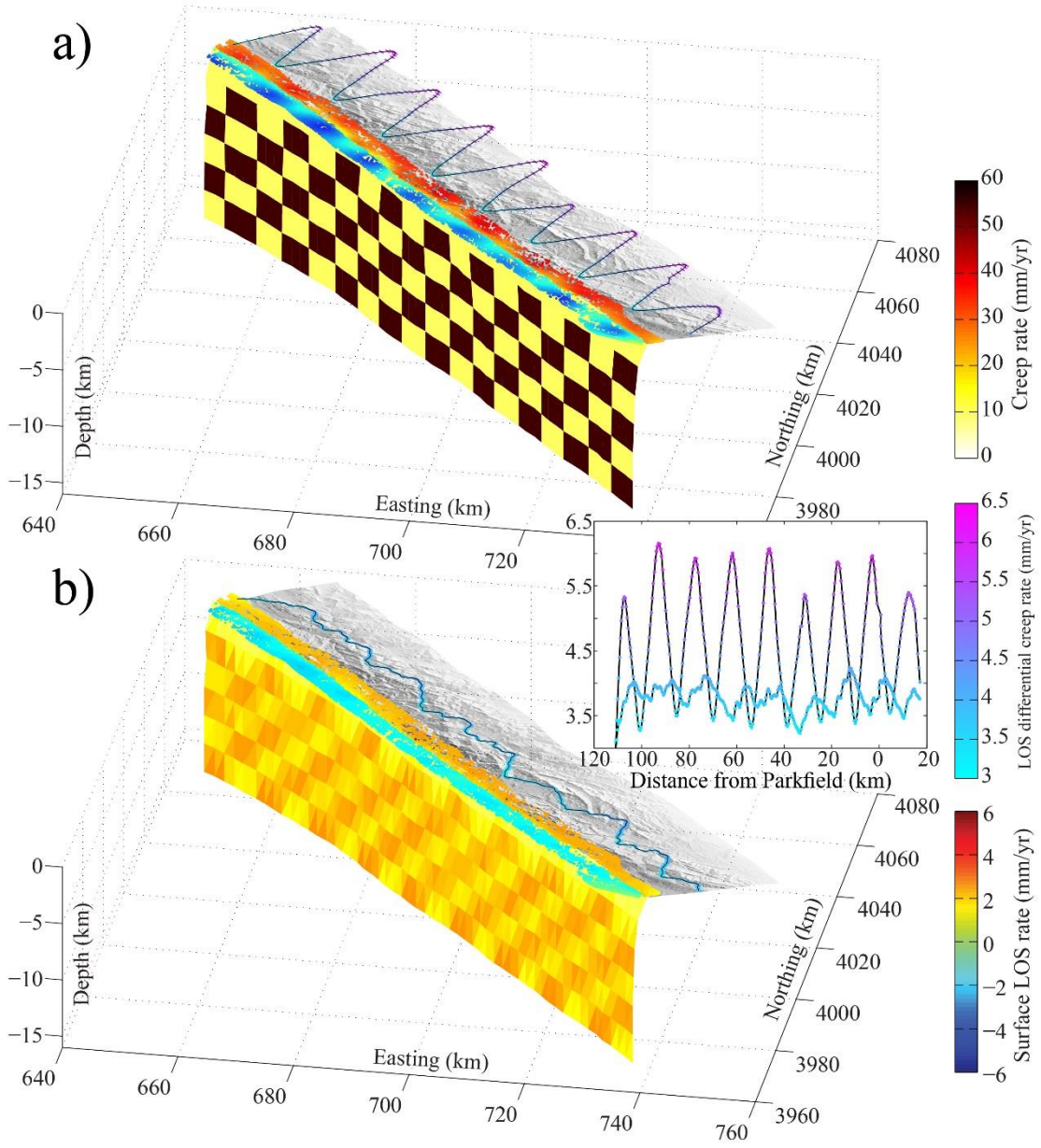

Figure 4.10. Conceptual model of creep distribution on a fault that undergoes compaction and frictional dilation. Modeled surface observation in LOS direction from two different scenarios for spatial distribution of creep rate (and pore pressure) along the CSAF. Creep rate on the fault is shown with color scale from yellow to black. Rainbow color scale is used for the LOS creep rate on the surface, estimated through forward modeling of the considered creep distribution on the fault. The resulting near-distance LOS creep rate, estimated using the moving window is also shown in the middle panel, using the color scale from cyan to magenta. (a) Resulting from scenario #1 in which pore pressure is heterogeneously distributed within idealized rectangular compartments formed as a result of compaction of intergranular pore spaces. These compartments are considered to form in depths of more than 3 km. A 60 and 10 mm/year creep rate, respectively, is considered for the high and low pore pressure compartments. (b) Resulting from scenario #2, in

which the porosity and permeability is increased due to accelerated creep events and pore pressure is more homogenously distributed within the fault. The creep rate in this scenario is considered to vary between 10 and 25 mm/year across the fault, with relatively more homogeneous distribution compared to scenario #1. The middle panel compares the near-field LOS creep rate estimated from the two scenarios to emphasize the difference in the roughness of resulted profiles.

proposed mechanism for SSEs on the CSAF (Byerlee, 1993; Lockner & Byerlee, 1995; Sleep & Blanpied, 1992). This suggested mechanism does not require an external fluid source (Byerlee, 1993; Sleep, 1995; Sleep & Blanpied, 1992), which makes it a favorable explanation for the observed variation of creep rate on other velocity-strengthening crustal faults (Jolivet et al., 2015a) and possibly subduction zones.

4.5. Slow Slip Events Impact on Seismic Hazard

SSEs are suggested as a mechanism for triggering major earthquakes on subduction zones (Kato et al., 2012; Schurr et al., 2014; Uchida et al., 2016) and as also being triggered due to adjacent earthquakes on crustal faults (Shelly et al., 2011; Shirzaei et al., 2013; Wei et al., 2015). Distribution of the seismicity (Waldhauser & Schaff, 2008) along the CSAF and the transition segment to the south (From km −50 to 115 km in Figure 4.2) reveal that earthquakes larger than M_w 4, including the 2004 M_w 6 Parkfield earthquake, occurred during SSEs on the CSAF. The timing of the earthquakes in the northern locked segment (From km 115 to 160 in Figure 4.2), however, is not correlated with the timing of SSEs on the CSAF, perhaps due to more complex fault structure in this segment. The observations show that initiation of the accelerated creep phase on the creeping segment precedes the 2004 earthquake, suggesting that this seismic event could have been triggered due to stress transfer from this SSE. The estimated Coulomb failure stress at the hypocenter shows that the rate of imparted stress increased up to 0.45 bar/year during the SSE. The time series of Coulomb failure stress change

ΔCFS is estimated using the time dependent model of creep on the CSAF presented in section 2.3 (Khoshmanesh et al., 2015). The total shear ($\Delta\tau$) and normal stress ($\Delta\sigma$) imposed at the earthquake hypocenter in each time step is estimated as superposition of the stress imparted by creep at all patches across the CSAF (Okada, 1992). The Coulomb failure stress change $\Delta CFS = \Delta\tau - \mu\Delta\sigma$ is then estimated assuming a friction coefficient of $\mu = 0.6$ on a fault with the mean strike (313°) and dip (86°) of the CSAF.

The ruptured asperity of the 2004 event, on the other hand, slowly re-ruptured in the form of a localized burst during the following episodes of SSE on the CSAF (bursts B and D in Figure 4.2). This calls for an additional explanation for the complex response of the Parkfield transition zone to the SSE on the CSAF, and most importantly the underlying triggering mechanism of the 2004 event. A closer examination of the creep rate difference distribution suggests that a combination of a significant localized burst (burst A in Figure 4.2), initiated about one year prior to this event, persistent until the time of nucleation, and the SSE on the CSAF might have triggered this earthquake. The coseismic slip distribution of this earthquake (Johanson et al., 2006) also suggests that the area experiencing the maximum coseismic slip has an overlap with the burst A. This is likely due to thermal pressurization of fluids (Schmitt et al., 2011) in addition to the pre-existing compaction-induced elevated pore pressure. This observation is also supported by a distinguishable increase in the microseismicity, following another significant local burst that occurred between 2007 and 2009 at the northern end of study area (burst C in Figure 4.2), having similar scale and amplitude to that of burst A. These findings highlight the role of observation and analyses of the surface creep rate to detect the SSEs and significant local bursts to improve the time-dependent estimates of seismic hazard associated with transform faults (Khoshmanesh & Shirzaei, 2018b). Moreover, considering the periodicity of these SSEs as opposed to the conventional

assumption of a constant loading rate, time-dependent probabilistic earthquake forecast models can be greatly improved.

CHAPTER 5.

EPISODIC SLOW SLIP EVENTS ON NORTHEAST JAPAN SUBDUCTION ZONE AND ASSOCIATED SEISMIC HAZARDS

5.1. Data

The NJSZ is one of the best instrumented subduction zones, with extensive GPS and seismic networks on mainland Japan. Its GNSS Earth Observation Network (GEONET) consists of over 1,200 stations (Sagiya, 2004; Sagiya et al., 2000). This comprehensive monitoring is motivated by the fact that Japan lies in a very tectonically complex region, whereby four tectonic plates (the Pacific, Amurian, Okhotsk, and Philippine Sea) converge. In this study, the central part of the NJST is considered, between 37 - 41° latitude (yellow box in Figure 5.3), where the Pacific plate subducts underneath the Okhotsk plate at a rate of ~8 cm/yr (Apel et al., 2006; DeMets et al., 2010). Since there were no earthquakes larger than M_w 6.5 in this area during 1996 - 2003, this interval is considered to represent the interseismic period on the NJSZ. To estimate the spatiotemporal distribution of interseismic slip on the subducting slab, the daily GPS daily solutions from 21 March 1996, the earliest measurement in the GPS dataset, to 24 September 2003 provided by Ozawa et al. (2012) is used. The termination of interseismic period is marked by the M_w 8.3 Tokachi-Oki earthquake that occurred on 25 September 2003 in the north of considered study region (Miyazaki & Larson, 2008), and a large proportion of the GEONET stations recorded co- and post-seismic signals from this event. In addition to the GPS observations, the CRE dataset from Uchida and Matsuzawa (2013) is also used to constrain the daily distribution of creep on the NJSZ.

5.1.1. Global Positioning System data set

The GPS displacements from the dataset reported in Ozawa et al. (2012) are used in this study. These data were analyzed daily using the Bernese GPS software and are provided in the stable Eurasian reference frame after Apel et al. (2006). The resulting RMSE of the data are 3 and 15 mm, for the horizontal and vertical components, respectively. In this study, only the horizontal components are considered due to the low signal to noise ratio for the vertical component and the contribution from subduction erosion that adds additional complexity to the vertical deformation data (Heki, 2004).

To isolate the signal due to creep, a refinement procedure is implemented, through which the signals due to nearby inland earthquakes, the effect of the long-term convergence rate, and seasonal components are removed. Since the number of available stations varied annually, the data are refined separately for each year. To account for nearby ($\geq M_w$ 7.0) earthquakes, the coseismic offset due to the M_w 7.0 intra-slab thrust event on 26th May 2003 (Ozawa et al., 2003) is removed for stations in the Miyagi prefecture, by subtracting displacements on the day after, from the day before. However, signals due to possible afterslip of several moderate ($6 \leq M_w \leq 6.5$) earthquakes and postseismic relaxation are not corrected for, consequently the creep model could include these effects.

To account for the long-term convergence rate, the effect of common mode noise is further removed from GPS network, following Wdowinski et al. (1997). The common mode noise is a linear combination of the entire network translation and rotation, which is calculated for each time step by analyzing the stations that are outside the Tohoku area (Mavrommatis et al., 2014). This selection of fiducial stations is to ensure that the estimation of common mode noise is not affected by creep on the subduction zone (depth < 70 km). Following this correction, the observed displacement at each station includes the effect of creep within the

upper 70 km of the subduction zone. In the next step, a function formed as a linear combination of sine and cosine functions with periods of 0.5 - 2 years is fitted to the time series of the east and north components for each station using a least squares approach. The optimum function is then subtracted from the time series to remove the possible effect of seasonal signals.

To remove anomalous stations that are affected by non-tectonic signals, such as volcanic processes, monument settlement, land subsidence, and inland seismicity, the long-term velocity of each station is compared with the median value of surrounding stations within

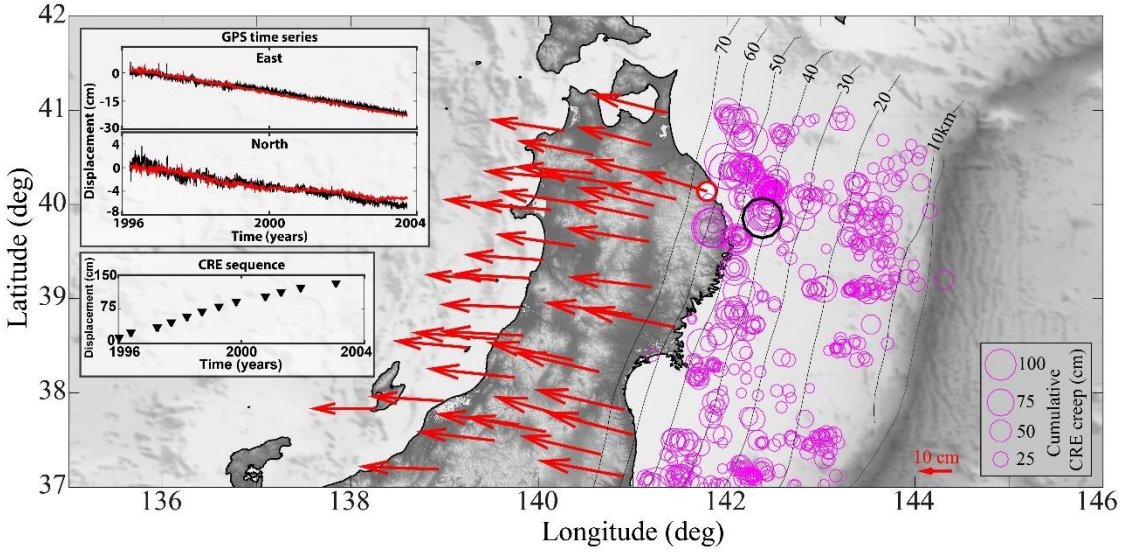

Figure 5.1. GPS and CRE observation. Cumulative horizontal displacement observed by 41 GPS stations (red arrows) and cumulative aseismic slip observed by CREs (pink circles) between 21 March 1996 and 24 September 2003. Depth of subducting slab is shown using the black thin contour lines. Inset (top panel): East and North components of the GPS time series for one station, whose location is shown by the red circle. The black line refers to the original data from Ozawa et al. (2012), and the red line is the resulting time series after accounting for coseismic shifts, the effect of the convergence rate and seasonal fluctuations. Inset (lower panel): An example time series of the cumulative displacement from one CRE family, whose location is denoted by the black circle.

a 50 km radius. The station is removed from the data set if its long-term rate is not within 15% of the estimated median. For the remaining stations, their spatial similarity is characterized using an approach similar to that used to estimate coherence in radar interferometry (Hanssen,

2001). Given the displacement in the east (d_E) and north (d_N) directions, at n stations surrounding arbitrary station k, the spatial coherence ρ_k^t at time step t for this station is defined as:

$$\rho_k^t = \frac{\left|\sum_{i=1}^{n} d_i^t d_i^{t-1}\right|}{\sqrt{\sum_{i=1}^{n} \left|d_i^t\right|^2 \sum_{i=1}^{n} \left|d_i^{t-1}\right|^2}} \tag{5.1}$$

in which, d_i^t is either of east or north components of the displacement at station $i = 1, \ldots, n$ at time step t. The value of equation (5.1) is between zero and one, and it is separately estimated for the east and north component of the GPS data. The spatial coherence is used to estimate the weight of the observations in the inversion process.

The resulting cumulative displacement for a subset of 41 stations that were consistently measuring throughout the study period is shown in Figure 5.1. Note that the actual number of stations used for inversion varies between 278 and 480 from year to year. The inset in Figure 5.1 compares the refined time series for an example station (red lines) with the original dataset (black lines).

5.1.2. Characteristically Repeating Earthquakes

Characteristically repeating earthquakes (CREs) are thought to be associated with the quasi-periodic failure of relatively small asperities, occupying less than 1% of the active fault surface, that are loaded due to surrounding aseismic slip (Nadeau et al., 1994; Nadeau & Johnson, 1998). The seismic moment release provides quantitative information about the amount of slip involved in these seismic events. Uchida and Matsuzawa (2013) identified CREs on the NJSZ between 1984 and 2012 using cross-spectral analysis and grouped them into CRE sequences occurring at discrete locations on the subducting plate interface. To ensure that the

slip inferred from CREs is representative of slip on the upper Pacific plate and is not affected by the motion of the Philippine Sea plate, only CREs occurring above 37° N latitude are used. The down-dip extent of the CREs is limited to 60 - 65 km depth. The location and cumulative

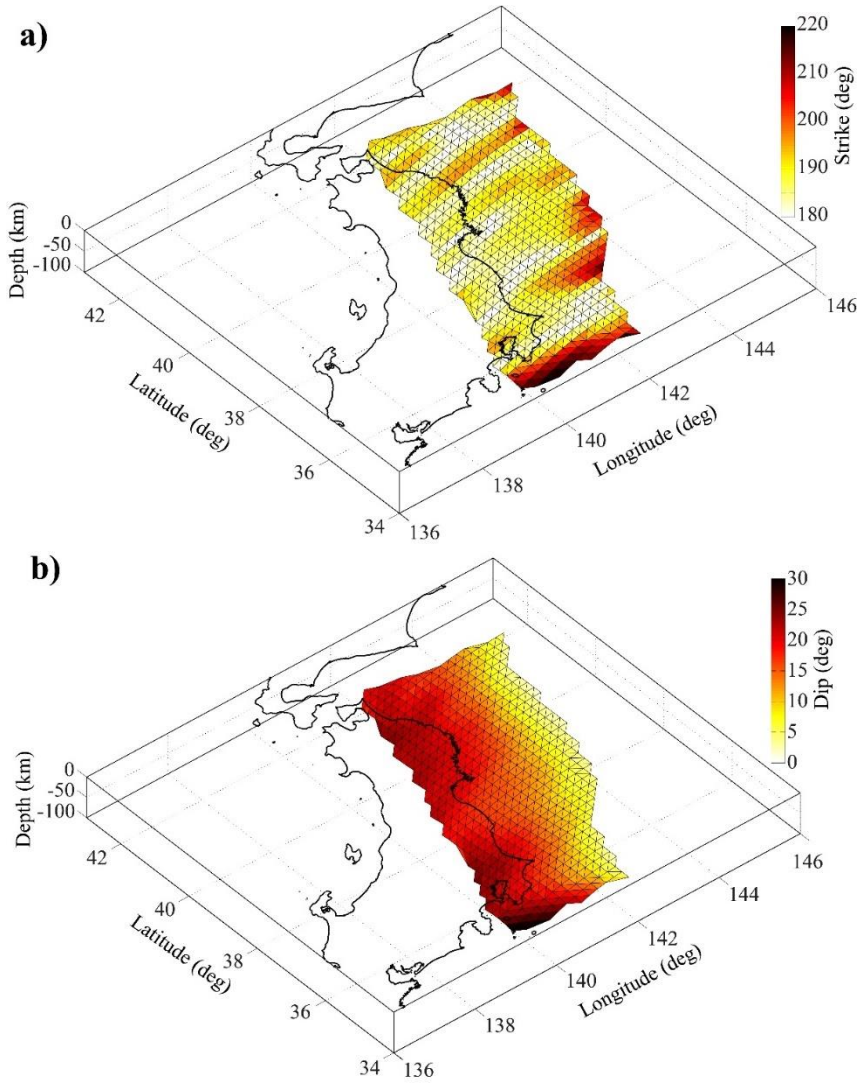

Figure 5.2. The fault geometry from Slab1.0 (Hayes et al., 2012), which is determined using a variety of seismic datasets and bathymetry data. Colors represent the (a) strike and (b) dip angle of the considered fault model.

slip from CREs that occurred during the interseismic period 1996 - 2003 are shown as pink circles in Figure 5.1. An example of cumulative time series of CRE creep is shown in the inset of Figure 5.1. In the context of the 2011 Tohoku, most of the CREs occurred outside the large-coseismic-area (> 30 m) (Figure 5.3).

To use the CRE observations as a constraint in the time-dependent inversion framework, the data set is interpolated in time. To this end, first a linear regression is applied to each CRE sequence with more than three events, to determine the average creep rate. This is then used to estimate a daily time series of creep for every CRE location. A spatial oversampling scheme is also applied to estimate the time series of CRE creep for each triangular patch. To this end, a 50 km search radius centered on each patch is used to assign the CRE time series and locations to the mesh representing the subducting plate (Figure 5.2). The optimum value of 50 km radius is chosen as it results in the assignment of a value to each triangle, whilst avoiding the possibility of oversmoothing the CRE distribution. Lastly a median filter of 100 km × 100 km is used at each time step (one day) to spatially smooth the assigned slip. This procedure provides creep rate bounds for use in the time-dependent inversion, which range on average between 0 to 0.2 cm/day.

5.2. Methods

5.2.1. Time-Dependent Slip Inversion

To associate the GPS displacements with creep on the subducting plate interface, a two-step time-dependent inverse modelling scheme (Khoshmanesh et al., 2015; Shirzaei & Bürgmann, 2013; Shirzaei et al., 2014) , as discussed in section 2.1.2, is used. In the First step, the GPS displacements are inverted to solve for a static creep distribution for each time step. This is followed by applying a linear Kalman filter (LKF) to static creep distributions in order to reduce the temporal noise (Grewal & Andrews, 2001). The creep (C_t) on each patch at each time step (t) is related to the GPS displacements, L_t as follows:

$$L_t + v_t = BC_t, \quad P_t = \sigma_0^2 \rho^t \sum\nolimits_{l_t, l_t}^{-1} \tag{5.2}$$

$$lb \leq C_t \leq ub, t = 1, 2, \dots, N$$

where, v_t is the vector of observation residuals, B is the Green's function, which is calculated assuming dip-slip motion and a Poisson ratio of 0.25, and P_t is the weight matrix. The variance-covariance matrix of the observations, represented by $\sum_{l_t,l_t}$, is a row-wise matrix with its elements calculated as the ratio of the spatial coherence estimated using equation (5.1) and the variance of the displacement. Therefore, the diagonal elements of $\sum_{l_t,l_t}$ are proportional to the inverse of the variance of the observations. Equation (5.2) is solved subject to a re-weighted L2-norm minimization of the observation residuals, whereby following each iteration the observations are re-weighted based on the residuals from the previous iteration (Shirzaei & Bürgmann, 2013). This approach allows the minimization of the effect of outliers and other observation artifacts (O'leary, 1990). The creep observed by CREs is used to define the upper (ub) and lower (lb) bounds of the creep during the inversion as follows;

$$\begin{aligned} ub &= C_{CRE} + \alpha S_L \\ lb &= \max\{0, C_{CRE} - \alpha S_L\} \end{aligned} \tag{5.3}$$

where, C_{CRE} is the mesh of creep estimated for each patch from the CRE data, described in section 5.1.2, S_L is the amount of creep with long-term convergence rate (8 cm/yr) for one day, as the inversion is done on a daily basis, and α is a factor determined from iterative testing with the optimum value of 200 (Weston & Shirzaei, 2016). During the inversion, it is ensured that the optimum creep is not converging to the lower or upper bound, and if this is the case then the bounds are extended. This approach ensures that areas with no creep observed by CREs are still allowed to creep in the inversion. However, it should be noted that the lower bound is less than zero, that is, backwards slip is not allowed. In the static inversion step, the second-order derivative of the creep distribution in each time step is also minimized to reduce

the roughness of the slip (Harris & Segall, 1987) using the equation $\gamma DC_t = 0$, where, D is the Laplacian operator and γ is the smoothing factor, which determines the roughness of the optimum creep model.

Following the optimization of the creep model for all observation times steps and determining the time series of the slip and the associated variance-covariance for each patch, the LKF is applied to reduce temporal noise. The LKF addresses the problem of estimating the parameters of a linear, stochastic system with measurements that are linear functions of the parameters. See Shirzaei and Bürgmann (2013), Shirzaei and Walter (2010), Khoshmanesh et al. (2015), and section 2.1.2 for more details on the LKF step. It should be noted that since the convergence rate is predominantly east-west, the signal to noise ratio for the north component is smaller than that for the east component. Therefore, east components of the GPS data are given more weight relative to the north components. A ratio of 8:1 for the east and north components, respectively, was selected following several tests with a range of ratios.

5.2.2. Gutenberg-Richter *b*-value Estimation

The Gutenberg-Richter law relates the frequency of occurrence to the magnitude of earthquakes through $\log_{10} N = a - bM$, where N is the cumulative number of events larger than magnitude M, and a and b are constants (Richter, 1958). To obtain the *b*-value, similar to Khoshmanesh and Shirzaei (2018a), the maximum likelihood estimation (MLE) method (equation (4.5)) with $\delta M = 0.1$ is implemented (Bender, 1983; Utsu, 1965). To account for the distribution of events near the fault surface, a distance-dependent weight is assigned to all the earthquakes within 15 km distance from the fault segment in consideration (Tormann et al., 2014). Sorting the earthquakes based on the occurrence time, a moving window containing n number of events, which moves one event at a time is used. The continuous moving window

method used here minimizes the dependence of estimated *b*-value on the starting event (Tormann et al., 2013). The estimated *b*-value in each window is displayed at the time of last event in that window. The optimum size of this moving window is estimated through a Monte Carlo search algorithm to be larger than 160 events (Khoshmanesh & Shirzaei, 2018a). The preferred *b*-value time series (Figure 5.11) is estimated using window size of 160 events, which yields a sampling rate of roughly half a year. However, our sensitivity analysis shows that the overall pattern of *b*-value time series remains constant by changing the window size up to 200 events (Figure F.1).

For the Japan Meteorological Agency (JMA) seismic catalogue, the estimated completeness magnitude (M_c) for the area considered in this study is ranging between 2.0 to 3.0 (Tormann et al., 2015). Moreover, the completeness magnitude is estimated for each moving window using an approach suggested by Woessner and Wiemer (2005) based on M_c by *b*-value stability method (Cao & Gao, 2002). Through this method, the M_c is estimated as a function of cutoff magnitudes M_{co} = 2.0, 2.1, …, 3.5, and the optimum M_c is defined as the smallest magnitude at which $\Delta b = |b_m - b| \leq \sigma_b$. In this equation, σ_b is estimated using equation (4.6), and b_m is the mean of estimated *b*-values as function of cutoff magnitude: $b_m = \sum_{M_{co}=2.0}^{3.5} b(M_{co})/n$, where n = 16 is the number of tested M_{co}. The results (Figure F.3) show that M_c is varying between 2 to 3 during study period. The preferred *b*-value time series (Figure 5.9) is estimated considering M_c = 2.0, which yields the smallest temporal window possible (~6 months), containing 160 events. However, to ensure that the choice of M_c does not affect our estimated *b*-value time series, we tested the M_c = 2.5 and 3.0. The results (Figure F.2) show that while the size of temporal window changes up to ~1 and ~2 years for the M_c

= 2.5 and 3.0, respectively, the general temporal pattern of *b*-value time series remain unchanged.

For the extended *b*-value analysis, completeness magnitude for moving window containing 250 events M_w 2+ is estimated through Goodness-of-Fit (GFT) method (Wiemer & Wyss, 2002). Through this method, the *b*-value is first estimated as a function of minimum magnitude M_i, which changes between 2.0 to 4.0 with increments of 0.1, for the events larger than M_i. Using the estimated *b*-value and M_i, a synthetic distribution representing a perfect fit to a power law is computed. Next, the absolute difference between the number of events in each magnitude bin of the observed and the synthetic distribution is estimated through:

$$R(b, M_i) = 100 - \left(\frac{\sum_{M_i}^{M_{\max}} |O_i - S_i|}{\sum O_i} \times 100 \right) \tag{5.4}$$

where O_i and S_i are the observed and synthetic cumulative number of events in each magnitude bin. The smallest M_i that results in $R > 90\%$ is chosen as the M_c of that moving window. Only the moving windows with 150 events larger than estimated M_c through GFT method are shown in the extended *b*-value time series (Figure 5.13).

5.3. Results

5.3.1. Interseismic Creep Distribution

The two-step inversion scheme (Khoshmanesh et al., 2015; Shirzaei & Bürgmann, 2013), discussed in section 2.1.2 (Khoshmanesh et al., 2015) is used to estimate the daily distribution of creep on the NJSZ. The optimum model of daily creep on NJSZ fits the GPS dataset well (Figure 5.3), with the daily RMSE for the whole time series lying between ± 0.15 cm, for both the north and east components (Figure 5.4). The estimated long-term creep rate shows a heterogenous pattern, reaching up to 8 cm/year (Figure 5.3). The area that hosted the

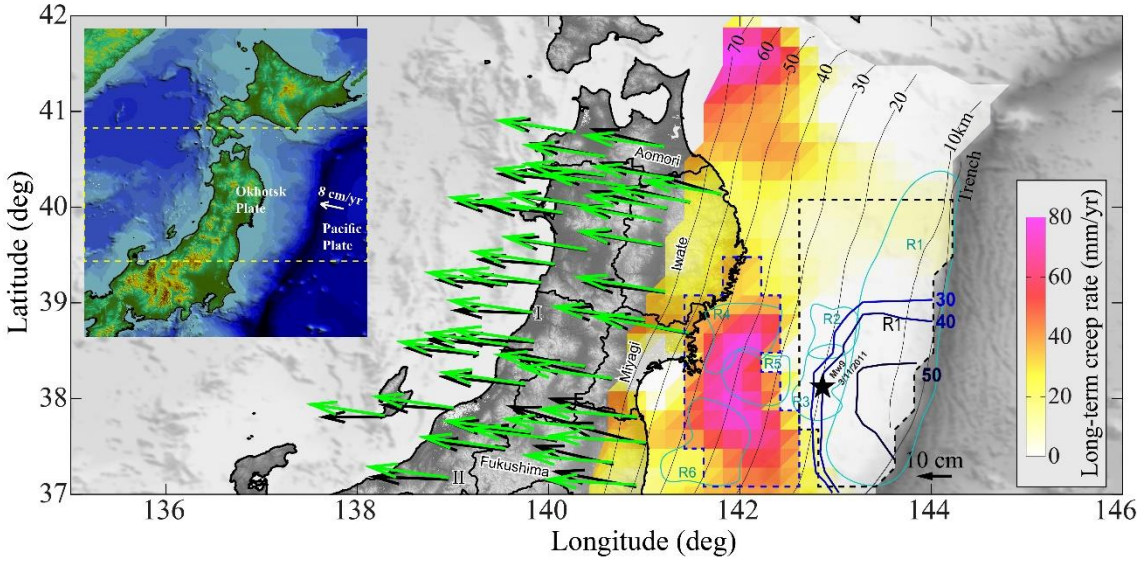

Figure 5.3. The long-term interseismic creep rate for each patch on the mesh, calculated from the optimum time-dependent creep model. The fit of this model to the 41 GPS stations (black arrows) is shown by the green arrows. The dark blue contours represent the large-coseismic-area of the Tohoku earthquakes based on the model from Shirzaei et al. (2014). The dashed blue and black boxes show the area of down-dip fast creeping segment and the shallow locked segment discussed in the text, respectively. The thin black lines show the depth contour lines on the subducting slab. The rupture areas of historic earthquakes are plotted in cyan contours (Shibazaki et al., 2011). R1: 1611 M_w 8.1; R1: 18 January 1981 M_w 7.1; R3: 31 October 2003 M_w 6.8; R4: 12 June 1978 M_w 7.8; R5: 1936 M_w 7.4; R6: 1938 M_w 7.3. Inset: A map showing the location and tectonic setting of Japan. The northeast Japan subduction zone located within the yellow dashed box (between 37° - 41° latitude) is the considered study area.

large-coseismic-slip of 2011 Tohoku earthquake is resolved as a locked segment located within ~37° to 39.5° latitude and depths shallower than ~30 km in the derived model (inside the black dashed box in Figure 5.3). This locked segment is juxtaposed with a deeper fast creeping segment that aseismically slips by an average rate up to 8 cm/year throughout the interseismic period (blue dashed box in Figure 5.3). Most of the afterslip due to the 2011 Tohoku earthquake was accommodated by this down-dip creeping segment (Shirzaei et al., 2014). Another smaller creeping segment is located in the north of considered study area, off the northeastern coast of Aomori Prefecture, at depth greater than 50 km. The up-dip area of this northern creeping segment shows almost no creep during interseismic period, but later hosted postseismic slip due to the 2003 M_w 8.3 earthquake (Miyazaki & Larson, 2008).

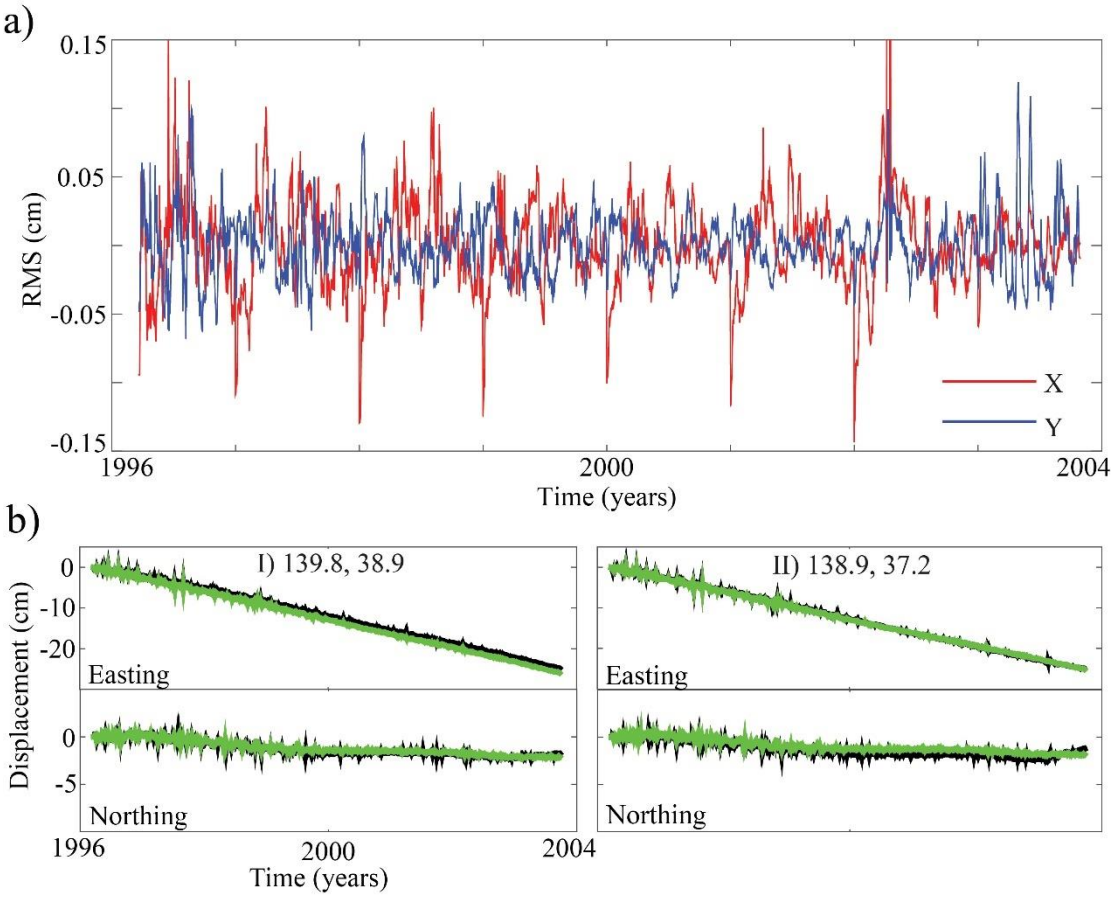

Figure 5.4. uncertainty of GPS observations. (a) The root-mean-square error (RMSE) for the entire GPS time series of all 41 stations, both the east (red) and north (blue) components. (b) GPS (black) and modeled (green) time series for two GPS station, their locations are shown in Figure 5.3. The east and north components are shown in the top and bottom panels, respectively.

5.3.2. Model Resolution

The resolution of the optimum model is calculated in the form of creep standard deviation, including the improvement in resolution when CREs are used as bounds in the time-dependent inversion, following Weston and Shirzaei (2016). For an inversion using just GPS data the model resolution decreases moving toward the trench (Figure 5.5a). The addition of CRE data leads to a reduction in the creep standard deviation, particularly for patches near the trench (Figure 5.5b), and across the plate interface there is a substantial improvement in

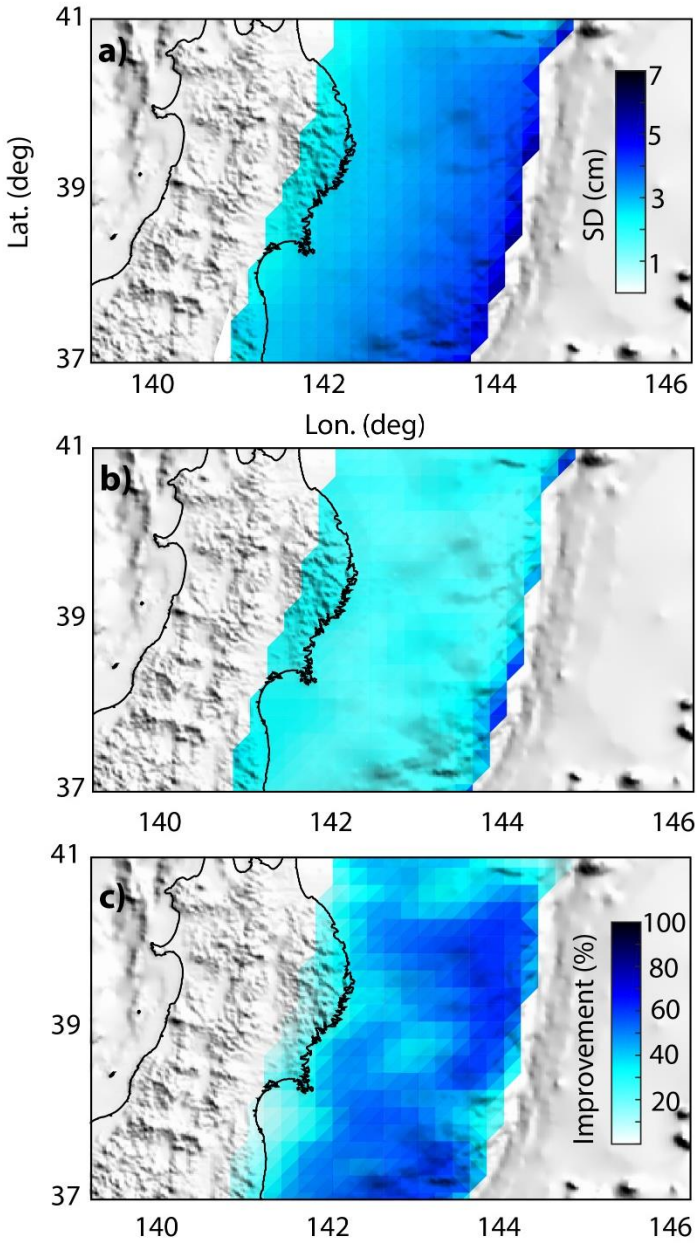

Figure 5.5. Creep model resolution in terms of the standard deviation (SD). (a) For a model from an inversion using only GPS data. (b) SD for an inversion combining GPS and CRE data. (c) Percentage improvement in the model resolution when the CRE data are added to the GPS data.

the model resolution (40-70%, Figure 5.5b). This test highlights the importance of CREs and the complementary nature of seismology and geodesy to understand subduction processes.

5.3.3. Multiscale Creep Rate Variations

To investigate the non-linear changes of creep rate on the NJSZ, the spatiotemporal distribution of constant long-term acceleration is evaluated by fitting a quadratic function to the time series of creep at each fault mesh patch (Khoshmanesh & Shirzaei, 2018b; Mavrommatis et al., 2015). The result shows that, with exception of the shallow locked zones and several decelerating patches located within the down-dip creeping zone, the rest of the

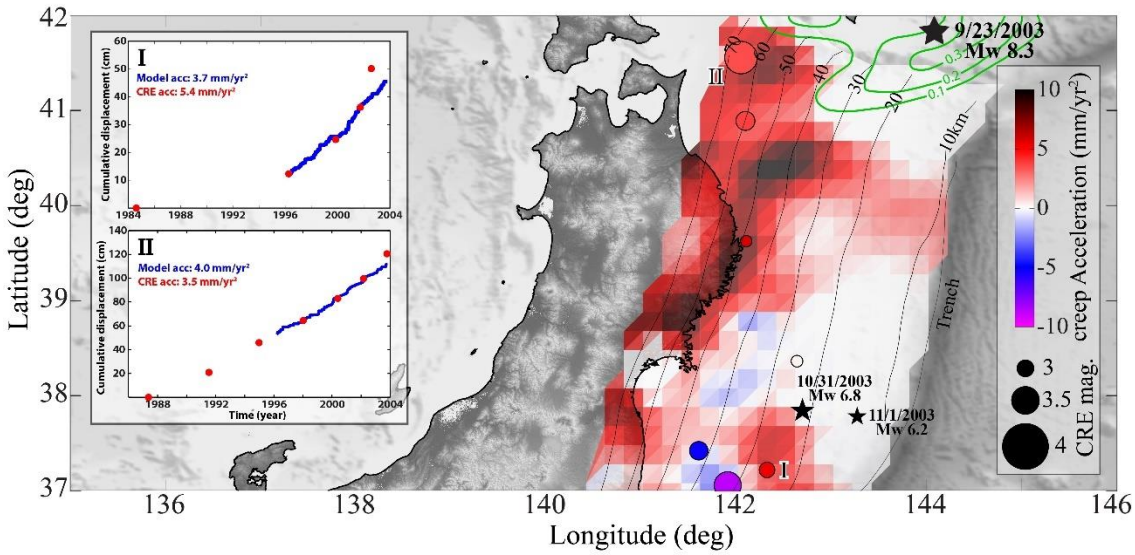

Figure 5.6. Estimated long-term constant acceleration for the estimated time series of creep on the NJSZ. The solid circles show the location of CRE sequences that pass the Mann-Kendal test at 95% confidence, color-coded based on the estimated constant acceleration for the sequence. Stars show the locations of 2003 Mw8.3 Tokachi-oki earthquake, and two Mw6+ that occurred in 2003. Green controur lines shows the modeled postseismic slip caused by the Mw8.3 earthquake. The inset shows the comparison between times series of two of the CRE sequences (red dots) that show non-linear behavior and the daily time series of modeled creep (blue curve) on their closest fault patch.

megathrust has been accelerating up to 1 cm/year^2 during the interseismic period. The constant acceleration is also estimated for the cumulative creep time series obtained for the CRE sequences that pass the Mann-Kendall statistical test at 95% confidence level (Gilbert, 1987), indicating that their repeat time is characterized by a monotonic trend (Khoshmanesh & Shirzaei, 2018b). The estimated CRE accelerations confirm the spatiotemporal distribution

of the modeled long-term acceleration (Figure 5.6). Moreover, comparing the time series of investigated CRE sequences with that of modeled creep on their nearest fault patch shows that non-linear temporal variation agrees between the two datasets (inset in Figure 5.6). The results indicate a major accelerating zone in depths deeper than ~30 km from 39° northward, perhaps imparting stress on the adjacent locked section that later ruptured through the M_w 8.3 Tokachi-Oki earthquake in 2003 (Figure 5.6) (Khoshmanesh & Shirzaei, 2018b; Mavrommatis et al., 2015).

The creep along the NJSZ in window sizes of 6 months shows that the amount of aseismic slip is also changing in shorter timescales (Figure 5.7), especially on the two main down-dip fast creeping segments. This suggests that aseismic slip on the subducting slab is not steady in time, and instead evolves as a series of SSEs. To better show the creep rate variation in time, the creep within the large down-dip creeping segment (blue dashed box in Figure 5.3) is averaged, showing that SSEs occur with an almost annual period in this segment (Figure 5.8). Seismic activity in this deeper portion, where most of the SSEs occur, seems to be spatially clustered within the periphery of the SSE zones (Figure 5.7). This shows that SSEs occur in between locked patches, which rupture due to shear stress concentration at the edge of SSE area.

5.4. Discussion

5.4.1. SSEs Interactions with Seismicity in Neighboring Segment

To further investigate the implication of detected deep SSEs in seismic hazards associated with the NJSZ, the time series of resulting Coulomb failure stress on the neighboring shallow locked patches, between 37° to 40°, that have a long-term rate of less than 1 cm/year (black dashed box in Figure 5.3) is estimated. This locked segment later

accommodated the large-coseismic-slip during the 2011 Tohoku earthquake (Figure 5.3). the Coulomb failure stress represents the combined effect of change in shear ($\Delta\tau$) and normal stress ($\Delta\sigma$) due to creep rate variation, estimated using the relationship $\Delta C = \Delta\tau - \mu\Delta\sigma$, in

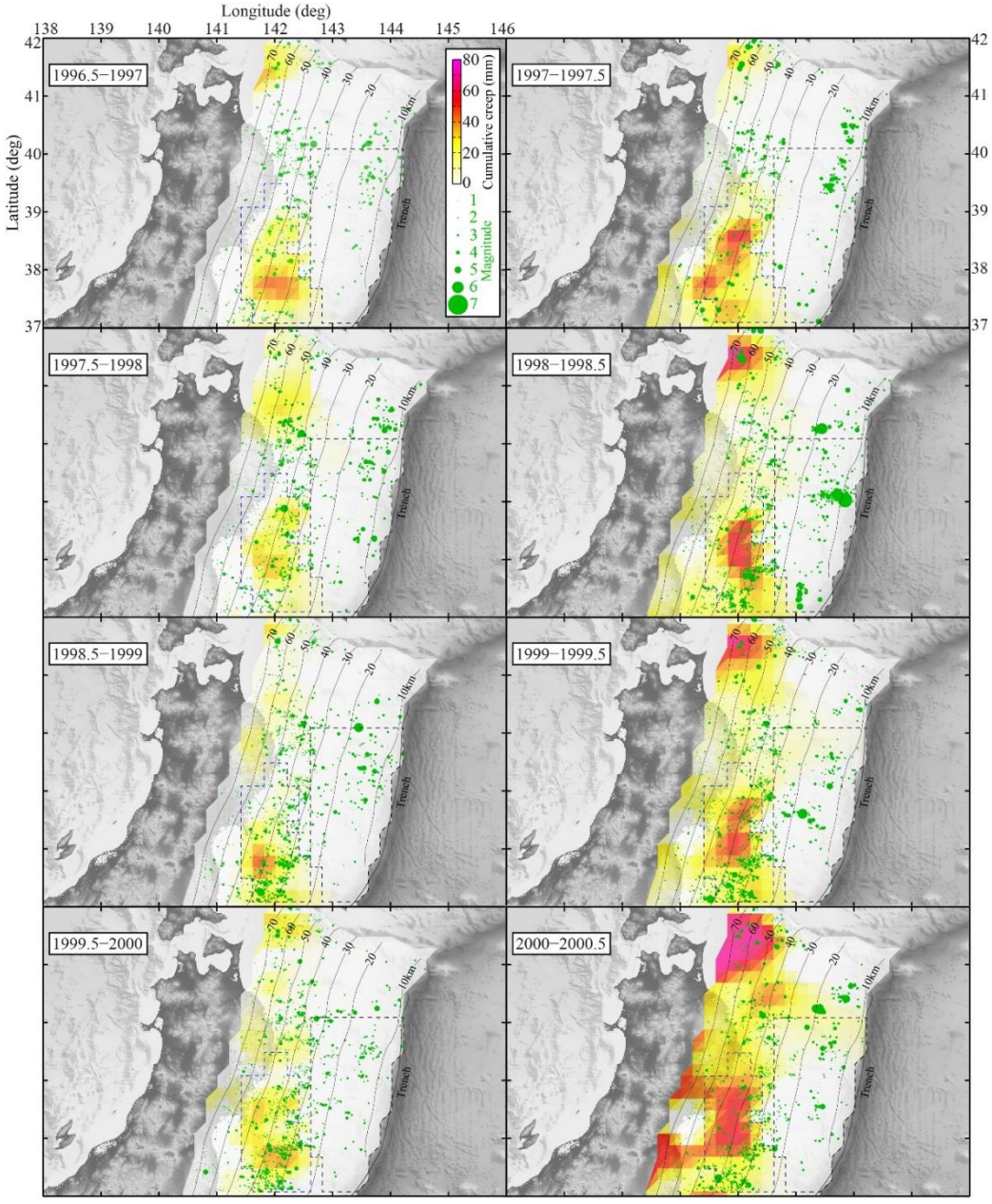

Figure 5.7. Creep in window sizes of 6 months between 1996.5 and 2003.5. The green dots show the location of seismicity within ± 15 km distance from the subducting plate. Size of dots represents the moment magnitude of associated seismic event.

which $\mu = 0.6$ is the friction coefficient. The results show that exerted Coulomb stress in this locked segment periodically increases with an almost annual repeat time (Figure 5.9). The number of seismic events within a ±15 km distance of this locked segment shows a positive correlation with the time variation of Coulomb stress (Figure 5.10). Also, the time series of total seismic moment released (green curve in Figure 5.9) has a similar temporal behavior to that of the Coulomb stress and number of earthquakes, suggesting a causal relationship between the down-dip SSEs and increase in the seismic activity in this neighboring shallow

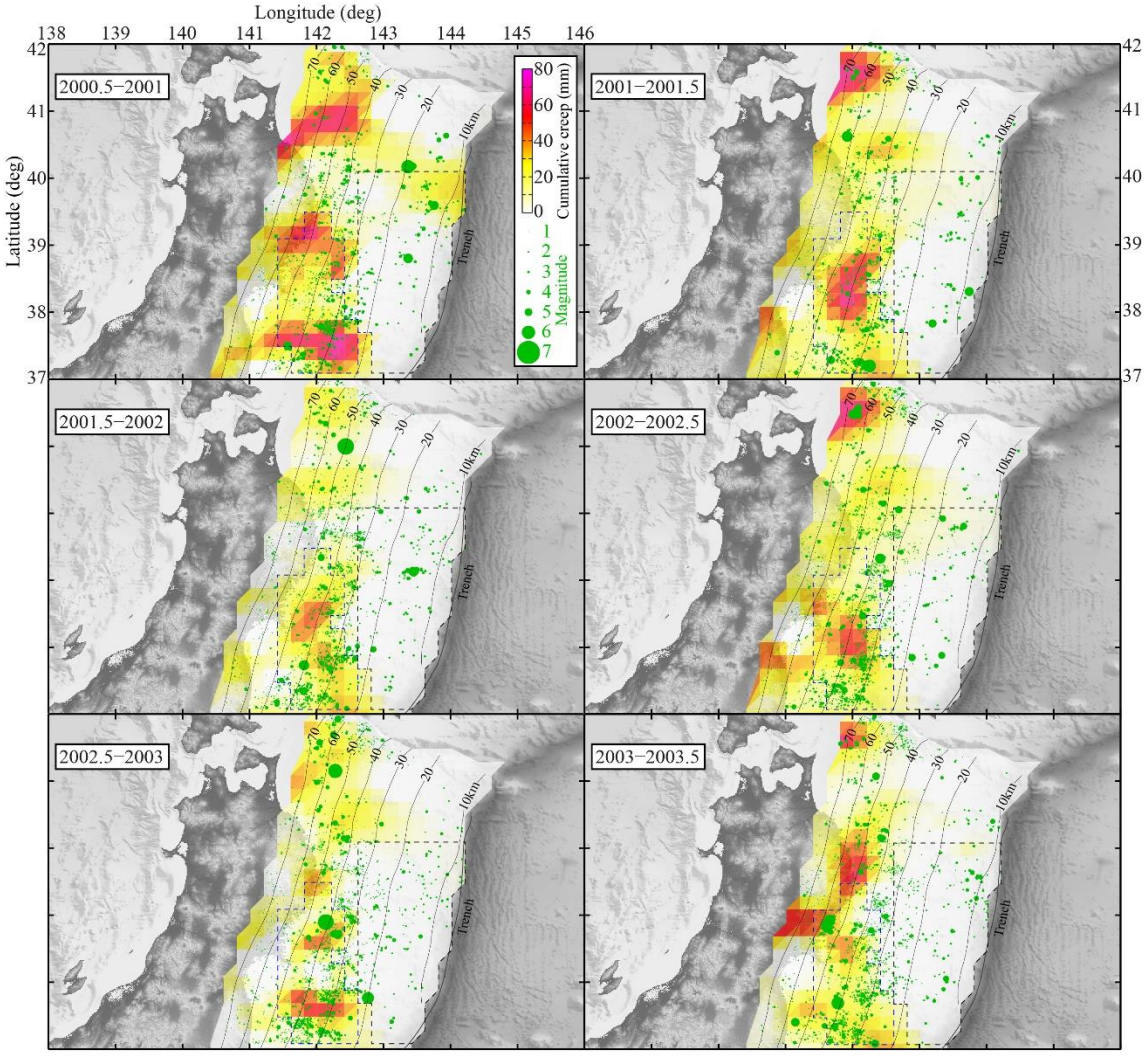

Figure 5.7 continued

locked segment. Moreover, all the M_w 5+ earthquakes within ±15 km distance of this segment during 1996 - 2003 occurred during the increasing or peak Coulomb stress (Figure 5.9). This might be the reason for the positive correlation between Coulomb stress and total seismic moment

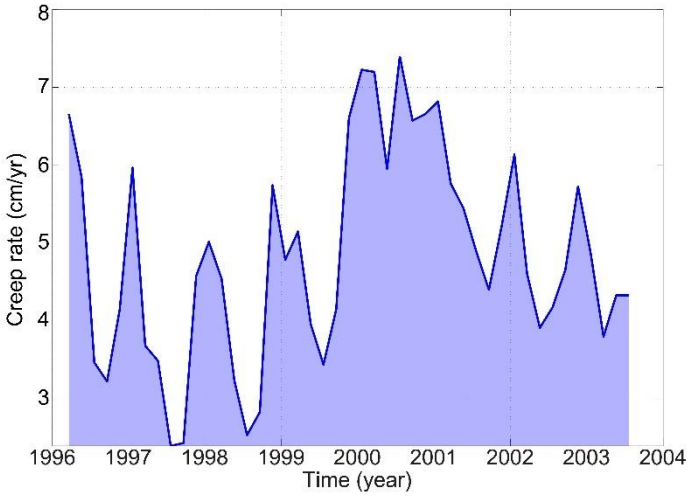

Figure 5.8. Time series of average creep rate within the down-dip creeping segment, indicated using the dashed blue box in Figure 5.3. The creep rate is estimated using cumulative creep in moving window of size 3 month and step size of 2 months. The creep rate is displayed at the beginning of each time window.

release, with the latter being mostly controlled by relatively larger seismic events (Figure 5.9). This is compatible with the increased imparted shear stress on the shallow locked segment (blue curve in Figure 5.11) during the SSEs, quantified through Coulomb stress elevation.

To gain a more accurate insight in the interactions between SSEs and seismicity on the shallow locked segment, the continuous time series of Gutenberg-Richter *b*-value (Gutenberg & Richter, 1944) is also evaluated using the seismic record within ±15 km distance of this segment (section 5.2.2). The Gutenberg-Richter *b*-value implies that earthquake magnitudes follow a power-law, which indicate that seismic events with different size occur on the fault segment in consideration, consistent with the seismic record associated with NJSZ (Figure 5.7). The *b*-value time series shows the temporal evolution of the ratio of smaller to larger

earthquakes, which is inversely related to the effective normal stress on the fault (Khoshmanesh & Shirzaei, 2018b; Schorlemmer et al., 2005; Tormann et al., 2013). The estimated *b*-value time series (magenta curve in Figure 5.9) shows an agreement with the Coulomb stress change with a correlation coefficient of 75%, implying that SSEs are

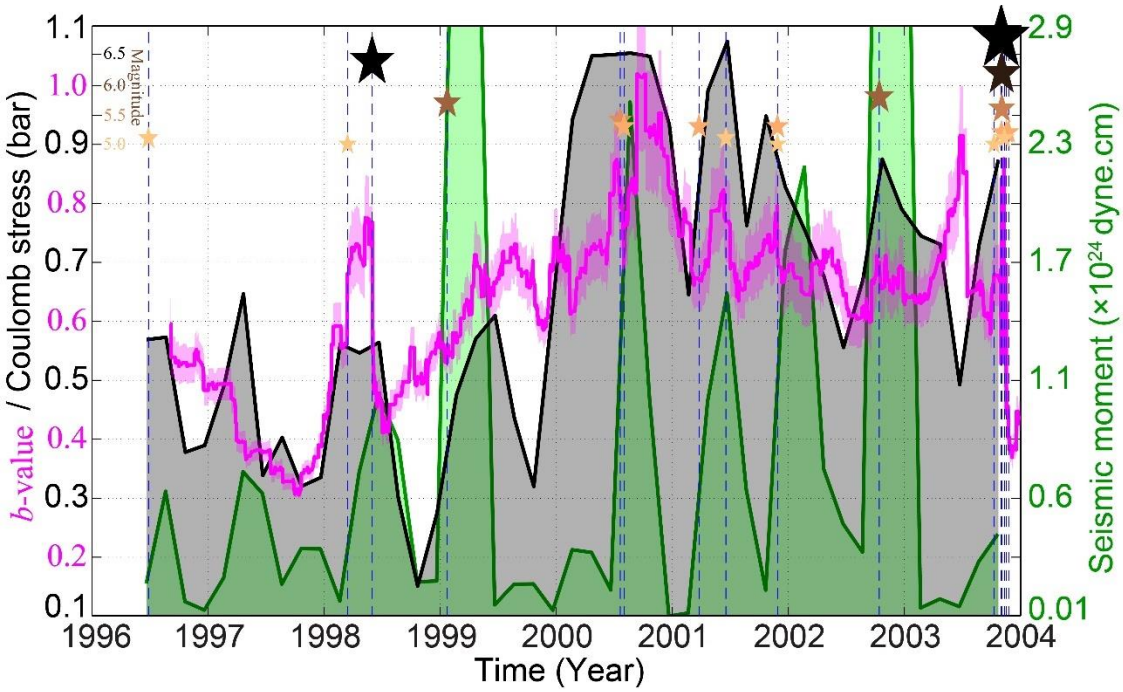

Figure 5.9. Coulomb stress and seismicity. Time series of Coulomb stress (black curve) on the shallow locked segment (inside the black dashed box in Figure 5.3), total seismic moment release (green curve) and *b*-value time series (magenta curve) for earthquakes within ± 15 km distance of subducting plate. Stars and vertical dashed blue lines show the magnitude and timing of M_w 5+ earthquakes within the shallow locked segment.

accompanied by an increase in the proportion of smaller earthquakes in their up-dip locked region. This is perhaps caused by the relaxation of confining normal stress on the locked segment during the elevated Coulomb stress due to the down-dip SSEs (Figure 5.11), consistent with the opposite relation between *b*-value and effective normal stress on the fault. Elevation of the proportion of smaller (larger) earthquakes, increasing (decreasing) the *b*-value, is related to reduction (increase) of the real contact area, which in turn is associated with effective normal stress decline (incline) (Archard, 1957; Yoshioka, 1997). Increase in the

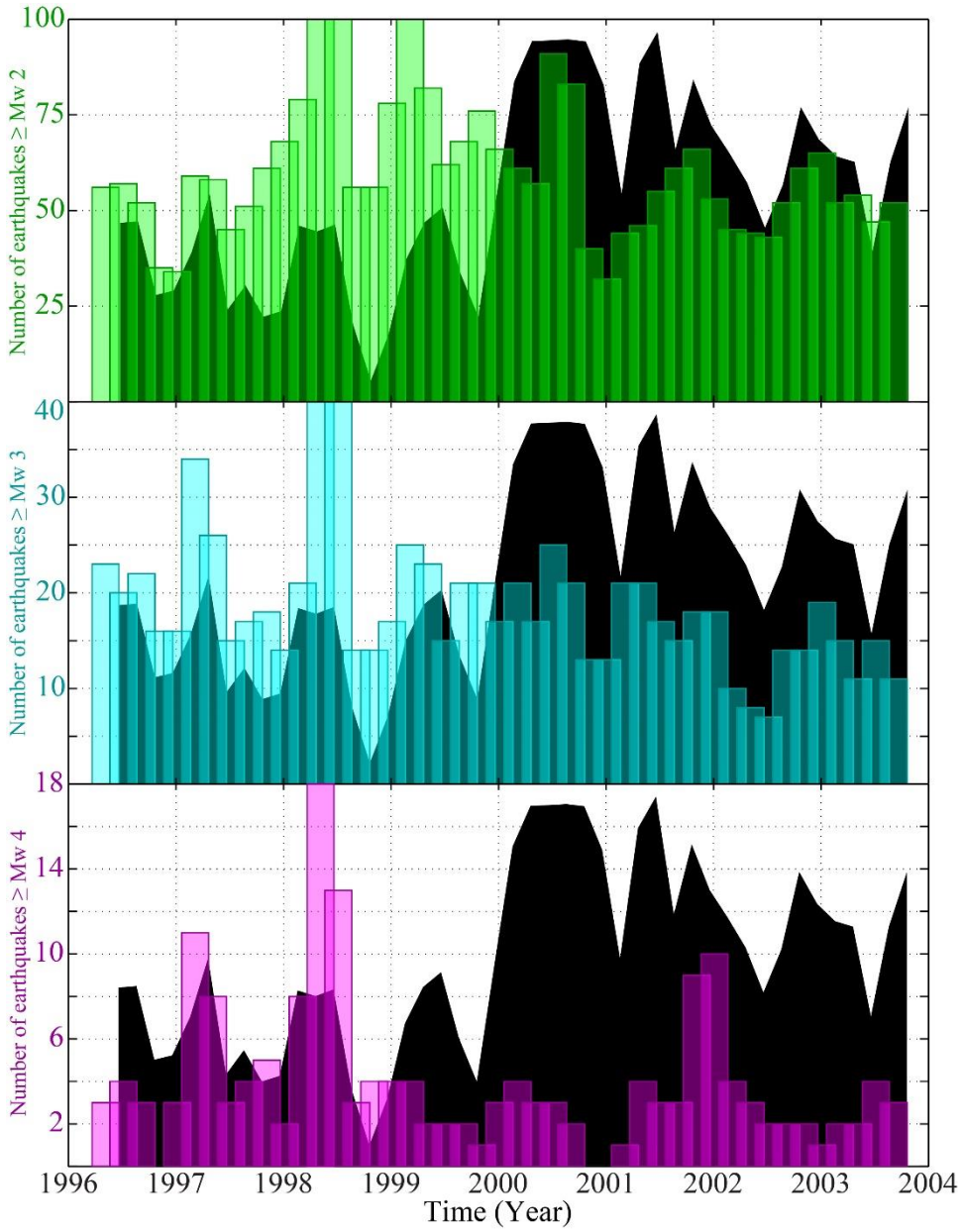

Figure 5.10. Time series of number of earthquakes above M_w 2.0 (green histogram in top panel), above M_w 3.0 (cyan histogram in middle panel), and above M_w 4.0 (magenta histogram in bottom panel) on the shallow locked segment. A temporal moving window of size 3 months and step size of 2 months is used. The background black curve shows the Coulomb stress on the shallow locked segment, as shown in Figure 5.9.

proportion of smaller earthquakes, however, seems inconsistent with the observed elevation of seismic moment release and increase in the possibility of M_w 5+ earthquakes during elevated Coulomb stress caused by SSEs. This requires an explanation regarding the interaction

between small and large earthquakes, which roots in the mechanical structure of the megathrust.

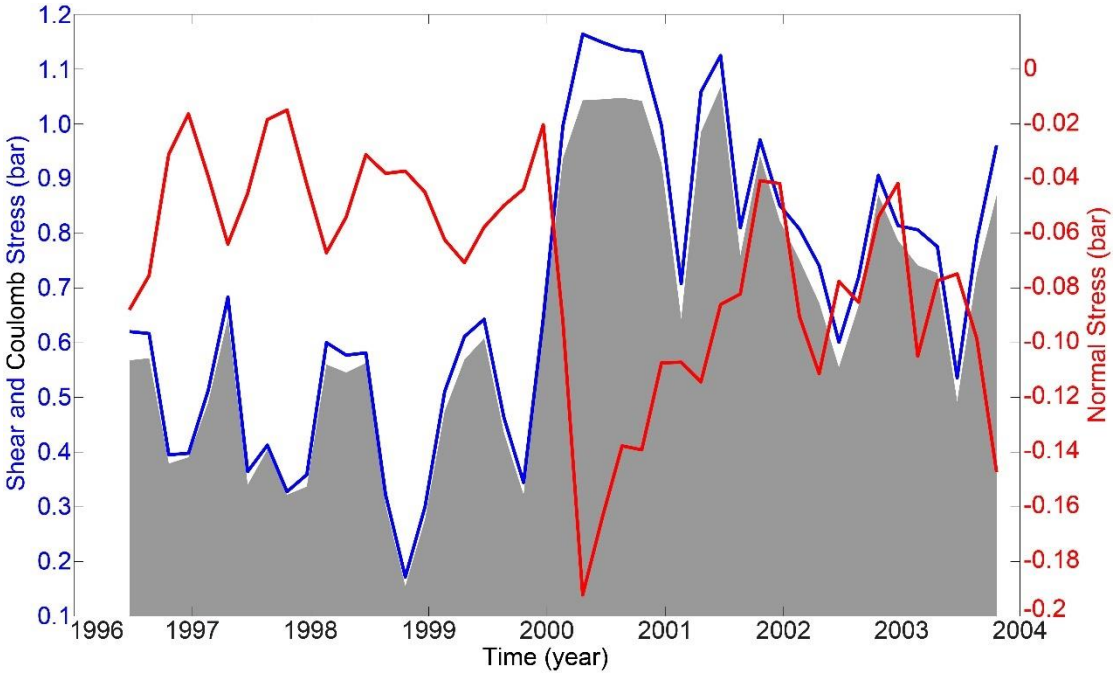

Figure 5.11. Imparted shear and normal stress on the shallow locked segment, shown respectively with blue and red curve, estimated in moving window of size 3 months and step size of 2 months. The gray curve shows the Coulomb stress time series as shown in Figure 5.9.

5.4.2. Microstructure of Megathrust

To explain the seemingly conflicting observations obtained here, we suggest that the megathrust might be paved with individual asperities, namely localized high frictional strength (competent) contact areas of different size that are capable of earthquake generation. These asperities are embedded in the low strength (incompetent) creeping area, which act as seismic barriers (Lay et al., 1982; Scholz & Engelder, 1976). This idea is supported by field observations of exhumed subduction zones, which suggest that isolated clusters of competent material of different scales are embedded within incompetent gouge matrix, forming a mélange of variable frictional strength (Bebout & Barton, 2002; Fagereng, 2011; Fagereng & Sibson,

2010; Meneghini et al., 2010). Moreover, radiated high frequency seismic waves recorded during 2011 Tohoku earthquake are also suggested to be associated with heterogenous rheology of fault material (Meng et al., 2011). In such a frictionally heterogenous structure, elevation of imparted shear stress during the deep SSEs is accommodated by isolated failure of smaller asperities on the up-dip locked segment, which hinders the accumulation of stress on bigger asperities (Lay et al., 1982). This explains the observed increase in the number of small earthquakes in the shallow locked segment during the deeper SSEs. The efficient interaction between these microearthquakes on small asperities, in turn, generates enough stress perturbation through a "domino effect" and eventually leads to rupture on the bigger asperities which results in larger seismic events (Konca et al., 2008; Lay et al., 1982). Alternatively, the rupture on small asperities could grow laterally and join other concurrent small events to rupture as one larger seismic patch, producing a larger earthquake (Corbi et al., 2017; Dublanchet et al., 2013).

To further support this hypothesis of domino effect as the cause of large seismic events, the *b*-value analysis is extended to 2011, for the area within 10 m contour line of coseismic slip of 2011 Tohoku earthquake (Figure 5.12) suggested by Shirzaei et al. (2014). The resulting time series shows that prior to the majority of M_w 6+ earthquakes, the *b*-value has an increasing trend (Figure 5.13). This means that the number of small earthquakes increases through time, until a major earthquake hits, perhaps due to the efficient interaction of small events and their resulting stress perturbation. There are, however, two exceptions, one in 2008 and the other one in 2011 prior to the Tohoku earthquake. In both cases the b-value shows a decreasing trend for several months after the previous M_w 6+ seismic events. Following the M_w 6.3 event on 10 August 2010 (Figure 5.12), the b-value decreases for ~ 6 months until the 2011 earthquake hits. This behavior may be a consequence of relative

decrease in the number of small earthquakes, suggesting a seismic quiescence prior to this megathrust event. In other words, the stressed small asperities remain intact and are spatially connected to nearby large asperities to form large enough locked segments, priming the megathrust for the great earthquake. A perturbation in stress field, possibly due to SSE on the locked segment (Kato et al., 2012), and simultaneous failure of larger seismic asperities (Corbi et al., 2017; Yabe & Ide, 2017) might have led to the M_w 9.0 event. Such mechanism is also consistent with the resolved rupture dynamics of the Tohoku event, starting in the center and

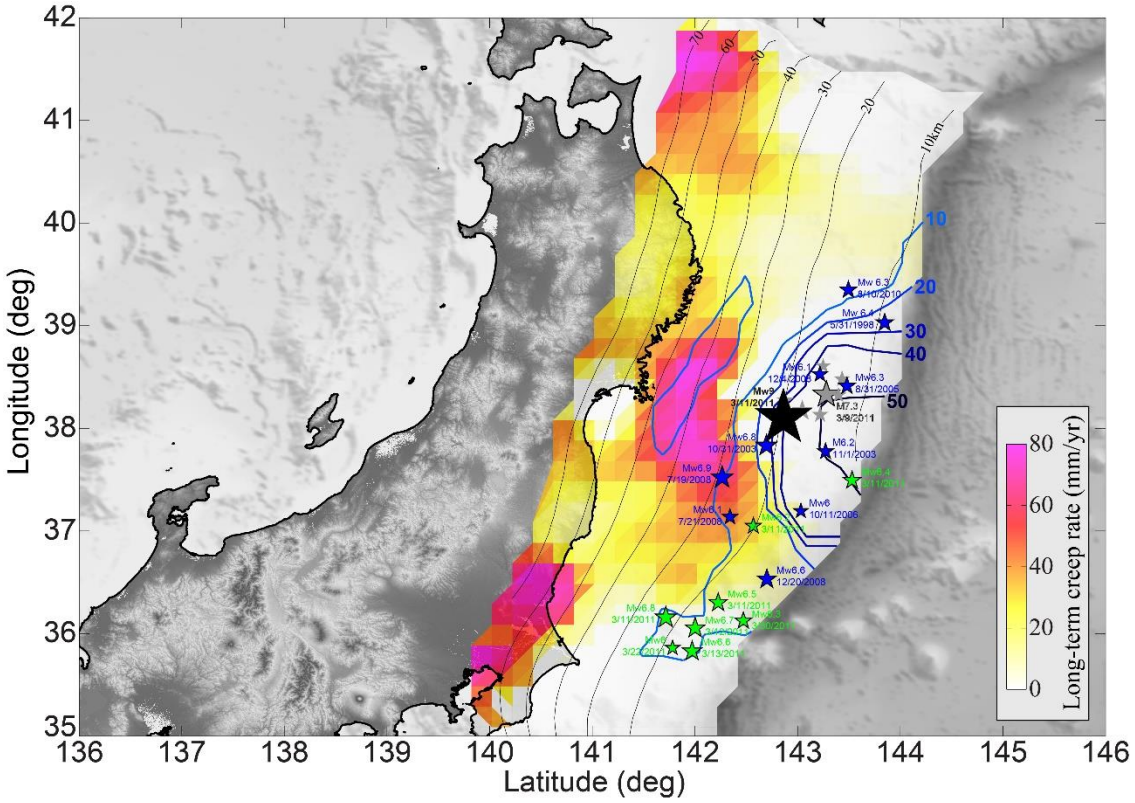

Figure 5.12. Interseismic creep rate along the entire fault, along with the blue contour lines showing the coseismic slip of the 2011 M_w 9.0 Tohoku earthquake. The location, timing, and magnitude of earthquakes above M_w 6.0 inside the 10 m coseismic slip area is shown using the solid stars. Earthquakes that occurred prior the foreshocks of M_w 9.0 earthquake are shown using blue stars. Gray and green stars show the M_w 6+ foreshocks and aftershocks of the 2011 M_w 9.0 earthquake.

propagating to the isolated asperities in southern and northern segments (Lee et al., 2011; Meng et al., 2011).

The decreasing *b*-value trend in 2008 initiated following the M_w 6.9 event on 19th July 2008 and terminated by occurrence of M_w 6.1 and M_w 6.6 events in December of the same year (Figure 5.12). Similar to the 2011 Tohoku earthquake, the hypocenter of the M_w 6.9 event in 2008 is located on the transition zone between shallow locked segment and the down-dip creeping segment. Also, interestingly, the two M_w 6+ December events occurred ~5 months later, on the northern and southern asperities. The 2008 events, therefore might provide an

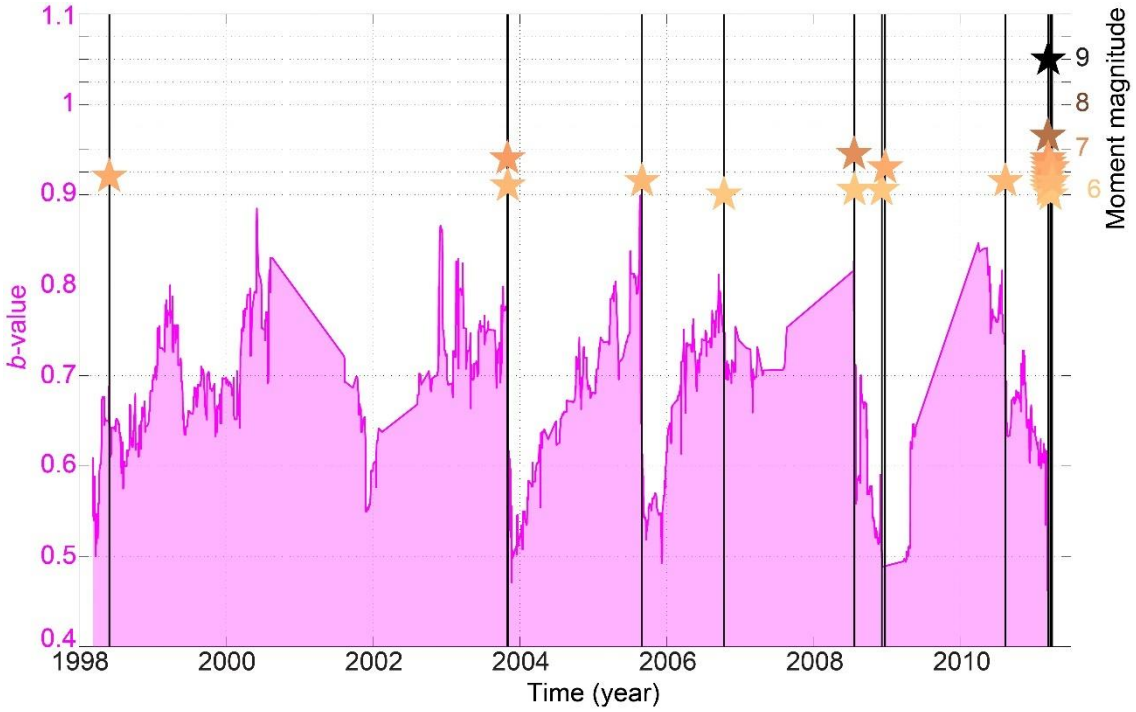

Figure 5.13. Gutenberg-Richter b-value time series during 1996 - 2011 for earthquakes within ± 15 km distance of the area within 10 m coseismic rupture of 2011 Tohoku earthquake. Stars and vertical black lines show the magnitude and timing of M_w6+ earthquakes.

example of unsynchronized failure on spatiotemporally separate asperities that later ruptured together during the 2011 Tohoku earthquake. In 2008, the intervening creeping area acted as a barrier to seismic rupture, whereas it failed to stop the rupture in 2011. This suggest that the seismic asperities and barriers are not permanent features, but instead their size and space is variable within the megathrust depending on the slip and stress history (Konca et al., 2008).

5.4.3. Hypothetical Model Based on Rate-and-State Law

To further elaborate on the suggested mechanical structure of megathrust, here a hypothetical model of a frictionally heterogenous fault according to the rate-and-state friction law (Dieterich, 1979; Ruina, 1983) is provided. Based on the Amonton-Coulomb friction, fault slip occurs when the fault frictional strength, governed by the product of confining pressure and inherent frictional strength of material, is overcome by shearing stress (Segall, 2010). The mode of slip, being either stable or unstable, on the other hand, depends on the frictional stability, which is determined by frictional properties of fault material and environmental conditions. In the framework of rate-and-state friction law, frictional stability is quantified using critical stiffness estimated through $k_c = -\sigma_e(a-b)/D_c$, in which, D_c is the critical slip distance, (*a-b*) is a combined parameter, and σ_e is the effective normal stress, estimated as subtraction of pore pressure from confining normal pressure (Scholz, 1998). The (*a-b*) parameter determines the change of friction coefficient in response to loading rate variations. A negative (*a-b*), known as velocity-weakening (VW) properties, is required for frictionally unstable regime, corresponding to the seismogenic asperities (Chen & Lapusta, 2009; Dublanchet et al., 2013; Ide & Aochi, 2005; Noda & Lapusta, 2013). Whereas, the creeping matrix of the fault is characterized by velocity-strengthening (VS) or weak VW properties, indicated with positive or small negative (*a-b*), respectively (Scholz, 1998). In case of VS, resulting in negative k_c, the matrix is stably creeping in absence of external stress perturbation, and is also capable of hosting aseismic transient slip through either SSEs or afterslip, if subject to stress perturbation caused by, e.g. nearby earthquakes or transient pore fluid pressure elevation. (Khoshmanesh & Shirzaei, 2018a; Perfettini & Ampuero, 2008). A small negative (*a-b*) in combination with elevated fluid pressure, on the other hand, results in a small positive k_c, which is also suggested as a favorable condition for SSE (Leeman et al., 2016; Liu & Rice,

2007). The condition required for aseismic transients is also met if the (*a-b*) of background matrix has a slip-rate-dependence behavior, being less VW (Kaproth & Marone, 2013; Shibazaki & Iio, 2003) or VS (Fukuda et al., 2013; Sawai et al., 2017) with increasing slip rate. Therefore, Both SSEs and regular earthquakes can coexist on such a frictionally heterogeneous fault, depending on the spatial density of VW asperities and frictional properties of the creeping barrier (Corbi et al., 2017; Dublanchet et al., 2013; Nakata & Snieder, 2011; Noda & Lapusta, 2013; Yabe & Ide, 2017).

Additional frictional heterogeneity might be caused by the inhomogeneous distribution of effective normal stress and critical slip distance (D_c). Since the fault is held together at the isolated contact points, most of the normal stress on the fault is accommodated through asperities, which increases their critical stiffness and promotes their instability through dynamic rupture. Heterogeneous distribution of pore pressure, caused by different compressibility and permeability of VS gouge matrix compared to the competent VW asperities might further contribute to the frictional heterogeneity of the fault, by changing k_c. Furthermore, D_c, which is the distance that the fault is needed to slip, upon a velocity perturbation, to establish a new set of contact points (Dieterich, 1979), is a geometrical property that depends on fault roughness (Okubo & Dieterich, 1984; Scholz, 1988), gouge layer thickness (Marone & Kilgore, 1993), and confining pressure (Scuderi & Collettini, 2016). Therefore, the frictional heterogeneity on the NJSZ might also stem from geometrical irregularities, which is controlled by the topography of downgoing plate and thickness of subducting trench sediments (Heuret et al., 2012; Tanioka et al., 1997).

CHAPTER 6.

CONCLUSIONS AND SUMMARY

6.1. Central San Andreas Fault

Fault creep, a mechanism through which the accumulated strain on the fault is released aseismically, is a prominent factor in earthquake cycle. Spatial distribution of creep is used to pinpoint the location of locked asperities, which are susceptible to rupture in large earthquakes. In CHAPTER 2, a spatiotemporal map of the interseismic creep distribution is obtained for the Central San Andreas Fault (CSAF). To this end, a two-step time-dependent modeling scheme consisting of iterated least squares and linear Kalman filter is applied to invert the time series of surface deformation data obtained using InSAR for the creep on the CSAF. The creep obtained using observations of small characteristically repeating earthquake (CRE) sequences along the CSAF is used to constrain the creep model. The obtained optimum time-dependent creep model reveals that the 30 km central segment of the CSAF is creeping with the rate of up to 32 mm/year, yet slower than the long-term rate of 34.5 mm/year. The creep rate tapers off towards the neighboring transition zone to the northwest and southeast of the CSAF. Another noticeable feature of the obtained time-dependent creep model is the afterslip triggered by the 2004 Parkfield earthquake in the southeast part of the CSAF.

The time-dependent model is further used to investigate the creep rate variations along the CSAF. The results indicate that the short-term creep rate varies along the CSAF, especially in the central 70 km section. The short-term creep rate oscillates around the long-term rate in a quasi-periodic manner, which resembles accelerating and decelerating pulses of creep in slow slip events (SSEs). The short-term geodetic moment accumulation rate also varies up to 30% compared to the long-term moment accumulation rate. The time-dependent creep model is

also used to refine the coefficient of the CRE creep scaling relation. A better fit between CRE creep and the time-dependent creep model is obtained across the CSAF, using the re-estimated coefficients $\alpha = -1.53 \pm 0.37$ and $\beta = 0.10 \pm 0.02$. The presented data, model, and interpretations improve our understanding of the time-dependent seismic hazards along San Andreas Fault.

The observation of fault-related surface deformations measured by radar interferometry are extended back to 1992 in CHAPTER 3 to study the kinematics of CSAF across two decades. The obtained time-dependent model of creep during 1992 – 2010 shows that creep rate on the CSAF is changing in short- and medium-term time scales. The decadal scale changes in creep rate is quantified using a constant creep acceleration. Results reveal a strike- and depth-dependent distribution of accelerating and decelerating patches along the fault, which may mark areas subject to decadal increase or decrease in pore fluid pressure, separated by low permeability barriers. Most noticeably, I show that Parkfield transition zone was accelerating prior to the 2004 M_w 6.0 Earthquake, which ruptured the locked segment adjacent to the fault.

The short-term evolution of creep along the CSAF is further investigated using near-field surface deformation observations during 1992 – 2010 through a statistical approach. The results suggest that evolution of aseismic slip on CSAF includes periods of slow creep, i.e., below the long-term average, followed by episodes of fast creep, where the creep rate exceeds the long-term average. The estimated probability distribution function (PDF) of these near-filed short-term creep rates has a non-Gaussian distribution, characterized by a power law tail for the creep rates above that of long-term. This suggest that the dynamics of aseismic slip along CSAF is governed by creep avalanches, which occur as spatially isolated clusters of velocities exceeding the long-term average rate. The statistical properties of these creep

avalanches are further investigated to obtain an insight on their underlying mechanisms. The results reveal that, similar to seismic events, creep avalanches occur at all spatial length scales. Moreover, the exponential decay in the size (in excess of long-term rate) of these avalanches suggest that pore pressure variation is the deriving mechanism of creep rate changes on CSAF. This suggestion is in alignment with the laboratory experiments and theoretical studies.

Episodic unsteady slip with limited speed in the form of SSEs is shown to occur over entire seismogenic depth of CSAF at semi-regular intervals in CHAPTER 2. These episodic SSEs might modulate the time of seismic events on nearby locked zones. The driving mechanism of these SSEs and their interaction with seismicity along the fault is investigated in CHAPTER 4 by using dense geodetic and seismic measurements and observations of CSAF fault properties at San Andreas Fault Observatory at Depth. The detailed map of near-field creep rate variations reveals that each episode of SSE results from an ensemble of localized creep avalanches that aseismically rupture isolated fault segments, separated by stable creeping patches, as discussed in CHAPTER 3. Furthermore, using a rate and state friction modeling scheme, I show that occurrence of SSEs coincides with reduction of effective normal stress due to pore pressure elevation. This finding is supported using the observations of seismicity, in particular Gutenberg-Richter b-value. I suggest that elevated pore pressure possibly driven by compaction of intergranular pore spaces and subsequent frictional dilation are responsible for initiating and arresting the episodic SSEs along the CSAF. Furthermore, I show that earthquakes larger than M_w 4.0, including the 2004 M_w 6.0 Parkfield earthquake occurred during SSEs on the CSAF. This suggests that the 2004 Parkfield quake could have been triggered due to stress transfer from an SSE on CSAF. This is supported by estimating the rate of Coulomb stress change at the hypocenter, which shows an increase up to 0.45 bar/year during the SSE.

6.2. Northeast Japan subduction zone

The interseismic evolution of creep on the northeast Japan subduction zone (NJSZ) is modeled using on-shore observation of GPS and creep inferred from CREs, in CHAPTER 5. The obtained result of long-term creep rate reveals that the shallow segment of the NJSZ was mostly locked during the interseismic period of 1996 - 2003. This resolved shallow locked segment moved up to 50 m during the 2011 M_w 9.0 Tohoku earthquake. The map of long-term rate also shows a fast creeping segment in the down-dip of the shallow locked segment. Using the estimated time series of creep, I show that creep on this deep creeping segment evolves as a series of SSEs that have an almost annual cycle. I further show that all the M_w 5+ earthquakes on the shallow locked segment occur during elevation of Coulomb stress due to these deep SSEs. Moreover, the *b*-value time series suggests that the ratio of small to large earthquake increases on the shallow locked segment during the deep SSEs. Therefore, I suggest that the shallow locked segment might be paved with individual asperities of different size that are capable of seismic rupture, embedded in the low strength creeping area, which act as seismic barriers. Therefore, an increase in shear stress caused by the down-dip SSEs is accommodated by isolated failure of smaller asperities on the up-dip locked segment, hindering the accumulation of stress on bigger asperities. The efficient interaction between these ruptures on small asperities, in turn, may cause a domino effect that generates enough stress perturbation, occasionally leading to rupture on bigger asperities that cause larger seismic events. This hypothesis is further supported by extension of *b*-value analysis to 2011, showing an increase in the ratio of small earthquakes prior to most of M_w 6+ earthquakes on the shallow locked segment.

REFERENCES

Apel, E. V., Bürgmann, R., Steblov, G., Vasilenko, N., King, R., & Prytkov, A. (2006). Independent active microplate tectonics of northeast Asia from GPS velocities and block modeling. *Geophysical Research Letters, 33*(11), L11303. doi: 10.1029/2006gl026077

Archard, J. F. (1957). Elastic deformation and the laws of friction. *Proceedings of the Royal Society of London Series a-Mathematical and Physical Sciences, 243*(1233), 190-205. doi: 10.1098/rspa.1957.0214

Avouac, J. P. (2015). From Geodetic Imaging of Seismic and Aseismic Fault Slip to Dynamic Modeling of the Seismic Cycle. In R. Jeanloz & K. H. Freeman (Eds.), *Annual Review of Earth and Planetary Sciences* (Vol. 43, pp. 233-271).

Barbot, S., Fialko, Y., & Bock, Y. (2009). Postseismic deformation due to the Mw 6.0 2004 Parkfield earthquake: Stress-driven creep on a fault with spatially variable rate-and-state friction parameters. *Journal of Geophysical Research-Solid Earth, 114*, B07405. doi: 10.1029/2008JB005748

Bebout, G. E., & Barton, M. D. (2002). Tectonic and metasomatic mixing in a high-T, subduction-zone melange - insights into the geochemical evolution of the slab-mantle interface. *Chemical Geology, 187*(1-2), 79-106. doi: 10.1016/s0009-2541(02)00019-0

Bender, B. (1983). Maximum-likelihood estimation of b-values for magnitude grouped data. *Bulletin of the Seismological Society of America, 73*(3), 831-851.

Bjerhammar, A. (1973). *Theory of errors and generalized matrix inverse*. Amsterdam: Elsevier publishing company.

Blanpied, M. L., Lockner, D. A., & Byerlee, J. D. (1992). An earthquake mechanism based on rapid sealing of faults. *Nature, 358*(6387), 574-576. doi: 10.1038/358574a0

Bruhat, L., Barbot, S., & Avouac, J. P. (2011). Evidence for postseismic deformation of the lower crust following the 2004 Mw6.0 Parkfield earthquake. *Journal of Geophysical Research-Solid Earth, 116*, B08401. doi: 10.1029/2010jb008073

Byerlee, J. (1993). Model for episodic flow of high-pressure water in fault zones before earthquakes. *Geology, 21*(4), 303-306. doi: 10.1130/0091-7613(1993)021<0303:MFEFOH>2.3.CO;2

Candela, T., Renard, F., Klinger, Y., Mair, K., Schmittbuhl, J., & Brodsky, E. E. (2012). Roughness of fault surfaces over nine decades of length scales. *Journal of Geophysical Research-Solid Earth, 117*, B08409. doi: 10.1029/2011jb009041

Cao, A., & Gao, S. S. (2002). Temporal variation of seismic b-values beneath northeastern Japan island arc. *Geophysical Research Letters, 29*(9). doi: 10.1029/2001GL013775

Carpenter, B. M., Marone, C., & Saffer, D. M. (2011). Weakness of the San Andreas Fault revealed by samples from the active fault zone. *Nature Geoscience, 4*(4), 251-254. doi: 10.1038/ngeo1089

Carpenter, B. M., Saffer, D. M., & Marone, C. (2015). Frictional properties of the active San Andreas Fault at SAFOD: Implications for fault strength and slip behavior. *Journal of Geophysical Research-Solid Earth, 120*(7), 5273-5289. doi: 10.1002/2015jb011963

Chen, C. W., & Zebker, H. A. (2001). Two-dimensional phase unwrapping with use of statistical models for cost functions in nonlinear optimization. *Journal of the Optical Society of America A, 18*(2), 338–351. doi: 10.1364/JOSAA.18.000338

Chen, T., & Lapusta, N. (2009). Scaling of small repeating earthquakes explained by interaction of seismic and aseismic slip in a rate and state fault model. *Journal of Geophysical Research-Solid Earth, 114*, B01311. doi: 10.1029/2008JB005749

Chlieh, M., Mothes, P. A., Nocquet, J. M., Jarrin, P., Charvis, P., Cisneros, D., et al. (2014). Distribution of discrete seismic asperities and aseismic slip along the Ecuadorian megathrust. *Earth and Planetary Science Letters, 400*, 292-301. doi: 10.1016/j.epsl.2014.05.027

Clotet, X., Ortin, J., & Santucci, S. (2016). Experimental study of stable imbibition displacements in a model open fracture. I. Local avalanche dynamics. *Physical Review E, 93*(1), 012149. doi: 10.1103/PhysRevE.93.012149

Corbi, F., Funiciello, F., Brizzi, S., Lallemand, S., & Rosenau, M. (2017). Control of asperities size and spacing on seismic behavior of subduction megathrusts. *Geophysical Research Letters, 44*(16), 8227-8235. doi: doi:10.1002/2017GL074182

Costantini, M., & Rosen, P. A. (1999). *A generalized phase unwrapping approach for sparse data.* Paper presented at the in Proceedings of the IEEE 1999 International Geoscience and Remote Sensing Symposium (IGARSS), Hamburg, Germany.

DeMets, C., Gordon, R. G., & Argus, D. F. (2010). Geologically current plate motions. *Geophysical Journal International, 181*(1), 1-80. doi: 10.1111/j.1365-246X.2009.04491.x

Dieterich, J. H. (1979). Modeling of rock friction: 1. Experimental results and constitutive equations. *Journal of Geophysical Research-Solid Earth, 84*(B5), 2161-2168. doi: 10.1029/JB084iB05p02161

Dragert, G., Wang, K., & James, T. S. (2001). A silent slip event on the deeper Cascadia subduction interface. *Science, 292*(5521), 1525-1528. doi: 10.1126/science.1060152

Dublanchet, P., Bernard, P., & Favreau, P. (2013). Interactions and triggering in a 3-D rate-and-state asperity model. *Journal of Geophysical Research-Solid Earth, 118*(5), 2225-2245. doi: 10.1002/jgrb.50187

Dupont, P. E., & Bapna, D. (1994). Stability of sliding frictional surfaces with varying normal force. *Journal of Vibration and Acoustics-Transactions of the Asme, 116*(2), 237-242. doi: 10.1115/1.2930418

Duputel, Z., Agram, P. S., Simons, M., Minson, S. E., & Beck, J. L. (2014). Accounting for prediction uncertainty when inferring subsurface fault slip. *Geophysical Journal International, 197*(1), 464-482. doi: 10.1093/gji/ggt517

Efron, B., & Tibshirani, R. (1993). *An Introduction to the bootstrap*. New York: Chapman & Hall.

Fagereng, A. (2011). Fractal vein distributions within a fault-fracture mesh in an exhumed accretionary melange, Chrystalls Beach Complex, New Zealand. *Journal of Structural Geology, 33*(5), 918-927. doi: 10.1016/j.jsg.2011.02.009

Fagereng, A., & Sibson, R. H. (2010). Melange rheology and seismic style. *Geology, 38*(8), 751-754. doi: 10.1130/g30868.1

Faulkner, D. R., Mitchell, T. M., Healy, D., & Heap, M. J. (2006). Slip on 'weak' faults by the rotation of regional stress in the fracture damage zone. *Nature, 444*(7121), 922-925. doi: 10.1038/nature05353

Franceschetti, G., & Lanari, R. (1999). *Synthetic aperture radar processing*. Boca Raton, Florida: CRC Press.

Freed, A. M. (2007). Afterslip (and only afterslip) following the 2004 Parkfield, California, earthquake. *Geophysical Research Letters, 34*(6), L06312. doi: 10.1029/2006gl029155

Fukuda, J. i., Kato, A., Kato, N., & Aoki, Y. (2013). Are the frictional properties of creeping faults persistent? Evidence from rapid afterslip following the 2011 Tohoku-oki earthquake. *Geophysical Research Letters, 40*, 3613–3617. doi: 10.1002/grl.50713

Fulton, P. M., & Saffer, D. M. (2009). Potential role of mantle-derived fluids in weakening the San Andreas Fault. *Journal of Geophysical Research-Solid Earth, 114*, B07408. doi: 10.1029/2008jb006087

Gao, S. S., Silver, P. G., & Linde, A. T. (2000). Analysis of deformation data at Parkfield, California: Detection of a long-term strain transient. *Journal of Geophysical Research-Solid Earth, 105*(B2), 2955-2967. doi: 10.1029/1999JB900383

Gao, X., & Wang, K. L. (2014). Strength of stick-slip and creeping subduction megathrusts from heat flow observations. *Science, 345*(6200), 1038-1041. doi: 10.1126/science.1255487

Gilbert, R. O. (1987). *Statistical methods for environmental pollution monitoring*. New York: Van Nostrand Reinhold Co.

Gonzalez, P. J., Tiampo, K. F., Camacho, A. G., & Fernandez, J. (2010). Shallow flank deformation at Cumbre Vieja volcano (Canary Islands): Implications on the stability

of steep-sided volcano flanks at oceanic islands. *Earth and Planetary Science Letters, 297*(3-4), 545-557. doi: 10.1016/j.epsl.2010.07.006

Goswami, J. C., & Chan, A. K. (1999). *Fundamentals of Wavelets: Theory, Algorithms, and Applications*. Hoboken, New Jersey: Wiley-Interscience.

Grewal, M. S., & Andrews, A. P. (2001). *Kalman Filtering : Theory and Practice Using MATLAB*. Hoboken, New Jersey: Wiley-Interscience.

Gutenberg, B., & Richter, C. F. (1944). Frequency of earthquakes in California. *Bulletin of the Seismological Society of America, 34*(4), 185-188.

Hanssen, R. F. (2001). *Radar interferometry, data interpretation and error analysis*. Dordrecht: Kluwer Academic Publishers.

Harris, R. A., & Segall, P. (1987). Detection of a Locked Zone at Depth on the Parkfield, California, Segment of the San-Andreas Fault. *Journal of Geophysical Research-Solid Earth and Planets, 92*(B8), 7945-7962. doi: 10.1029/Jb092ib08p07945

Hayes, G. P., Wald, D. J., & Johnson, R. L. (2012). Slab1.0: A three-dimensional model of global subduction zone geometries. *Journal of Geophysical Research: Solid Earth, 117*(B1), B01302. doi: 10.1029/2011JB008524

Heki, K. (2004). Space geodetic observation of deep basal subduction erosion in northeastern Japan. *Earth and Planetary Science Letters, 219*(1-2), 13-20. doi: 10.1016/s0012-821x(03)00693-9

Heuret, A., Conrad, C. P., Funiciello, F., Lallemand, S., & Sandri, L. (2012). Relation between subduction megathrust earthquakes, trench sediment thickness and upper plate strain. *Geophysical Research Letters, 39*, L05304. doi: 10.1029/2011gl050712

Hillers, G., & Miller, S. A. (2007). Dilatancy controlled spatiotemporal slip evolution of a sealed fault with spatial variations of the pore pressure. *Geophysical Journal International, 168*(1), 431-445. doi: 10.1111/j.1365-246X.2006.03167.x

Hirose, H., Hirahara, K., Kimata, F., Fujii, N., & Miyazaki, S. (1999). A slow thrust slip event following the two 1996 Hyuganada earthquakes beneath the Bungo Channel, Southwest Japan. *Geophysical Research Letters, 26*(21), 3237-3240. doi: 10.1029/1999GL010999

Holland, P. W., & Welsch, R. E. (1977). Robust Regression Using Iteratively Reweighted Least-Squares. *Communications in Statistics: Theory and Methods, A6*, 813-827.

Ide, S., & Aochi, H. (2005). Earthquakes as multiscale dynamic ruptures with heterogeneous fracture surface energy. *Journal of Geophysical Research-Solid Earth, 110*(B11), B11303. doi: 10.1029/2004jb003591

Iio, Y., Kobayashi, Y., & Tada, T. (2002). Large earthquakes initiate by the acceleration of slips on the downward extensions of seismogenic faults. *Earth and Planetary Science Letters, 202*(2), 337-343. doi: 10.1016/S0012-821X(02)00776-8

Ikari, M. J., Marone, C., Saffer, D. M., & Kopf, A. J. (2013). Slip weakening as a mechanism for slow earthquakes. *Nature Geoscience, 6*(6), 468-472. doi: 10.1038/ngeo1818

Ito, Y., Hino, R., Kido, M., Fujimoto, H., Osada, Y., Inazu, D., et al. (2013). Episodic slow slip events in the Japan subduction zone before the 2011 Tohoku-Oki earthquake. *Tectonophysics, 600*, 14-26. doi: 10.1016/j.tecto.2012.08.022

Johanson, I. A., Fielding, E. J., Rolandone, F., & Burgmann, R. (2006). Coseismic and postseismic slip of the 2004 Parkfield earthquake from space-geodetic data. *Bulletin of the Seismological Society of America, 96*(4), S269-S282. doi: 10.1785/0120050818

Johnson, K. M. (2013). Is stress accumulating on the creeping section of the San Andreas fault? *Geophysical Research Letters, 40*(23), 6101-6105. doi: 10.1002/2013gl058184

Jolivet, R., Candela, T., Lasserre, C., Renard, F., Klinger, Y., & Doin, M. P. (2015a). The Burst-Like Behavior of Aseismic Slip on a Rough Fault: The Creeping Section of the Haiyuan Fault, China. *Bulletin of the Seismological Society of America, 105*(1), 480-488. doi: 10.1785/0120140237

Jolivet, R., Simons, M., Agram, P. S., Duputel, Z., & Shen, Z. K. (2015b). Aseismic slip and seismogenic coupling along the central San Andreas Fault. *Geophysical Research Letters, 42*(2), 297-306. doi: 10.1002/2014gl062222

Jónsson, S., Zebker, H., Segall, P., & Amelung, F. (2002). Fault Slip Distribution of the 1999 Mw7.1 Hector Mine Earthquake, California, estimated from Satellite Radar and GPS Measurements. *Bulletin of the Seismological Society of America, 92*(4), 1377-1389. doi: 10.1785/0120000922

Kaneko, Y., Avouac, J.-P., & Lapusta, N. (2010). Towards inferring earthquake patterns from geodetic observations of interseismic coupling. *Nature Geoscience, 3*(5), 363-U324. doi: 10.1038/ngeo843

Kaproth, B. M., & Marone, C. (2013). Slow Earthquakes, Preseismic Velocity Changes, and the Origin of Slow Frictional Stick-Slip. *Science, 341*(6151), 1229-1232. doi: 10.1126/science.1239577

Kato, A., Obara, K., Igarashi, T., Tsuruoka, H., Nakagawa, S., & Hirata, N. (2012). Propagation of Slow Slip Leading Up to the 2011 M-w 9.0 Tohoku-Oki Earthquake. *Science, 335*(6069), 705-708. doi: 10.1126/science.1215141

Khoshmanesh, M., & Shirzaei, M. (2018a). Episodic creep events on the San Andreas Fault caused by pore pressure variations. *Nature Geoscience, 11*(8), 610-614. doi: 10.1038/s41561-018-0160-2

Khoshmanesh, M., & Shirzaei, M. (2018b). Multiscale Dynamics of Aseismic Slip on Central San Andreas Fault. *Geophysical Research Letters, 45*(5), 2274-2282. doi: 10.1002/2018GL077017

Khoshmanesh, M., Shirzaei, M., & Nadeau, R. M. (2015). Time-dependent model of aseismic slip on the central San Andreas Fault from InSAR time series and repeating earthquakes. *Journal of Geophysical Research-Solid Earth, 120*(9), 6658-6679. doi: 10.1002/2015JB012039

Kodaira, S., Iidaka, T., Kato, A., Park, J.-O., Iwasaki, T., & Kaneda, Y. (2004). High pore fluid pressure may cause silent slip in the Nankai trough. *Science, 304*(5675), 1295-1298. doi: 10.1126/science.1096535

Konca, A. O., Avouac, J. P., Sladen, A., Meltzner, A. J., Sieh, K., Fang, P., et al. (2008). Partial rupture of a locked patch of the Sumatra megathrust during the 2007 earthquake sequence. *Nature, 456*(7222), 631-635. doi: 10.1038/nature07572

Kostoglodov, V., Singh, S. K., Santiago, J. A., Franco, S. I., Larson, K. M., Lowry, A. R., & Bilham, R. (2003). A large silent earthquake in the Guerrero seismic gap, Mexico. *Geophysical Research Letters, 30*(15), 1807. doi: 10.1029/2003gl017219

Lay, T., Kanamori, H., & Ruff, L. (1982). The asperity model and the nature of large subduction zone earthquakes. *Earthquake Prediction Research, 1*, 3-71.

Leclere, H., Faulkner, D., Wheeler, J., & Mariani, E. (2016). Permeability control on transient slip weakening during gypsum dehydration: Implications for earthquakes in subduction zones. *Earth and Planetary Science Letters, 442*, 1-12. doi: 10.1016/j.epsl.2016.02.015

Lee, S.-J., Huang, B.-S., Ando, M., Chiu, H.-C., & Wang, J.-H. (2011). Evidence of large scale repeating slip during the 2011 Tohoku-Oki earthquake. *Geophysical Research Letters, 38*(19), L19306. doi: 10.1029/2011gl049580

Leeman, J. R., Saffer, D. M., Scuderi, M. M., & Marone, C. (2016). Laboratory observations of slow earthquakes and the spectrum of tectonic fault slip modes. *Nature Communications, 7*, 11104. doi: 10.1038/ncomms11104

Lienkaemper, J. J., McFarland, F. S., Simpson, R. W., Bilham, R. G., Ponce, D. A., Boatwright, J. J., & Caskey, S. J. (2012). Long-Term Creep Rates on the Hayward Fault: Evidence for Controls on the Size and Frequency of Large Earthquakes. *Bulletin of the Seismological Society of America, 102*(1), 31-41. doi: 10.1785/0120110033

Liu, Y. J., & Rice, J. R. (2007). Spontaneous and triggered aseismic deformation transients in a subduction fault model. *Journal of Geophysical Research-Solid Earth, 112*(B9), B09404. doi: 10.1029/2007jb004930

Lockner, D. A., & Byerlee, J. D. (1995). An earthquake instability model based on faults containing high fluid pressure compartments. *Pure and Applied Geophysics, 145*(3/4), 717-746.

Lockner, D. A., Morrow, C., Moore, D., & Hickman, S. (2011). Low strength of deep San Andreas fault gouge from SAFOD core. *Nature, 472*(7341), 82-85. doi: 10.1038/nature09927

Lopez-Martinez, C., & Fabregas, X. (2002). Modeling and reduction of SAR interferometric phase noise in the wavelet domain. *Ieee Transactions on Geoscience and Remote Sensing, 40*(12), 2553-2566. doi: 10.1109/TGRS.2002.806997

Maloy, K. J., Santucci, S., Schmittbuhl, J., & Toussaint, R. (2006). Local waiting time fluctuations along a randomly pinned crack front. *Physical Review Letters, 96*(4), 045501. doi: 10.1103/PhysRevLett.96.045501

Malservisi, R., Furlong, K. P., & Gans, C. R. (2005). Microseismicity and creeping faults: Hints from modeling the Hayward fault, California (USA). *Earth and Planetary Science Letters, 234*(3-4), 421-435. doi: 10.1016/j.epsl.2005.02.039

Marchenko, A., Fichou, D., Bonamy, D., & Bouchaud, E. (2006). Time resolved observation of fracture events in mica crystal using scanning tunneling microscope. *Applied Physics Letters, 89*(9), 093124. doi: 10.1063/1.2335823

Marone, C. (1998). Laboratory-derived friction laws and their application to seismic faulting. *Annual Review of Earth and Planetary Sciences, 26*, 643-696. doi: 10.1146/annurev.earth.26.1.643

Marone, C., & Kilgore, B. (1993). Scaling of the critical slip distance for seismic faulting with shear strain in fault zones. *Nature, 362*(6421), 618-621. doi: 10.1038/362618a0

Marone, C., Scholz, C. H., & Bilham, R. (1991). On the mechanics of earthquake afterslip. *Journal of Geophysical Research-Solid Earth, 96*(B5), 8441-8452. doi: 10.1029/91JB00275

Maurer, J., & Johnson, K. (2014). Fault coupling and potential for earthquakes on the creeping section of the central San Andreas Fault. *Journal of Geophysical Research-Solid Earth, 119*(5), 4414-4428. doi: 10.1002/2013jb010741

Mavrommatis, A. P., Segall, P., & Johnson, K. M. (2014). A decadal-scale deformation transient prior to the 2011 M-w 9.0 Tohoku-oki earthquake. *Geophysical Research Letters, 41*(13), 4486-4494. doi: 10.1002/2014gl060139

Mavrommatis, A. P., Segall, P., Uchida, N., & Johnson, K. M. (2015). Long-term acceleration of aseismic slip preceding the M-w 9 Tohoku-oki earthquake: Constraints from repeating earthquakes. *Geophysical Research Letters, 42*(22), 9717-9725. doi: 10.1002/2015gl066069

Meade, B. J. (2007). Algorithms for the calculation of exact displacements, strains, and stresses for triangular dislocation elements in a uniform elastic half space. *Computers & Geosciences, 33*(8), 1064-1075. doi: 10.1016/j.cageo.2006.12.003

Meneghini, F., Di Toro, G., Rowe, C. D., Moore, J. C., Tsutsumi, A., & Yamaguchi, A. (2010). Record of mega-earthquakes in subduction thrusts: The black fault rocks of

Pasagshak Point (Kodiak Island, Alaska). *Geological Society of America Bulletin, 122*(7-8), 1280-1297. doi: 10.1130/b30049.1

Meng, L. S., Inbal, A., & Ampuero, J. P. (2011). A window into the complexity of the dynamic rupture of the 2011 Mw 9 Tohoku-Oki earthquake. *Geophysical Research Letters, 38*, L00g07. doi: 10.1029/2011gl048118

Mikhail, E. M. (1976). *Observations and least squares* New York: IEP

Miller, M. M., Melbourne, T., Johnson, D. J., & Sumner, W. Q. (2002). Periodic slow earthquakes from the Cascadia subduction zone. *Science, 295*(5564), 2423. doi: 10.1126/science.1071193

Mittempergher, S., Di Toro, G., Gratier, J. P., Hadizadeh, J., Smith, S. A. F., & Spiess, R. (2011). Evidence of transient increases of fluid pressure in SAFOD phase III cores. *Geophysical Research Letters, 38*, L03301. doi: 10.1029/2010gl046129

Miyazaki, S., & Larson, K. M. (2008). Coseismic and early postseismic slip for the 2003 Tokachi-oki earthquake sequence inferred from GPS data. *Geophysical Research Letters, 35*(4), L04302. doi: 10.1029/2007gl032309

Miyazaki, S., McGuire, J. J., & Segall, P. (2003). A transient subduction zone slip episode in southwest Japan observed by the nationwide GPS array. *Journal of Geophysical Research-Solid Earth, 108*(B2), 2087. doi: 10.1029/2001jb000456

Morrow, C. A., Lockner, D. A., Moore, D. E., & Hickman, S. (2014). Deep permeability of the San Andreas Fault from San Andreas Fault Observatory at Depth (SAFOD) core samples. *Journal of Structural Geology, 64*, 99-114. doi: 10.1016/j.jsg.2013.09.009

Murray, J. R., & Segall, P. (2002). Testing time-predictable earthquake recurrence by direct measurement of strain accumulation and release. *Nature, 419*(6904), 287-291. doi: 10.1038/nature00984

Murray, J. R., & Segall, P. (2005). Spatiotemporal evolution of a transient slip event on the San Andreas fault near Parkfield, California. *Journal of Geophysical Research-Solid Earth, 110*(B9), B09407. doi: 10.1029/2005JB003651

Murray, J. R., Segall, P., Cervelli, P., Prescott, W., & Svarc, J. (2001). Inversion of GPS data for spatially variable slip-rate on the San Andreas fault near Parkfield, CA. *Geophysical Research Letters, 28*(2), 359-362. doi: 10.1029/2000GL011933

Nadeau, R., Antolik, M., Johnson, P. A., Foxall, W., & McEvilly, T. V. (1994). Seismological studies at Parkfield III: Microearthquake clusters in the study of fault-zone dynamics. *Bulletin of the Seismological Society of America, 84*(2), 247-263.

Nadeau, R. M., Foxall, W., & McEvilly, T. V. (1995). Clustering and Periodic Recurrence of Microearthquakes on the San-Andreas Fault at Parkfield, California. *Science, 267*(5197), 503-507. doi: 10.1126/science.267.5197.503

Nadeau, R. M., & Johnson, L. R. (1998). Seismological studies at Parkfield VI: Moment release rates and estimates of source parameters for small repeating earthquakes. *Bulletin of the Seismological Society of America, 88*(3), 790-814.

Nadeau, R. M., & McEvilly, T. V. (2004). Periodic pulsing of characteristic microearthquakes on the San Andreas fault. *Science, 303*(5655), 220-222. doi: 10.1126/science.1090353

Nakata, N., & Snieder, R. (2011). Near-surface weakening in Japan after the 2011 Tohoku-Oki earthquake. *Geophysical Research Letters, 38*(17), L17302. doi: 10.1029/2011gl048800

Noda, H., & Lapusta, N. (2013). Stable creeping fault segments can become destructive as a result of dynamic weakening. *Nature, 493*(7433), 518-521. doi: 10.1038/nature11703

O'leary, D. P. (1990). Robust Regression Computation Using Iteratively Reweighted Least-Squares. *Siam Journal on Matrix Analysis and Applications, 11*(3), 466-480. doi: 10.1137/0611032

Obara, K., Hirose, H., Yamamizu, F., & Kasahara, K. (2004). Episodic slow slip events accompanied by non-volcanic tremors in southwest Japan subduction zone. *Geophysical Research Letters, 31*(23), L23602. doi: 10.1029/2004GL020848

Okada, Y. (1992). Internal deformation due to shear and tensile faults in a half-space. *Bulletin of the Seismological Society of America, 82*(2), 1018-1040.

Okubo, P. G., & Dieterich, J. H. (1984). Effects of physical fault properties on frictional instabilities produced on simulated faults. *Journal of Geophysical Research-Solid Earth, 89*(B7), 5817-5827. doi: 10.1029/JB089iB07p05817

Ozawa, S., Miyazaki, S. i., Hatanaka, Y., Imakiire, T., Kaidzu, M., & Murakami, M. (2003). Characteristic silent earthquakes in the eastern part of the Boso peninsula, Central Japan. *Geophysical Research Letters, 30*(6), 1283. doi: 10.1029/2002GL016665

Ozawa, S., Murakami, M., Kaidzu, M., Tada, T., Sagiya, T., Hatanaka, Y., et al. (2002). Detection and Monitoring of ongoing aseismic Slip in the Tokai region, Central Japan. *Science, 298*(5595), 1009-1012. doi: 10.1126/science.1076780

Ozawa, S., Nishimura, T., Munekane, H., Suito, H., Kobayashi, T., Tobita, M., & Imakiire, T. (2012). Preceding, coseismic, and postseismic slips of the 2011 Tohoku earthquake, Japan. *Journal of Geophysical Research-Solid Earth, 117*(B7), B07404. doi: 10.1029/2011jb009120

Pacheco, J. F., Sykes, L. R., & Scholz, C. H. (1993). Nature of seismic coupling along simple plate boundaries of the subduction type. *Journal of Geophysical Research-Solid Earth, 98*(B8), 14133-14159. doi: 10.1029/93jb00349

Parsons, T. (2002). Post-1906 stress recovery of the San Andreas fault system calculated from three-dimensional finite element analysis. *Journal of Geophysical Research-Solid Earth, 107*(B8), 1-13. doi: 10.1029/2001JB001051

Perfettini, H., & Ampuero, J. P. (2008). Dynamics of a velocity strengthening fault region: Implications for slow earthquakes and postseismic slip. *Journal of Geophysical Research-Solid Earth, 113*(B9), B09411. doi: 10.1029/2007jb005398

Perfettini, H., & Avouac, J. P. (2007). Modeling afterslip and aftershocks following the 1992 Landers earthquake. *Journal of Geophysical Research-Solid Earth, 112*(B7), B07409. doi: 10.1029/2006jb004399

Perfettini, H., Avouac, J. P., Tavera, H., Kositsky, A., Nocquet, J. M., Bondoux, F., et al. (2010). Seismic and aseismic slip on the central Peru megathrust. *Nature, 465*(7294), 78-81. doi: 10.1038/nature09062

Planet, R., Santucci, S., & Ortín, J. (2009). Avalanches and Non-Gaussian Fluctuations of the Global Velocity of Imbibition Fronts. *Physical Review Letters, 102*(9), 094502 doi: 10.1103/PhysRevLett.102.094502

Radiguet, M., Perfettini, H., Cotte, N., Gualandi, A., Valette, B., Kostoglodov, V., et al. (2016). Triggering of the 2014 Mw7.3 Papanoa earthquake by a slow slip event in Guerrero, Mexico. *Nature Geoscience, 9*(11), 829-833. Letter. doi: 10.1038/ngeo2817

Rice, J. R. (1992). Fault stress states, pore pressure distributions, and the weakness of the San Andreas fault. In B. Evans & T.-F. Wong (Eds.), *Earthquake Mechanics, Rock Deformation, and Transport Properties of Rocks* (pp. 475-503). San Diego, Calif.: Academic.

Richter, C. F. (1958). *Elementary Seismology*. San Francisco, California: Freeman.

Rogers, G., & Dragert, H. (2003). Episodic tremor and slip on the Cascadia subduction zone: the chatter of silent slip. *Science, 300*(5627), 1942-1943. doi: 10.1126/science.1084783

Rolandone, F., Burgmann, R., Agnew, D. C., Johanson, I. A., Templeton, D. C., d'Alessio, M. A., et al. (2008). Aseismic slip and fault-normal strain along the central creeping section of the San Andreas fault. *Geophysical Research Letters, 35*(14), L14305. doi: 10.1029/2008gl034437

Rolandone, F., Nocquet, J. M., Mothes, P. A., Jarrin, P., Vallee, M., Cubas, N., et al. (2018). Areas prone to slow slip events impede earthquake rupture propagation and promote afterslip. *Science Advances, 4*(1), eaao6596. doi: 10.1126/sciadv.aao6596

Rubin, A. M., & Ampuero, J.-P. (2005). Earthquake nucleation on (aging) rate and state faults. *Journal of Geophysical Research-Solid Earth, 110*(B11), B11312. doi: 10.1029/2005JB003686

Ruina, A. (1983). Slip instability and state variable friction laws. *Journal of Geophysical Research-Solid Earth, 88*(B12), 10359-10370. doi: 10.1029/JB088iB12p10359

Ryder, I., & Bürgmann, R. (2008). Spatial variations in slip deficit on the central San Andreas Fault from InSAR. *Geophysical Journal International, 175*(3), 837-852. doi: 10.1111/j.1365-246X.2008.03938.x

Sagiya, T. (2004). Interplate coupling in the Kanto district, central Japan, and the Boso Peninsula silent earthquake in May 1996. *Pure and Applied Geophysics, 161*(11-12), 2327-2342. doi: 10.1007/s0024-004-2566-6

Sagiya, T., Miyazaki, S., & Tada, T. (2000). Continuous GPS array and present-day crustal deformation of Japan. *Pure and Applied Geophysics, 157*(11/12), 2303-2322.

Satriano, C., Dionicio, V., Miyake, H., Uchida, N., Vilotte, J. P., & Bernard, P. (2014). Structural and thermal control of seismic activity and megathrust rupture dynamics in subduction zones: Lessons from the Mw 9.0, 2011 Tohoku earthquake. *Earth and Planetary Science Letters, 403*, 287-298. doi: 10.1016/j.epsl.2014.06.037

Sawai, M., Niemeijer, A. R., Hirose, T., & Spiers, C. J. (2017). Frictional properties of JFAST core samples and implications for slow earthquakes at the Tohoku subduction zone. *Geophysical Research Letters, 44*(17), 8822-8831. doi: 10.1002/2017gl073460

Schaff, D. P., Beroza, G. C., & Shaw, B. E. (1998). Postseismic response of repeating aftershocks. *Geophysical Research Letters, 25*(24), 4549-4552. doi: 10.1029/1998GL900192

Schmitt, S. V., Segall, P., & Matsuzawa, T. (2011). Shear heating-induced thermal pressurization during earthquake nucleation. *Journal of Geophysical Research-Solid Earth, 116*, B06308. doi: 10.1029/2010jb008035

Schmittbuhl, J., Schmitt, F., & Scholz, C. (1995a). Scaling invariance of crack surfaces. *Journal of Geophysical Research-Solid Earth, 100*(B4), 5953-5973. doi: 10.1029/94JB02885

Schmittbuhl, J., Vilotte, J. P., & Roux, S. (1995b). Reliability of self-affine measurements. *Physical Review E, 51*(1), 131-147. doi: 10.1103/PhysRevE.51.131

Scholz, C. H. (1988). The critical slip distance for seismic faulting. *Nature, 336*(6201), 761-763. doi: 10.1038/336761a0

Scholz, C. H. (1998). Earthquakes and friction laws. *Nature, 391*, 37-42. doi: 10.1038/34097

Scholz, C. H., & Engelder, J. T. (1976). The role of asperity indentation and ploughing in rock friction, I. Asperity creep and stick-slip. *International Journal of Rock Mechanics and Mining Sciences, 13*(5), 149-154. doi: 10.1016/0148-9062(76)90819-6

Schorlemmer, D., Wiemer, S., & Wyss, M. (2004). Earthquake statistics at Parkfield: 1. Stationarity of b values. *Journal of Geophysical Research-Solid Earth, 109*(B12), B12307. doi: 10.1029/2004JB003234

Schorlemmer, D., Wiemer, S., & Wyss, M. (2005). Variations in earthquake-size distribution across different stress regimes. *Nature, 437*(7058), 539-542. doi: 10.1038/nature04094

Schurr, B., Asch, G., Hainzl, S., Bedford, J., Hoechner, A., Palo, M., et al. (2014). Gradual unlocking of plate boundary controlled initiation of the 2014 Iquique earthquake. *Nature, 512*(7514), 299-302. doi: 10.1038/nature13681

Scuderi, M. M., & Collettini, C. (2016). The role of fluid pressure in induced vs. triggered seismicity: insights from rock deformation experiments on carbonates. *Scientific Reports, 6*, 24852. doi: 10.1038/srep24852

Segall, P. (2010). *Earthquake and Volcano Deformation*. Princeton, New Jersey: Princeton University Press.

Segall, P., & Harris, R. (1987). Earthquake Deformation Cycle on the San-Andreas Fault near Parkfield, California. *Journal of Geophysical Research-Solid Earth and Planets, 92*(B10), 10511-10525. doi: 10.1029/Jb092ib10p10511

Segall, P., Rubin, A. M., Bradley, A. M., & Rice, J. R. (2010). Dilatant strengthening as a mechanism for slow slip events. *Journal of Geophysical Research-Solid Earth, 115*, B12305. doi: 10.1029/2010jb007449

Shelly, D. R. (2009). Possible deep fault slip preceding the 2004 Parkfield earthquake, inferred from detailed observations of tectonic tremor. *Geophysical Research Letters, 36*, L17318. doi: 10.1029/2009gl039589

Shelly, D. R., Peng, Z. G., Hill, D. P., & Aiken, C. (2011). Triggered creep as a possible mechanism for delayed dynamic triggering of tremor and earthquakes. *Nature Geoscience, 4*(6), 384-388. doi: 10.1038/ngeo1141

Shi, Y., & Bolt, B. A. (1982). The standard error of the magnitude-frequency b-value. *Bulletin of the Seismological Society of America, 72*(5), 1677-1687.

Shibazaki, B., & Iio, Y. (2003). On the physical mechanism of silent slip events along the deeper part of the seismogenic zone. *Geophysical Research Letters, 30*(9), 42-41 to 42-44. doi: 10.1029/2003GL017047

Shibazaki, B., Matsuzawa, T., Tsutsumi, A., Ujiie, K., Hasegawa, A., & Ito, Y. (2011). 3D modeling of the cycle of a great Tohoku-oki earthquake, considering frictional behavior at low to high slip velocities. *Geophysical Research Letters, 38*(21), L21305. doi: 10.1029/2011gl049308

Shirzaei, M. (2013). A Wavelet-Based Multitemporal DInSAR Algorithm for Monitoring Ground Surface Motion. *IEEE Geoscience and Remote Sensing Letters, 10*(3), 456-460. doi: 10.1109/Lgrs.2012.2208935

Shirzaei, M., & Bürgmann, R. (2012). Topography correlated atmospheric delay correction in radar interferometry using wavelet transforms. *Geophysical Research Letters, 39*(1), L01305. doi: 10.1029/2011GL049971

Shirzaei, M., & Bürgmann, R. (2013). Time-dependent model of creep on Hayward fault inferred from joint inversion of 18 years InSAR time series and surface creep data. *Journal of Geophysical Research-Solid Earth, 118*, 1733–1746. doi: 10.1002/jgrb.50149

Shirzaei, M., Bürgmann, R., & Taira, T. a. (2013). Implications of recent asperity failures and aseismic creep for time-dependent earthquake hazard on the Hayward fault. *Earth and Planetary Science Letters, 371–372*, 59-66. doi: 10.1016/j.epsl.2013.04.024

Shirzaei, M., Burgmann, R., Uchida, N., Hu, Y., Pollitz, F., & Matsuzawa, T. (2014). Seismic versus aseismic slip: Probing mechanical properties of the northeast Japan subduction zone. *Earth and Planetary Science Letters, 406*, 7-13. doi: 10.1016/j.epsl.2014.08.035

Shirzaei, M., & Walter, T. R. (2010). Time-dependent volcano source monitoring using interferometric synthetic aperture radar time series: A combined genetic algorithm and Kalman filter approach. *Journal of Geophysical Research-Solid Earth, 115*, B10421. doi: 10.1029/2010jb007476

Shirzaei, M., & Walter, T. R. (2011). Estimating the Effect of Satellite Orbital Error Using Wavelet-Based Robust Regression Applied to InSAR Deformation Data. *Ieee Transactions on Geoscience and Remote Sensing, 49*(11), 4600-4605. doi: 10.1109/Tgrs.2011.2143419

Sibson, R. H. (1982). Zone models, heat-flow, and the depth distribution of earthquakes in the continental-crust of the United States. *Bulletin of the Seismological Society of America, 72*(1), 151-163.

Sieh, K. E. (1978). Slip along San Andreas fault associated with great 1857 earthquake. *Bulletin of the Seismological Society of America, 68*(5), 1421-1448.

Sleep, N. H. (1995). Ductile creep, compaction, and rate and state dependent friction within major fault zones. *Journal of Geophysical Research-Solid Earth, 100*(B7), 13065-13080. doi: 10.1029/94JB03340

Sleep, N. H., & Blanpied, M. L. (1992). Creep, compaction and the weak rheology of major faults. *Nature, 359*(6397), 687-692. doi: 10.1038/359687a0

Song, S. G., Beroza, G. C., & Segall, P. (2008). A unified source model for the 1906 San Francisco earthquake. *Bulletin of the Seismological Society of America, 98*(2), 823-831. doi: 10.1785/0120060402

Tallakstad, K. T., Toussaint, R., Santucci, S., Schmittbuhl, J., & Maloy, K. J. (2011). Local dynamics of a randomly pinned crack front during creep and forced propagation: An experimental study. *Physical Review E, 83*(4), 046108. doi: 10.1103/PhysRevE.83.046108

Tanioka, Y., Ruff, L., & Satake, K. (1997). What controls the lateral variation of large earthquake occurrence along the Japan Trench? *Island Arc, 6*(3), 261-266. doi: 10.1111/j.1440-1738.1997.tb00176.x

Titus, S. J., DeMets, C., & Tikoff, B. (2006). Thirty-five-year creep rates for the creeping segment of the San Andreas fault and the effects of the 2004 Parkfield earthquake: Constraints from alignment arrays, continuous global positioning system, and creepmeters. *Bulletin of the Seismological Society of America, 96*(4), S250-S268. doi: 10.1785/0120050811

Titus, S. J., Dyson, M., DeMets, C., Tikoff, B., Rolandone, F., & Buergmann, R. (2011). Geologic versus geodetic deformation adjacent to the San Andreas fault, central California. *Geological Society of America Bulletin, 123*(5-6), 794-820. doi: 10.1130/b30150.1

Toké, N. A., Arrowsmith, J. R., Rymer, M. J., Landgraf, A., Haddad, D. E., Busch, M., et al. (2011). Late Holocene slip rate of the San Andreas fault and its accommodation by creep and moderate-magnitude earthquakes at Parkfield, California. *Geology, 39*(3), 243-246. doi: 10.1130/G31498.1

Tormann, T., Enescu, B., Woessner, J., & Wiemer, S. (2015). Randomness of megathrust earthquakes implied by rapid stress recovery after the Japan earthquake. *Nature Geoscience, 8*(2), 152-158. doi: 10.1038/ngeo2343

Tormann, T., Wiemer, S., Metzger, S., Michael, A., & Hardebeck, J. L. (2013). Size distribution of Parkfield's microearthquakes reflects changes in surface creep rate. *Geophysical Journal International, 193*(3), 1474-1478. doi: 10.1093/gji/ggt093

Tormann, T., Wiemer, S., & Mignan, A. (2014). Systematic survey of high-resolution b value imaging along Californian faults: Inference on asperities. *Journal of Geophysical Research-Solid Earth, 119*(3), 2029-2054. doi: 10.1002/2013jb010867

Turner, R. C., Shirzaei, M., Nadeau, R. M., & Buergmann, R. (2015). Slow and Go: Pulsing slip rates on the creeping section of the San Andreas Fault. *Journal of Geophysical Research-Solid Earth, 120*(8), 5940-5951. doi: 10.1002/2015JB011998

Uchida, N., Iinuma, T., Nadeau, R. M., Burgmann, R., & Hino, R. (2016). Periodic slow slip triggers megathrust zone earthquakes in northeastern Japan. *Science, 351*(6272), 488-492. doi: 10.1126/science.aad3108

Uchida, N., & Matsuzawa, T. (2013). Pre- and postseismic slow slip surrounding the 2011 Tohoku-oki earthquake rupture. *Earth and Planetary Science Letters, 374*, 81-91. doi: 10.1016/j.epsl.2013.05.021

Utsu, T. (1965). A method for determining the value of b in a formula log n= a-bM showing the magnitude-frequency relation for earthquakes. *Geophysical Bulletin of Hokkaido University, 13*, 99-103.

Waldhauser, F., & Schaff, D. P. (2008). Large-scale relocation of two decades of Northern California seismicity using cross-correlation and double-difference methods. *Journal of Geophysical Research-Solid Earth, 113*(B8), B08311. doi: 10.1029/2007jb005479

Wdowinski, S., Bock, Y., Zhang, J., Fang, P., & Genrich, J. (1997). Southern California Permanent GPS Geodetic Array: Spatial filtering of daily positions for estimating coseismic and postseismic displacements induced by the 1992 Landers earthquake. *Journal of Geophysical Research-Solid Earth, 102*(B8), 18057-18070. doi: 10.1029/97jb01378

Wei, M., Kaneko, Y., Liu, Y., & McGuire, J. J. (2013). Episodic fault creep events in California controlled by shallow frictional heterogeneity. *Nature Geoscience, 6*(7), 566-570. doi: 10.1038/ngeo1835

Wei, M., Liu, Y. J., Kaneko, Y., McGuire, J. J., & Bilham, R. (2015). Dynamic triggering of creep events in the Salton Trough, Southern California by regional M >= 5.4 earthquakes constrained by geodetic observations and numerical simulations. *Earth and Planetary Science Letters, 427*, 1-10. doi: 10.1016/j.epsl.2015.06.044

Weston, J., & Shirzaei, M. (2016). Combining GPS and repeating earthquakes for a high resolution analysis of subduction zone coupling. *Tectonophysics, 667*, 37-47. doi: 10.1016/j.tecto.2015.11.009

Wiemer, S., & Wyss, M. (2002). Mapping spatial variability of the frequency-magnitude distribution of earthquakes. In R. Dmowska & B. Saltzman (Eds.), *Advances in Geophysics*. San Diego: Academic Press.

Williams, C. F., Grubb, F. V., & Galanis, S. P., Jr. (2004). Heat flow in the SAFOD pilot hole and implications for the strength of the San Andreas Fault. *Geophysical Research Letters, 31*(15), L15S14. doi: 10.1029/2003GL019352

Woessner, J., & Wiemer, S. (2005). Assessing the quality of earthquake catalogues: Estimating the magnitude of completeness and its uncertainty. *Bulletin of the Seismological Society of America, 95*(2), 684-698. doi: 10.1785/0120040007

Yabe, S., & Ide, S. (2017). Slip-behavior transitions of a heterogeneous linear fault. *Journal of Geophysical Research-Solid Earth, 122*(1), 387-410. doi: 10.1002/2016jb013132

Yamanaka, Y., & Kikuchi, M. (2004). Asperity map along the subduction zone in northeastern Japan inferred from regional seismic data. *Journal of Geophysical Research-Solid Earth, 109*(B7), B07307. doi: 10.1029/2003jb002683

Yoshioka, N. (1997). A review of the micromechanical approach to the physics of contacting surfaces. *Tectonophysics, 277*(1-3), 29-40. doi: 10.1016/s0040-1951(97)00076-0

Zoback, M. D., Zoback, M. L., Mount, V. S., Suppe, J., Eaton, J., Healy, J. H., et al. (1987). New evidence on the state of stress on the San Andreas Fault System. *Science, 238*(4830), 1105-1111. doi: 10.1126/science.238.4830.1105

APPENDIX A.

JUSTIFICATIONS AND DETAILS FOR THE CONSIDERED TRANSITION ZONE

A 10 km zone of transition from brittle to ductile deformation starting below the seismogenic zone is considered. This transition zone, extending from 15 to 25 km depth, is discretized like the shallow 15 km seismogenic zone of the fault. Considering the extent of the surface deformation observations, the creep obtained on this transition zone has large uncertainties and is not reliable. However, this zone is considered in order to prevent stress singularities at the bottom tip of seismogenic zone, where the creep rate drops suddenly from long-term creep rate in the deep zone to some number obtained in the model for the patches located in this area. Alternatively, a very narrow zone of overlap between seismogenic and deep zone could be considered, e.g., from 12.5 to 15 km. In this way, the deep zone would be considered to extend from 12.5 km to 3000 km depth and a seismogenic zone starting from 12.5 km depth, all the way up to the surface. Then, the creep along both seismogenic and the considered overlapping zone is modeled. The creep is constrained to be almost zero in this overlapping zone, simply because the contribution of creep on deep zone (including the overlapping zone) from the surface deformation observations is already removed. However, having a narrow zone with zero creep, right below the seismogenic zone, the Laplacian operator used for smoothing the creep map would result in artificially decreased creep as well as induced roughness on the patches located at the bottom of seismogenic zone (from 10 to 12.5 km). Figure A.1 shows the long-term creep map along the CSAF, implementing this alternative method.

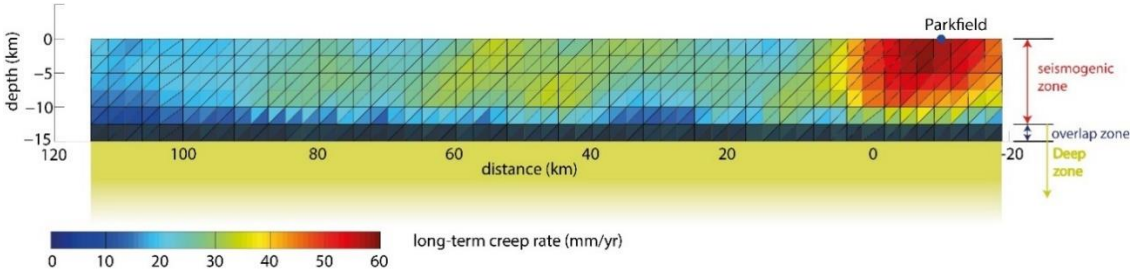

Figure A.1. Long-term creep rate along the CSAF, considering a narrow overlapping zone between seismogenic and deep zone.

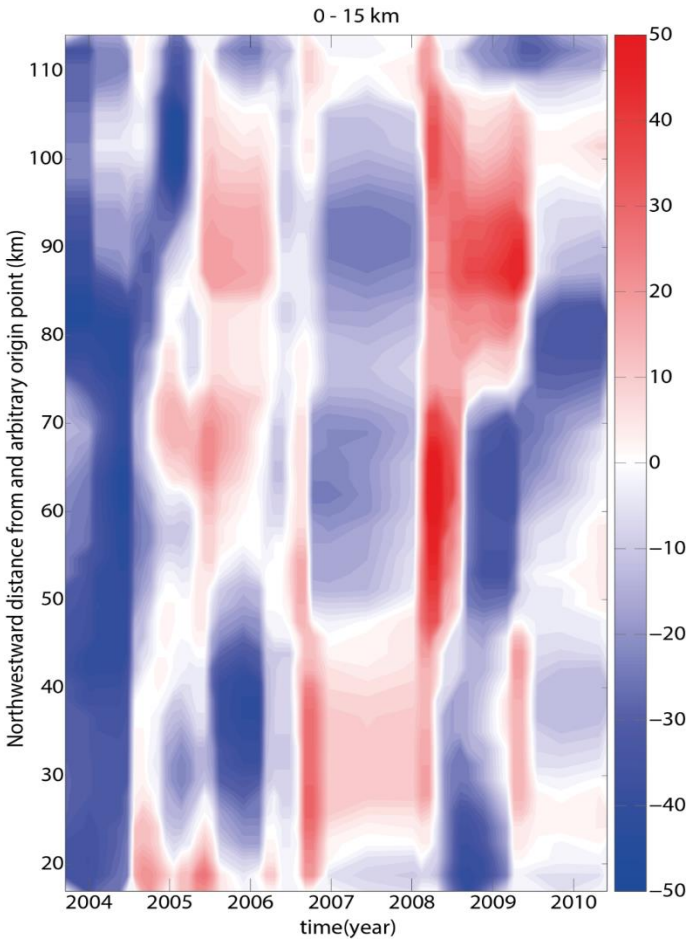

Figure A.2. Creep rate variation considering scenario #1. Time series of the difference between the short-term and long-term creep rate, normalized by the long-term creep rate in percentage, averaged along the dip along the CSAF, using the results obtained from the scenario #1.

APPENDIX B.

THE EFFECT OF SPATIALLY CORRELATED NOISE ON THE UNCERTAINTY OF THE TIME-DEPENDENT CREEP MODEL

To investigate the effect of spatially correlated (or colored) noise on the time series of creep along the CSAF, the atmospheric noise model proposed by Hansen [2002] is used. This model combines three regimes of atmospheric delay, each corresponding to a particular scale factor and characterized by different exponent of the power spectrum:

Regime 1: Scale factor > 2 km: $P_{\varphi}(k) \propto k^{-5/3}$

Regime 2: 0.5 km < scale factor < 2 km: $P_{\varphi}(k) \propto k^{-8/3}$

Regime 3: 0.01 km < scale factor < 0.5 km: $P_{\varphi}(k) \propto k^{-2/3}$

Where, $P_{\varphi}(k)$ is the noise power spectrum and k is the wave number. This model is derived by assuming isotropy for the noise and ignoring ionospheric contributions, which is shown to be adequate assumption for the C-band dataset. Figure B1 shows an example of the simulated colored noise, generated using equation above and considering 5 mm of standard deviation. The effect of this colored noise on the creep model is investigated through bootstrapping as detailed in section 2.3.1 of the main text. Figures B2 to B10 show the estimated standard deviation for the creep time series. The standard deviation, however, is estimated for every other 5th time step to save the computation time.

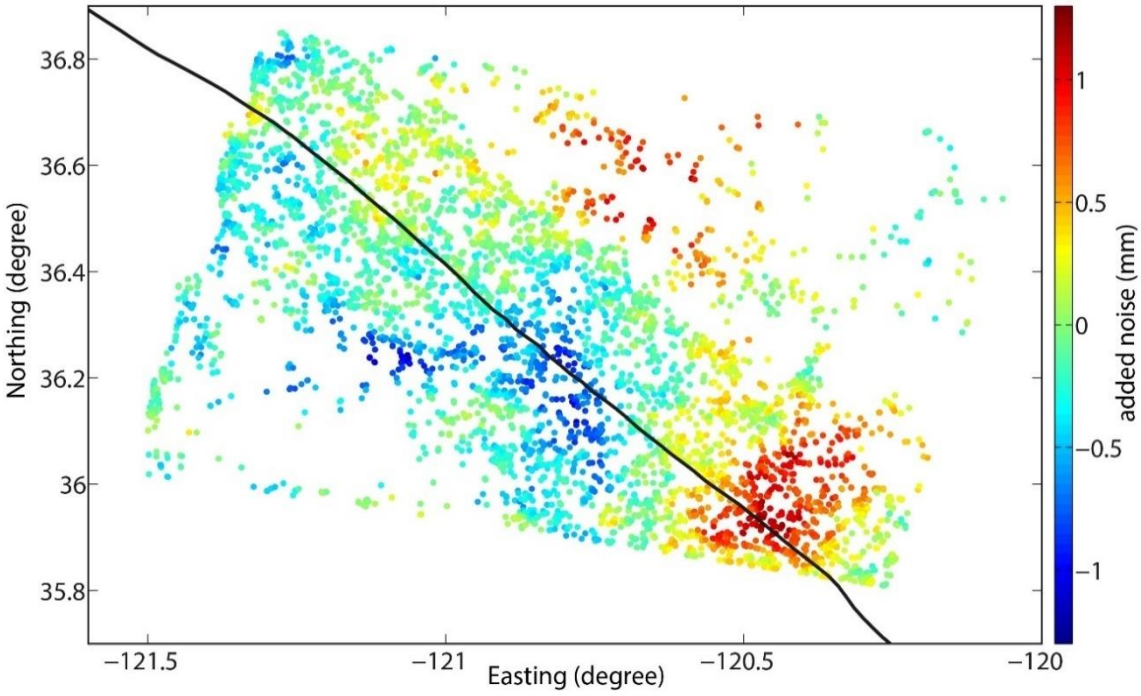

Figure B.1. Example of colored noise on InSAR surface observations, obtained from a random noise of 5 mm standard deviation. The black line shows the trace of San Andreas Fault.

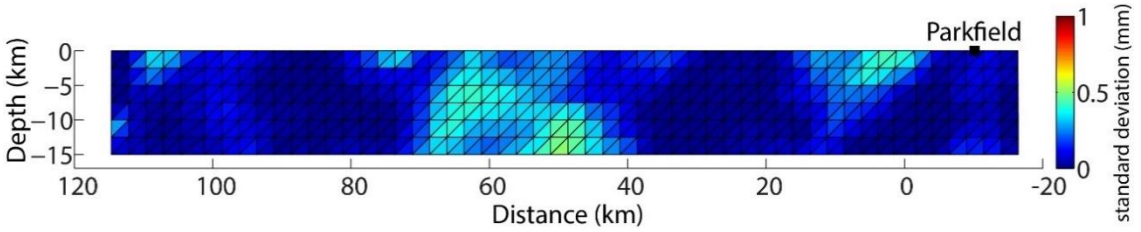

Figure B.2. Standard deviation of the obtained creep for 23 Jun 2004.

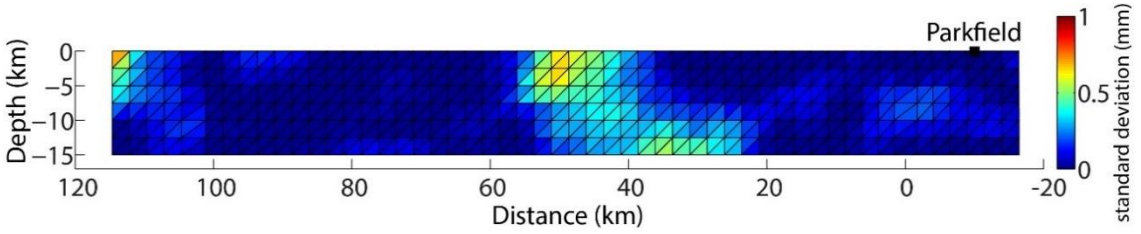

Figure B.3. Standard deviation of the obtained creep for 15 Dec 2004.

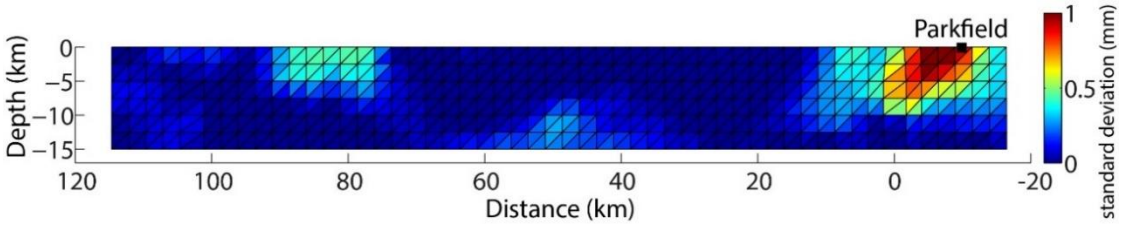

Figure B.4. Standard deviation of the obtained creep for 8 Jun 2005.

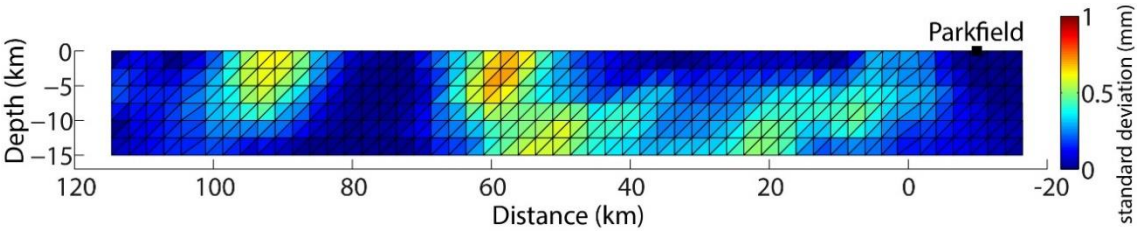

Figure B.5. Standard deviation of the obtained creep for 15 Mar 2006.

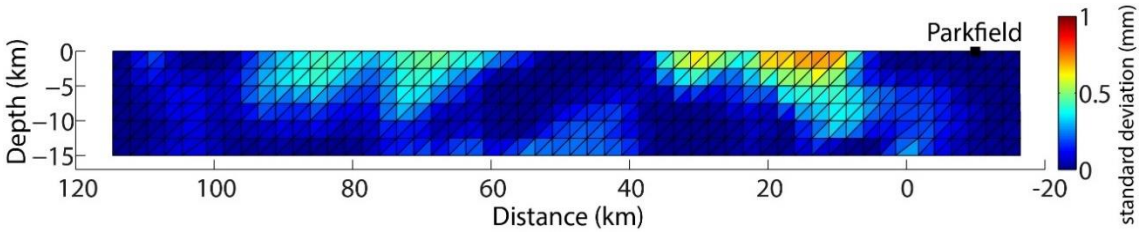

Figure B.6. Standard deviation of the obtained creep for 6 Sep 2006.

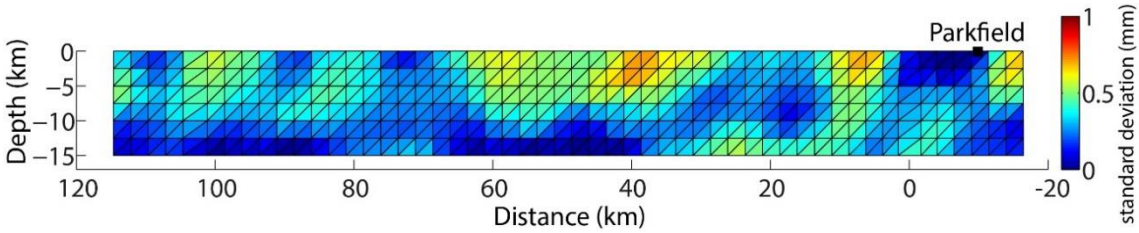

Figure B.7. Standard deviation of the obtained creep for 13 Feb 2008.

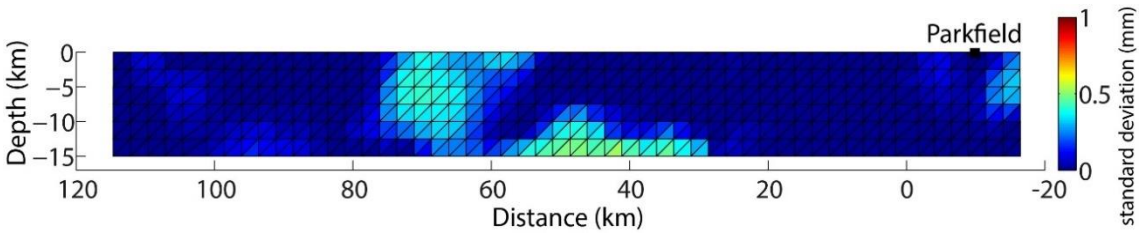

Figure B.8. Standard deviation of the obtained creep for 6 Aug 2008.

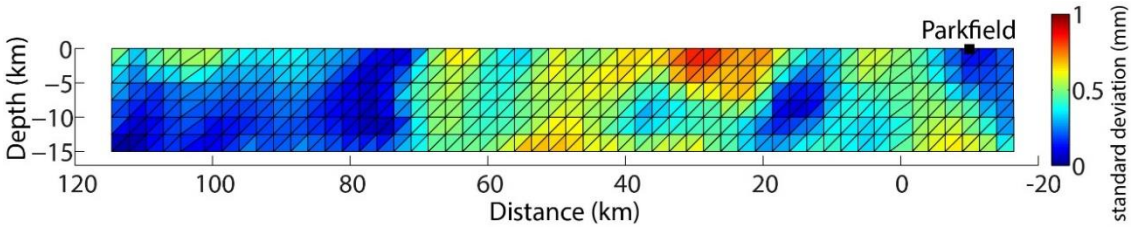

Figure B.9. Standard deviation of the obtained creep for 13 May 2009.

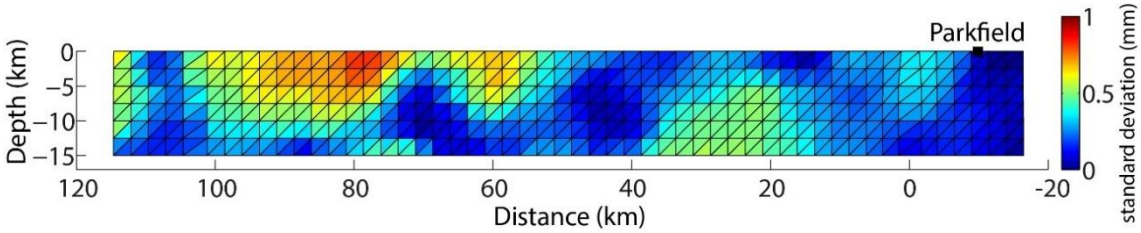

Figure B.10. Standard deviation of the obtained creep for 7 Jul 2010.

APPENDIX C.

CREEP ACCELERATION FROM CRE SEQUENCES

To obtain a reliable estimate of creep acceleration from CRE observations, the sequences with at least 4 events in the time interval of interest that conforms with some statistical criteria are used. We exclude the sequences that are short-lived, thus are related to the short-term transients (Satriano et al., 2014). The short-lived sequences are found by implementing the criteria $n\bar{T} < 0.7 \times (t_{end} - t_0)$, where n is the number of events between last (t_{end}: 7 Jul 2010) and first (t_0: 3 May1992) time steps, and $\bar{T}$ is the average recurrence interval. The "persistent" sequences (i.e., not short-lived) with at least 4 events, are then tested for detecting the sequence with statistically significant monotonic creep trend, using non-parametric Mann-Kendall (MK) test at 95% confidence level (Gilbert, 1987). The MK statistic for each CRE sequence is estimated as:

$$S_{MK} = \sum_{i=1}^{m-1} \sum_{j=i+1}^{m} \mathrm{sgn}(T_j - T_i)$$

where T_i is the time series of repeat time, $m = n - 1$ is the size of this time series, n is the size of CRE sequence as defined above, and sgn is the signum function. The variance of S_{MK} is estimated using:

$$\mathrm{Var}(S_{MK}) = \frac{1}{18}[m(m-1)(2m+5)]$$

Then S_{MK} and $\mathrm{Var}(S_{MK})$ are used to estimate the test statistic Z as follows:

$$Z = \begin{cases} (S_{MK} - 1)/\mathrm{Var}(S_{MK}) & \text{if } S_{MK} > 0 \\ 0 & \text{if } S_{MK} = 0 \\ (S_{MK} + 1)/\mathrm{Var}(S_{MK}) & \text{if } S_{MK} < 0 \end{cases}$$

Next, the MK test *p*-value is estimated as:

$$p = 1 - N_{cdf}(|Z|)$$

where N_{cdf} is the Gaussian cumulative distribution function which operates on $|Z|$. Lastly, the sequences with *p*-value below 0.05, which is considered as the significance level for

MK test (95% confidence level) are chosen. After fitting the equation (3.1) in the main text to CRE sequences that passed the MK test, a Chi-squared goodness-of-fit test at 95% confidence level is used to further narrow down the population of reliable CRE sequences.

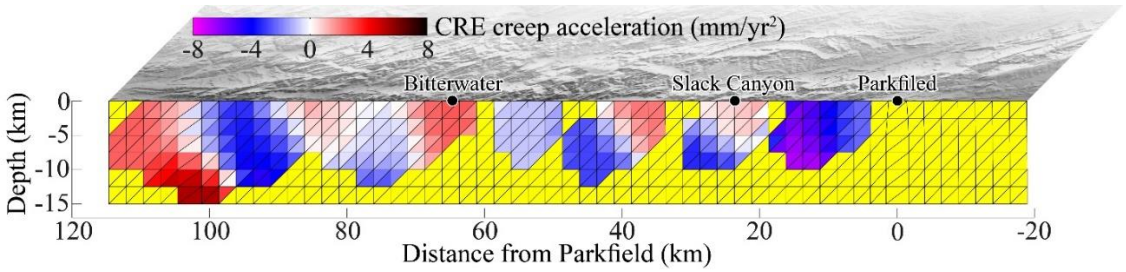

Figure C.1. The CRE creep acceleration oversampled on the triangular mesh. The patches that are located farther than 5km from a CRE sequence are shown with yellow color and are not assigned any values.

APPENDIX D.

PDF OF SHORT-TERM CREEP RATES AND POTENCY, CONSIDERING THE ESTIMATED UNCERTAINTY

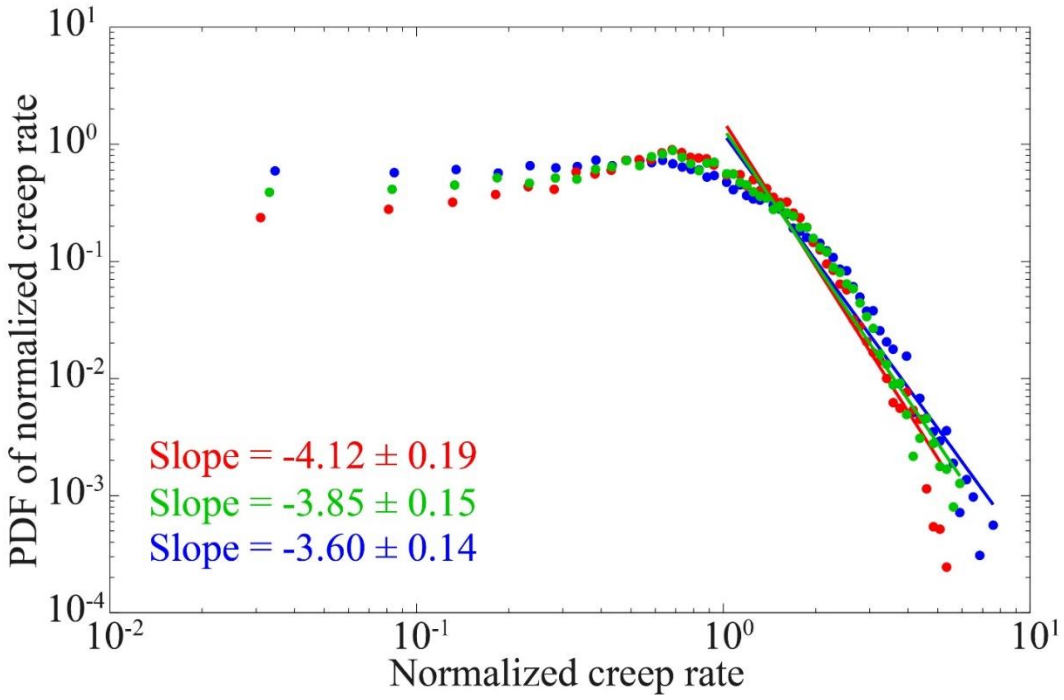

Figure D.1. The PDF of short-term creep rate, normalized by the mean rate, in log-log space. Green dots and line show the PDF of estimated short-term rate and associated power-law fit to the rates higher than the long-term rate, respectively. Red and blue colors show the associated PDF for short-term rates plus and minus one-sigma uncertainty, respectively.

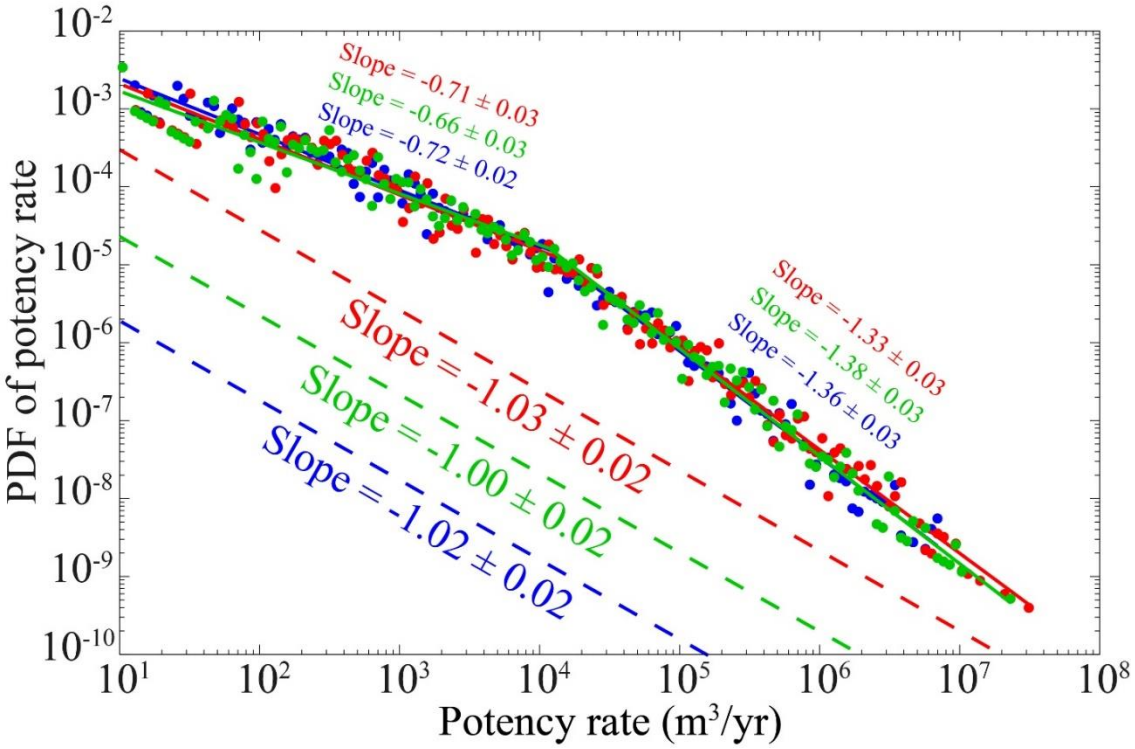

Figure D.2. The PDF of the potency rate. The dashed and solid lines respectively show the single and double power-law functions fitted to the PDF. Green, Red, and blue colors show the results for potency estimates using short-term rate, and short-term rate plus and minus one-sigma uncertainty, respectively.

APPENDIX E.

SUPPLEMENTARY FIGURES FOR CHAPTER 4

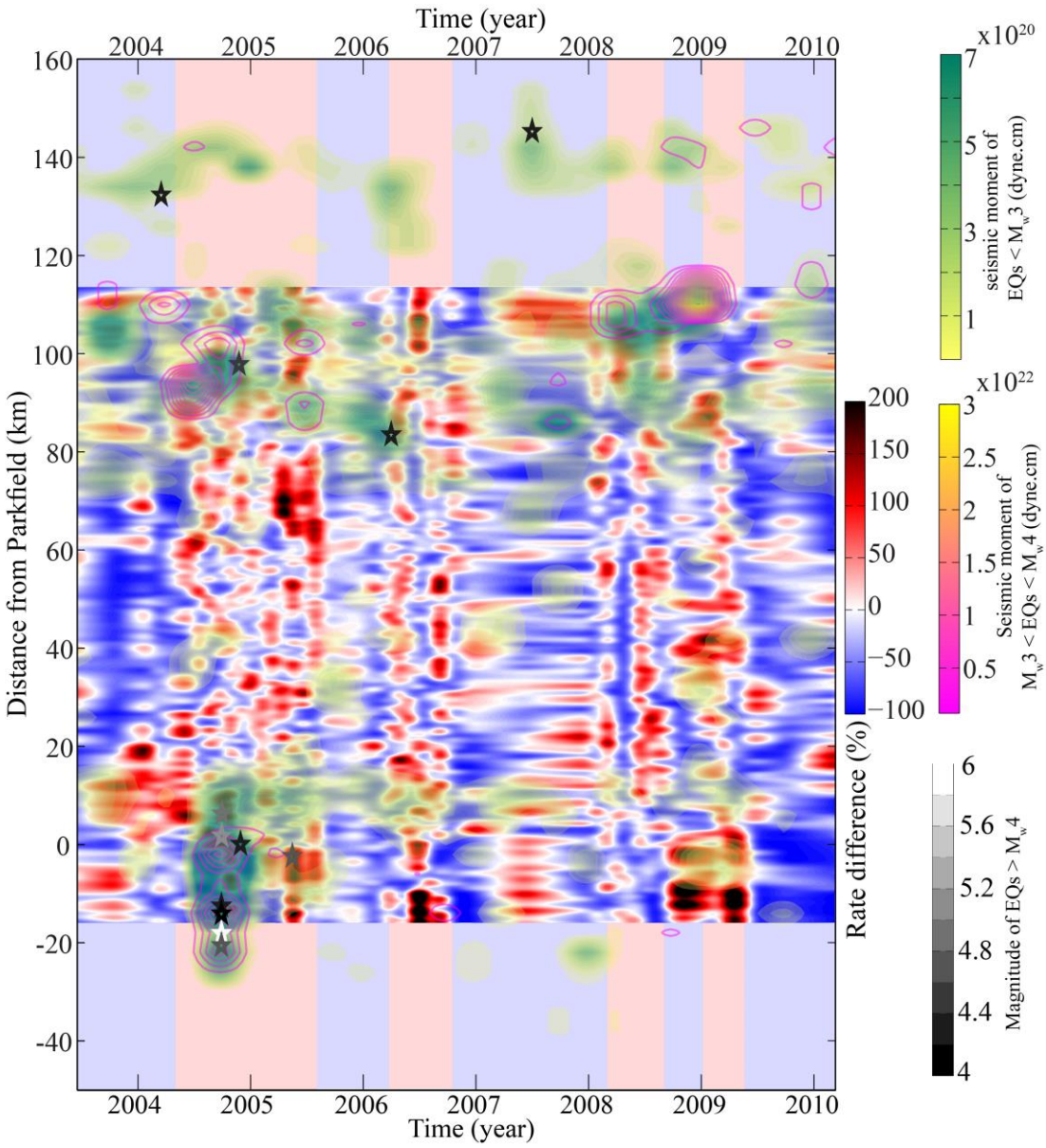

Figure E.1. The same as Figure 4.3, but with detailed moment release map. Seismic moment released is shown using the contours in yellow to green colormap for EQs < M_w3, and in magenta to yellow colormap for M_w3 < EQs < M_w4. A moving window with spatial size of 6 km (step size of 4 km), and temporal size of 3 month is used to estimate the seismic moment for the earthquakes within 2 km of either side of the fault. Lastly, a Gaussian smoothing filter of size 6 months is applied in the temporal dimension.

APPENDIX F.

SUPPLEMENTARY FIGURES FOR B-VALUE ESTIMATIONS DISCUSSED IN CHAPTER 5

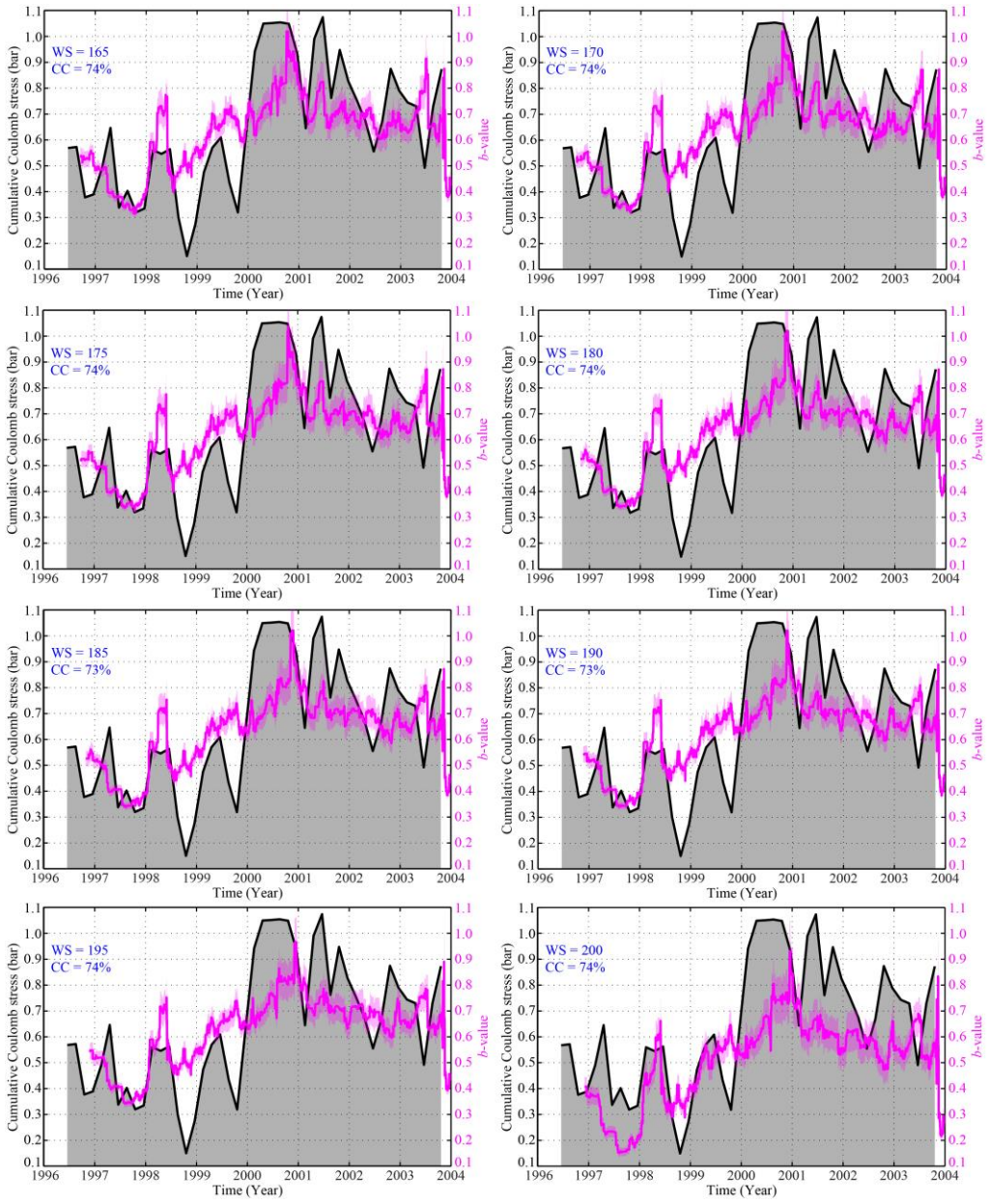

Figure F.1. Sensitivity of the *b*-value time series on size of moving window. The panels show *b*-value time series with M_c = 2.0 and window sizes from 156 to 200 with increments of 5 events. The black curve shows the time series of Coulomb stress on the shallow locked segment.

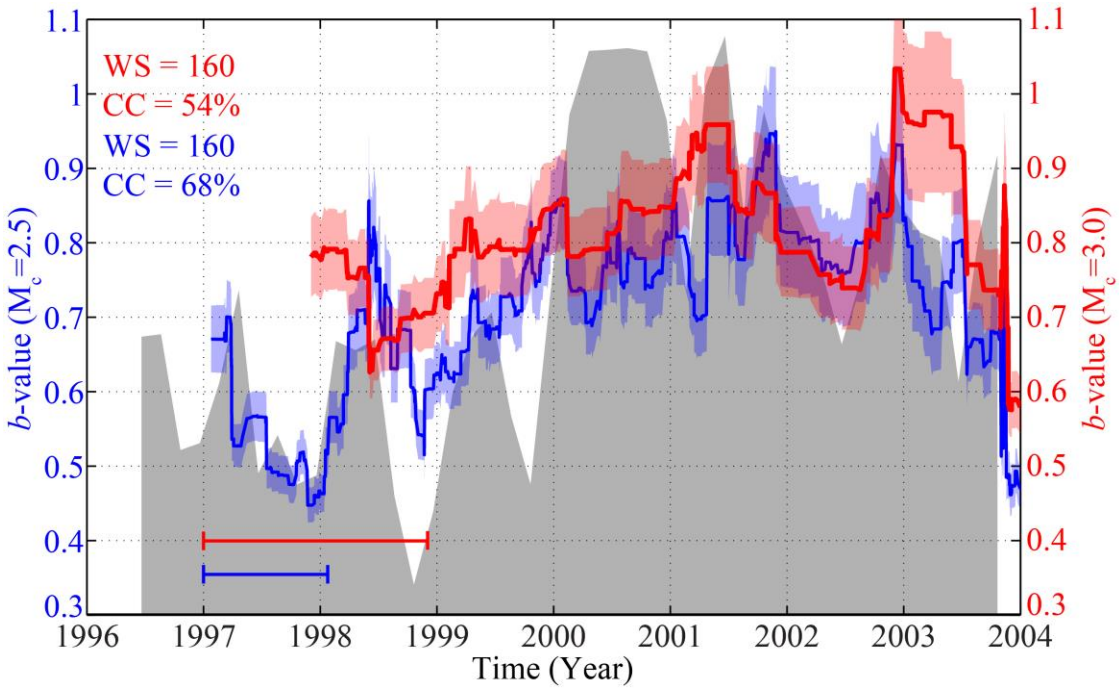

Figure F.2. Sensitivity of the b-value time series on magnitude of completeness. The blue and red curves show *b*-value time series considering M_c = 2.5 and M_c = 3.0 window size of 160, respectively. The black curve shows the time series of Coulomb stress on the shallow locked segment. The blue and red horizontal lines show the respective time span of moving window associated with the choice of completeness magnitude.

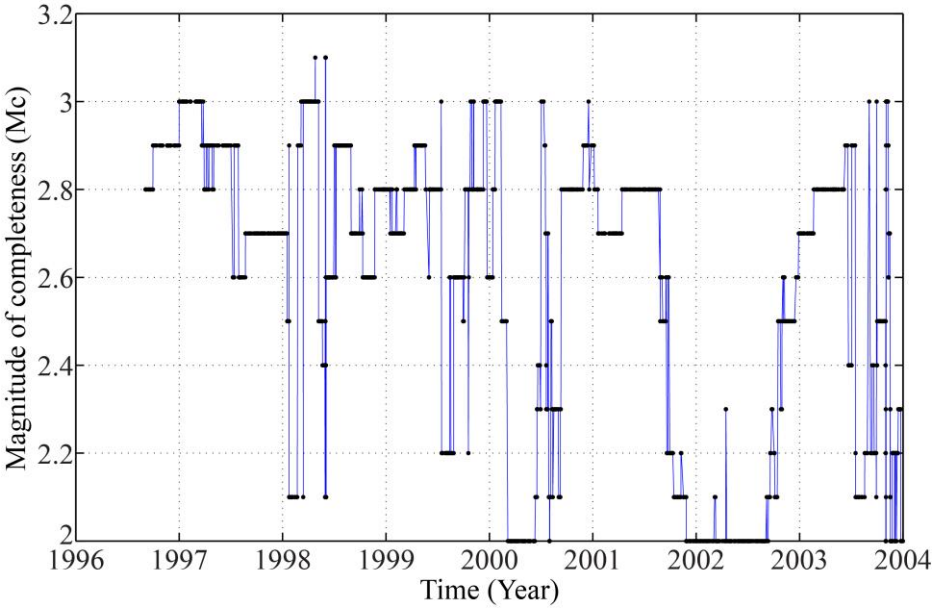

Figure F.3. Magnitude of completeness for each window estimated using Mc by b-value stability method